

Technische Universität München  
TUM School of Engineering and Design

# Conceptual Design and Modeling of a Module for Self-Sufficient Energy Supply with Hydrogen as Energy Carrier

Tin Jurišić

Vollständiger Abdruck der von der TUM School of Engineering and Design der Technischen Universität München zur Erlangung des akademischen Grades eines  
Doktors der Ingenieurwissenschaften  
genehmigten Dissertation.

Vorsitz: Prof. Dr.-Ing. Andreas Jossen

Prüfende der Dissertation: 1. Prof. Dr.-Ing. Harald Klein

2. Prof. Dr. rer. nat. Thomas Hamacher

Die Dissertation wurde am 17.01.2024 bei der Technischen Universität München eingereicht  
und durch die TUM School of Engineering and Design am 21.10.2024 angenommen.



Parts of the submitted dissertation have been published in the following:

JURISIC ET AL. 2021

JURISIC, T. ; REHFELDT, S. ; KNELLER, M. ; KLEIN, H.: *Range of application for a self-sufficient energy system with hydrogen as energy carrier in remote areas*. Proceedings of Global Power and Propulsion Society. 2021.



# Foreword

In 2005, my hydrogen journey started. I was in school at that time and hadn't given much thought to this very powerful element, which is connected to so many ideas and topics. At a street fair in Munich, I was able to examine a hydrogen car while my father sat next to me concluding "this is the future". The future didn't come as fast as he predicted, but the constant progress in hydrogen technologies under the radar of public perception made benefits of hydrogen suddenly more visible and led to projects such as the start of the world's first car sharing with fuel cell electric vehicles. Being part of this hydrogen pioneering work offered me insights into hydrogen technology and applications, which I was not aware they existed before. I realized that I want to learn more about hydrogen and be part of an evolving sustainable hydrogen economy, in which this thesis can be seen as a small contribution.

Along my hydrogen journey I met many hydrogen enthusiasts, who supported and enabled me in my undertakings. To all of you I would like to say: Thank you.

In particular, I want to thank my doctoral supervisor, Prof. Dr.-Ing. Harald Klein as well as Dr.-Ing. Sebastian Rehfeldt for the excellent mentoring and support during my thesis. The discussions we had always gave me the right impulses how to improve my work and thesis.

For the second examination of the thesis, I would like to thank Prof. Dr. rer. nat. Thomas Hamacher as well as Prof. Dr.-Ing. Andreas Jossen for acting as chair.

Moreover, I would like to thank Dipl.-Ing. Dr. h.c. Adolf Feizlmayr and Dr. Michel Kneller for the great support, discussions and setting the right conditions for me to master this thesis.

Also, I would like to emphasize my gratitude to the staff of ILF Consulting Engineers and the Chair of Plant and Process Technology of TUM, who helped me in critical stages of my thesis and proved that to every problem there is a solution.

Furthermore, I want to thank Madani Drave for the fruitful exchanges on containerized energy systems and site specific insights on energy demand in remote regions. It is important to find minds, who aim for the same goals with different ideas.

Finally, I want to express my grand gratitude to my family and thanks for all the support in the last years. Vielen Dank und hvala puno.

Abu Dhabi, January 2025

Tin Jurišić



# Abstract

In this work a new concept design for an off-grid hydrogen energy system is developed intended for rural electrification. Starting point for the development of this containerized system named selfHY<sup>®</sup> is the in-depth analysis of current hydrogen technology relevant for this plant design and extensive literature review. Utilizing this knowledge base, relevant options for renewable energy sources, hydrogen generation, storage and reconversion as well as the battery and electrical components are presented. The optimal configuration is defined by using the Munich Procedural Model and the weighted sum method. This resulted in the use of photovoltaic power as renewable energy source, PEM technology for hydrogen generation and reconversion as well as compressed hydrogen storage without an additional compression.

Furthermore, a simulation model to size the components of selfHY<sup>®</sup> has been developed with two major dependencies on the electrical load and the trend of renewable energy availability at the given location. Data from a 7-person household in Bamako, Mali from the year 2021 has been used to calculate the power and sizes of the selfHY<sup>®</sup> components leading to the result that the hydrogen storage is limiting further scale-up within one 20 foot container according to ISO 668. One 20 foot container equipped with hydrogen generation, storage and reconversion as well as a battery and all auxiliaries can cover the energy demand of two respective households. It is to mention that an additional 20 foot container is necessary for the renewable energy generation, where the PV panels are arranged on a mechanical structure for folding and unfolding on site.

Moreover, the process and electrical design is elaborated further in order to list all necessary equipment and components for the economic assessment of selfHY<sup>®</sup>. With regards to economics, four variants are defined varying in component size and ranging from 4 to 40 kW of installed hydrogen generation. It is to conclude that the smaller variants, which only use one single 20 foot container, do not reach comparable leveled cost of energy (LCOE) to other off-grid solutions. However, if selfHY<sup>®</sup> is extended by additional hydrogen storage containers, LCOE from 0.34 to 0.41  $\frac{\text{€}}{\text{kWh}}$  can be achieved.





# Contents

<b>Foreword</b>	<b>V</b>
<b>Abstract</b>	<b>VII</b>
<b>Formula Symbols and Abbreviations</b>	<b>XI</b>
<b>1 Introduction</b>	<b>1</b>
<b>2 Objectives and Initial Situation</b>	<b>3</b>
<b>3 State of the Art</b>	<b>5</b>
3.1 Renewable Energy . . . . .	5
3.1.1 Photovoltaic . . . . .	5
3.1.2 Concentrating Solar Power . . . . .	10
3.1.3 Wind . . . . .	12
3.1.4 Hydropower . . . . .	17
3.2 Hydrogen Generation . . . . .	20
3.2.1 Water Treatment . . . . .	22
3.2.2 Electrolysis . . . . .	27
3.2.2.1 Alkaline Electrolysis . . . . .	28
3.2.2.2 Proton Exchange Membrane Electrolysis . . . . .	29
3.2.2.3 Solid Oxide Electrolysis . . . . .	31
3.2.2.4 Anion Exchange Membrane Electrolysis . . . . .	32
3.2.3 Hydrogen Purification . . . . .	33
3.3 Hydrogen Storage . . . . .	34
3.4 Hydrogen Reconversion . . . . .	39
3.5 Battery Storage and Electrical Components . . . . .	43
3.6 Self-Sufficient Energy Systems with Hydrogen . . . . .	49
<b>4 Specification of selfHY<sup>®</sup></b>	<b>53</b>
4.1 Requirement Analysis . . . . .	54
4.1.1 System . . . . .	54
4.1.2 Renewable Energy . . . . .	55
4.1.3 Hydrogen Generation . . . . .	56
4.1.4 Hydrogen Storage . . . . .	58
4.1.5 Hydrogen Reconversion . . . . .	60
4.1.6 Auxiliary Equipment . . . . .	61
4.2 Configuration of selfHY <sup>®</sup> . . . . .	61
<b>5 Modeling of selfHY<sup>®</sup></b>	<b>65</b>
5.1 Operating Philosophy . . . . .	65
5.2 Hydrogen Generation . . . . .	68

---

5.3	Hydrogen Reconversion . . . . .	82
5.4	Hydrogen Storage . . . . .	85
5.5	Battery . . . . .	87
5.6	Photovoltaic Power Plant . . . . .	89
<b>6</b>	<b>Simulation and Results</b>	<b>93</b>
<b>7</b>	<b>Basic Design</b>	<b>105</b>
7.1	Process . . . . .	105
7.2	Electrical . . . . .	110
7.3	3D-Model and Variants . . . . .	112
<b>8</b>	<b>Economic Evaluation</b>	<b>117</b>
8.1	Cost Estimation for selfHY <sup>®</sup> Variants . . . . .	117
8.2	Comparison with other Renewable Microgrids . . . . .	123
<b>9</b>	<b>Outlook</b>	<b>125</b>
<b>A</b>	<b>Operating Modes and Active Streams</b>	<b>127</b>
<b>B</b>	<b>Parameter Values for Simulation</b>	<b>129</b>
<b>C</b>	<b>Process Flow Diagram</b>	<b>131</b>
<b>D</b>	<b>Single Line Diagram</b>	<b>133</b>
	<b>Bibliography</b>	<b>135</b>

# Formula Symbols and Abbreviations

## Latin Formula Symbols

$a$	Axial induction factor	
$a_{ij}$	Performance value	
$A_D$	Area of actuator disc	$m^2$
$A_{Ely,act}$	Active area of electrolysis	$m^2$
$A_{Ely,Cell}$	Active area of electrolysis cell	$m^2$
$A_{Ely,Stack}$	Active area of electrolysis stack	$m^2$
$A_{FC,act}$	Active area of fuel cell	$m^2$
$A_{FC,Cell}$	Active area in cell of fuel cell	$m^2$
$A_{FC,Stack}$	Active area of fuel cell stack	$m^2$
$A_{Panel}$	Surface area of PV panel	$m^2$
$A_{PV}$	Area of PVPP	$m^2$
$A_{WSM}$	Weighted sum method score	
$c_{drag}$	Drag coefficient	
$c_{HP}$	Power consumption factor of hydrogen purification	$\frac{kWh}{m^3}$
$c_{PV}$	Capacity factor	
$c_{th}$	Theoretical specific battery capacity	$\frac{Ah}{g}$
$C$	Concentration ratio	
$C_0$	Capital expenditure	€
$C_P$	Power coefficient	
$c_{W,demi}$	Conversion factor for demineralized water demand	
$d$	Discount factor	
$e$	Specific battery energy	$\frac{Wh}{g}$
$e_{WT}$	Specific energy consumption of water treatment	$\frac{kWh}{m^3}$
$E_a$	Annual energy production	kWh
$E_{Anode}$	Reduction potential of anode	V
$E_{Bat}$	Energy storage capacity of battery	kWh
$E_{Bat,id}$	Ideal energy storage capacity of battery	kWh
$E_C$	Compression energy	kWh
$E_{Cathode}$	Reduction potential of cathode	V
$E_{Cell}$	Cell voltage according to Nernst	V
$E_{Cell,th}$	Cell voltage under standard conditions	V
$E_{el}$	Electrical energy	kWh

$E_{SOC,id}$	Ideal state of charge	kWh
$f_{Bat}$	Battery discharge scaling factor	
$f_{Ely,cool}$	Electrical efficiency factor of electrolysis cooling unit	
$f_{FC,cool}$	Electrical efficiency factor of fuel cell cooling unit	
$f_{Feed}$	Feed water flow	$\frac{m^3}{h}$
$f_P$	Permeate flow	$\frac{m^3}{h}$
$F$	Faraday constant	$\frac{As}{mol}$
$g$	Gravitational constant	$\frac{m}{s^2}$
$\Delta G$	Gibbs free energy change	$\frac{J}{kg}$
$h$	Elevation head	m
$\Delta h_C$	Enthalpy change of compression	$\frac{kJ}{kg}$
$\Delta h_{Ely,cool}$	Enthalpy change of electrolysis cooling	$\frac{kJ}{kg}$
$\Delta h_{FC,cool}$	Enthalpy change of fuel cell cooling	$\frac{kJ}{kg}$
$H$	Height	m
$\Delta H_{hydr}$	Hydrogenation enthalpy of LOHC compound pair	$\frac{kJ}{mol}$
$H_L$	Head loss in piping system	m
$H_{Sep}$	Height of oxygen separator	m
$\Delta_R \bar{H}$	Reaction enthalpy	$\frac{kJ}{mol}$
$i_{Ely}$	Current density electrolysis	$\frac{A}{m^2}$
$I_{Ely}$	Electrolysis current	A
$i_{FC}$	Current density of fuel cell	$\frac{A}{m^2}$
$I_{FC}$	Fuel cell current	A
$I_{Ph}$	Photocurrent	A
$j_{Ely,Cell}$	Power density of electrolysis cell	$\frac{kW}{m^2}$
$J_T$	Flux at operating temperature	$\frac{kg}{m^2 s}$
$k$	Boltzmann constant	$\frac{eV}{K}$
$K$	Membrane permeability constant	$\frac{mol}{m s Pa}$
$l$	Membrane thickness	$\mu m$
$L_{Ely}$	Load of electrolysis operation	
$L_{FC}$	Load of fuel cell operation	
$LHV_{H_2}$	Lower heating value of hydrogen	$\frac{kWh}{kg}$
$L_N$	Diffusion length	$\mu m$
$\dot{m}_{Ely,cool}$	Mass flow for electrolyzer cooling	$\frac{kg}{h}$
$\dot{m}_{FC,cool}$	Mass flow for fuel cell cooling	$\frac{kg}{h}$
$M$	Molecular mass	$\frac{g}{mol}$
$M_{H_2}$	Molar mass of hydrogen	$\frac{g}{mol}$

$M_{\text{H}_2\text{O}}$	Molar mass of water	$\frac{\text{g}}{\text{mol}}$
$M_{\text{H}_2}$	Molar mass of hydrogen	$\frac{\text{g}}{\text{mol}}$
$n$	Product life	years
$n_i$	Intrinsic carrier density	$\frac{1}{\text{m}^3}$
$N_0$	Density of states	$\frac{1}{\text{cm}^3}$
$N_{\text{Ely,Stack}}$	Number of electrolysis stack	
$N_{\text{Ely,Stack,Cell}}$	Number of electrolysis cells per stack	
$N_{\text{FC,Stack}}$	Number of fuel cell stacks	
$N_{\text{FC,Stack,Cell}}$	Number of cells per fuel cell stack	
$N_{\text{H}_2,g}$	Dragged gaseous amount of substance of hydrogen	mol
$N_{\text{H}_2\text{O},g}$	Dragged gaseous amount of substance of water	mol
$N_{\text{H}_2\text{O},l}$	Dragged liquid amount of substance of water	mol
$N_{\text{O}_2,g}$	Dragged gaseous amount of substance of oxygen	mol
$N_{\text{out},g}$	Total gaseous amount of substance	mol
$\Delta N_{\text{H}_2}$	Difference in amount of substance of hydrogen	mol
$\Delta N_{\text{H}_2\text{O}}$	Difference in amount of substance of water	mol
$O_0$	Yearly operational expenditure	€
$\Delta p$	Transmembrane pressure	Pa
$p_D^+$	Pressure upstream at actuator disk	bar
$p_D^-$	Pressure downstream at actuator disk	bar
$p_{\text{Ely}}$	Electrolysis operating pressure	bar
$p_{\text{Ely,An}}$	Pressure at anode of electrolysis	bar
$p_{\text{FC}}$	Operating pressure of fuel cell	bar
$p_{\text{H}_2\text{O}}$	Partial pressure of water	bar
$p_{\text{H}_2,\text{Store}}$	Pressure of hydrogen storage	bar
$p_{\text{O}_2}^a$	Partial pressure of oxygen	bar
$p_{\text{Store}}$	Storage pressure	bar
$P_{\text{Bat,AC}}$	Battery power (alternating current)	kW
$P_{\text{Bat,Charge}}$	Battery charging power	kW
$P_{\text{Bat,DC}}$	Battery power (direct current)	kW
$P_{\text{Bat,Dis}}$	Battery discharging power	kW
$P_C$	Compression power	kW
$P_E$	Electrical power output	kW
$P_{\text{Ely,AC}}$	Electrolysis power (alternating current)	kW
$P_{\text{Ely,cool}}$	Cooling power for electrolysis	kW
$P_{\text{Ely,DC}}$	Electrolysis power (direct current)	kW

$P_{Ely,DC,max}$	Maximum power for electrolysis operation	kW
$P_{Ely,DC,min}$	Minimum power for electrolysis operation	kW
$P_{FC,AC}$	Fuel cell power (alternating current)	kW
$P_{FC,AC,max}$	Maximum fuel cell power (alternating current)	kW
$P_{FC,cool}$	Cooling power for fuel cell	kW
$P_{FC,DC}$	Fuel cell power (direct current)	kW
$P_{FC,DC,max}$	Maximum power of fuel cell	kW
$P_H$	Hydropower considering losses	kW
$P_{HL}$	Hydraulic friction losses	kW
$P_{HP}$	Power for hydrogen purification	kW
$P_{H,th}$	Theoretical hydropower	kW
$P_{Load}$	Electrical load	kW
$P_{Load,max}$	Maximum electrical load	kW
$P_{Panel}$	Power of PV panel	kW
$P_{PV}$	PVPP installed peak power	kW
$P_{PV,AC}$	Power of PV plant (alternating current)	kW
$P_{PV,DC}$	Power of PV plant (direct current)	kW
$P_W$	Wind power	kW
$P_{WT}$	Water treatment unit power	kW
$\Delta P$	Difference of power generation and load	kW
$Q$	Reaction quotient	
$\dot{Q}$	Heat flow rate	kW
$\dot{Q}_{Ely}$	Heat of electrolysis	kW
$\dot{Q}_{FC}$	Heat of fuel cell	kW
$r_{HD}$	Ratio of height to diameter of oxygen separator	
$R$	Universal gas constant	$\frac{J}{K \text{ mol}}$
$R_{LHV}$	Ratio of compression energy to LHV of hydrogen	
$RR$	Recovery rate	
$R_{Sep}$	Radius of oxygen separator	m
$R_T$	Total resistance in membrane system	$\frac{m^2}{kg}$
$s$	Supersaturation factor	
$s_{Bat}$	Scaling factor for battery storage	
$S_{O_2}$	Oxygen solubility in water	$\frac{mol}{Pa \cdot m^3}$
$s_{PV}$	Area safety factor of PVPP	
$\Delta s$	Entropy difference	$\frac{J}{K}$
$\Delta t$	Time step	h

---

$T$	Temperature	$^{\circ}\text{C}$
$T_{boil}$	Boiling point of LOHC compound pair	$^{\circ}\text{C}$
$T_{Ely}$	Temperature of electrolysis	$^{\circ}\text{C}$
$T_{\text{H}_2,Store}$	Temperature of hydrogen storage	$^{\circ}\text{C}$
$T_{melt}$	Melting point of LOHC compound pair	$^{\circ}\text{C}$
$T_W$	Force on the air, torque	N
$u_{G,max}$	Maximum allowable flow velocity	$\frac{\text{m}}{\text{s}}$
$u_{G,\text{O}_2}$	Flow velocity of oxygen	$\frac{\text{m}}{\text{s}}$
$U_{Bat}$	Battery voltage	V
$U_D$	Diffusion voltage	V
$U_{Ely,Cell}$	Operating voltage electrolysis cell	V
$U_{Ely,max}$	Maximum operating voltage electrolysis cell	V
$U_{Ely,min}$	Minimum operating voltage electrolysis cell	V
$U_{Ely,Stack}$	Electrolysis stack voltage	V
$U_{FC,Cell}$	Cell voltage of fuel cell	V
$U_{FC,max}$	Maximum cell voltage of fuel cell	V
$U_{FC,min}$	Minimum cell voltage of fuel cell	V
$U_{th}$	Thermoneutral voltage	V
$V_D$	Wind speed at actuator disc	$\frac{\text{m}}{\text{s}}$
$\dot{V}_{\text{H}_2,Ely}$	Hydrogen volume flow to hydrogen purification unit	$\frac{\text{m}^3}{\text{h}}$
$\dot{V}_{\text{H}_2,FC,cool}$	Hydrogen volume flow for cooling system operation	$\frac{\text{m}^3}{\text{h}}$
$\dot{V}_{\text{H}_2,Rec}$	Hydrogen volume flow to fuel cell	$\frac{\text{m}^3}{\text{h}}$
$\dot{V}_{\text{H}_2,Store}$	Hydrogen volume flow to hydrogen storage	$\frac{\text{m}^3}{\text{h}}$
$\dot{V}_{\text{O}_2}$	Volume flow of oxygen	$\frac{\text{m}^3}{\text{h}}$
$\dot{V}_{\text{O}_2,Ely,out}$	Volume flow of oxygen from electrolysis stack	$\frac{\text{m}^3}{\text{h}}$
$\dot{V}_{\text{O}_2,out}$	Volume flow of oxygen to vent	$\frac{\text{m}^3}{\text{h}}$
$V_{Sep}$	Inner separator volume	$\text{m}^3$
$V(t_0)_{Tank}$	Volume of stored hydrogen at simulation start	$\text{m}^3$
$\dot{V}_{Tank}$	Volume flow in or out of storage tank	$\frac{\text{m}^3}{\text{h}}$
$V_{Tank}$	Volume of stored hydrogen	$\text{m}^3$
$V_{Tank,0}$	Volume of hydrogen storage tank	$\text{m}^3$
$V_W$	Downstream wind velocity	$\frac{\text{m}}{\text{s}}$
$\dot{V}_W$	Volumetric flow rate	$\frac{\text{m}^3}{\text{h}}$
$\dot{V}_{W,demi}$	Volume flow of demineralized water	$\frac{\text{m}^3}{\text{h}}$
$\dot{V}_{W,Ely,in}$	Volume flow of water to electrolysis stack	$\frac{\text{m}^3}{\text{h}}$
$\dot{V}_{W,Ely,out}$	Volume flow of water from electrolysis stack	$\frac{\text{m}^3}{\text{h}}$

---

$\dot{V}_{W,in}$	Feed water volume flow	$\frac{\text{m}^3}{\text{h}}$
$V_{W,liq}$	Liquid water volume in oxygen separator	$\text{m}^3$
$\dot{V}_{W,out}$	Volume flow of waste water	$\frac{\text{m}^3}{\text{h}}$
$\dot{V}_{W,pot}$	Volume flow of potable water	$\frac{\text{m}^3}{\text{h}}$
$\dot{V}_{W,pot,p.P.}$	Volume flow of potable water per person	$\frac{\text{m}^3}{\text{h}}$
$V_\infty$	Initial wind velocity	$\frac{\text{m}}{\text{s}}$
$w_j$	Criterion importance	
$w$	Weight factor	
$\Delta W_G$	Bandgap energy	eV
$x$	Distance between Fresnel reflectors	m
$y_{\text{H}_2}$	Molar fraction of hydrogen in gaseous phase	
$y_{\text{H}_2\text{O}}$	Molar fraction of water in gaseous phase	
$y_{\text{O}_2}$	Molar fraction of oxygen in gaseous phase	
$z$	Number of electrons	



## Greek Formula Symbols

$\gamma_W$	Specific weight for water	$\frac{N}{m^3}$
$\eta_{AC/DC,El_y}$	Efficiency AC/DC converter electrolyzer	
$\eta_{AC/DC,FC}$	Efficiency AC/DC converter fuel cell	
$\eta_{Bat}$	Battery efficiency	
$\eta_{DCAC}$	Efficiency DC/AC converter	
$\eta_{EG}$	Electric generator efficiency	
$\eta_{el}$	Electric efficiency	
$\eta_{Ely}$	Electrolysis efficiency	
$\eta_{ET}$	Electric transformer efficiency	
$\eta_F$	Faraday efficiency	
$\eta_{FC}$	Fuel cell efficiency	
$\eta_{HPP}$	Hydropower plant efficiency	
$\eta_{HT}$	Hydroturbine efficiency	
$\eta_{is}$	Isentropic efficiency	
$\eta_{max}$	Maximum efficiency	
$\eta_{WT}$	Efficiency water treatment	
$\mu_T$	Viscosity at operating temperature	Pa s
$\rho_{Air}$	Air density	$\frac{kg}{m^3}$
$\rho_D$	Air density at actuator disk	$\frac{kg}{m^3}$
$\rho_{H_2O}$	Density of water	$\frac{kg}{m^3}$
$\rho_{H_2O,cool}$	Density of cooling water	$\frac{kg}{m^3}$
$\rho_{H_2O,st}$	Density of water at standard conditions	$\frac{kg}{m^3}$
$\rho_{H_2,st}$	Density of hydrogen at standard conditions	$\frac{kg}{m^3}$
$\rho_\infty$	Ambient air density	$\frac{kg}{m^3}$
$\tau$	Retention time	min

## Abbreviations

AACE	Association for the Advancement of Cost Engineering
AC	Alternating current
AE	Alkaline electrolysis
AEC	Alkaline electrolysis cell
AFC	Alkaline fuel cell
AEME	Anion exchange membrane electrolysis
AEMEC	Anion exchange membrane electrolysis cell
ASTM	American society for testing and materials

ATEX	EU directive on explosive atmospheres
BDC	Bottom dead center
BEV	Battery electric vehicles
BESS	Battery energy storage system
BM	Biomass
BMS	Battery management system
C	Carbon
CV	Control valve
CAPEX	Capital expenditure
CH <sub>2</sub>	Compressed hydrogen
CCS	Carbon capture and storage
CCUS	Carbon capture, utilization and storage
CSP	Concentrating solar power
DC	Direct current
DG	Diesel generator
DMFC	Direct methanol fuel cell
DOH	Degree of hybridization
EDI	Electrodeionization
ELY	Electrolyzer
EN	European Norm
ESD	Emergency shutdown
FC	Fuel cell
FCH 2 JU	Fuel Cell and Hydrogen Joint Undertaking
FT	Flow transmitter
GDP	Gross domestic product
GHG	Greenhouse gas
HER	Hydrogen evolution reaction
HAWT	Horizontal axis wind turbines
IBC	Intermediate bulk container
ICE	Internal combustion engine
IEC	International Electrotechnical Commission
IRENA	International Renewable Energy Agency
ISO	International Organization for Standardization
KOH	Potassium hydroxide
KPI	Key performance indicator
LAB	Lead-acid battery

---

LCAPEX	Levelized capital expenditure
LCOE	Levelized cost of energy
LFP	Lithium iron phosphate
LH <sub>2</sub>	Liquid hydrogen
LHV	Lower heating value
LMO	Lithium manganese oxide
LOHC	Liquid organic hydrogen carrier
LT	Level transmitter
LTO	Lithium titanate oxide
MEA	Membrane electrode assembly
MERRA	Modern-era retrospective analysis for research and applications
MCH	Methylcyclohexane
MCFC	Molten carbonate fuel cell
MPM	Munich procedural model
MPPT	Maximum power point tracker
NEC	N-Ethylcarbazole
NCA	Lithium nickel cobalt aluminum oxide
NMC	Lithium nickel manganese cobalt oxide
OER	Oxygen evolution reaction
OPEX	Operational expenditure
PAFC	Phosphoric acid fuel cell
PDT	Pressure difference transmitter
PEME	Proton exchange membrane electrolysis
PEMEC	Proton exchange membrane electrolysis cell
PEMFC	Proton exchange membrane fuel cell
PFD	Process flow diagram
PGM	Platinum group metal
PLC	Programmable logic controller
PSA	Pressure swing adsorption
PT	Pressure transmitter
PV	Photovoltaic
PVPP	Photovoltaic power plant
QT	Quality transmitter
RO	Reverse osmosis
SLD	Single line diagram
SOE	Solid oxide electrolysis

SOEC	Solid oxide electrolysis cell
SOFC	Solid oxide fuel cell
TESSC	Toshiba Energy Systems & Solutions Corporation
TDC	Top dead center
TDS	Total dissolved solids
TOC	Total organic carbon
TRBS	Technische Regeln für Betriebssicherheit (standard for operational safety)
TrinwV	German drinking water regulation
TRL	Technology readiness level
TRNSYS	Plant simulation tool
TSA	Temperature swing adsorption
TT	Temperature transmitter
VAWT	Vertical axis wind turbines
VDE	Association of German electrical engineers
VDI	Association of German engineers
VGOT	Variable-geometry oval-trajectory Darrieus wind turbine
WSM	Weighted sum method
WT	Wind turbine

# 1 Introduction

In the Paris Agreement of 2015, 194 countries committed their intention to “hold[...] the increase in the global average temperature to well below 2 °C above pre-industrial levels and [to] pursue [...] efforts to limit the temperature increase to 1.5 °C above pre-industrial levels[...]”. To reach this goal, many carbon emission sources need to be mitigated. In addition new technologies with no carbon emissions are key to a more sustainable future and can lead to a turnaround in the climate change trend. Either way, this global goal can only be achieved in a common approach by involving all countries and in particular by supporting developing countries as stated in the Paris Agreement under Article 4.4.

While focusing on the efforts of developing a cleaner future with more renewable energy and less carbon emissions, around one billion people still do not have access to electricity at all (see Figure 1.1). Combining the challenges connected to climate change with the challenges of providing energy access to everybody, puts certain regions in an unfavorable situation. As shown in Figure 1.1 Sub-Saharan Africa and South Asia

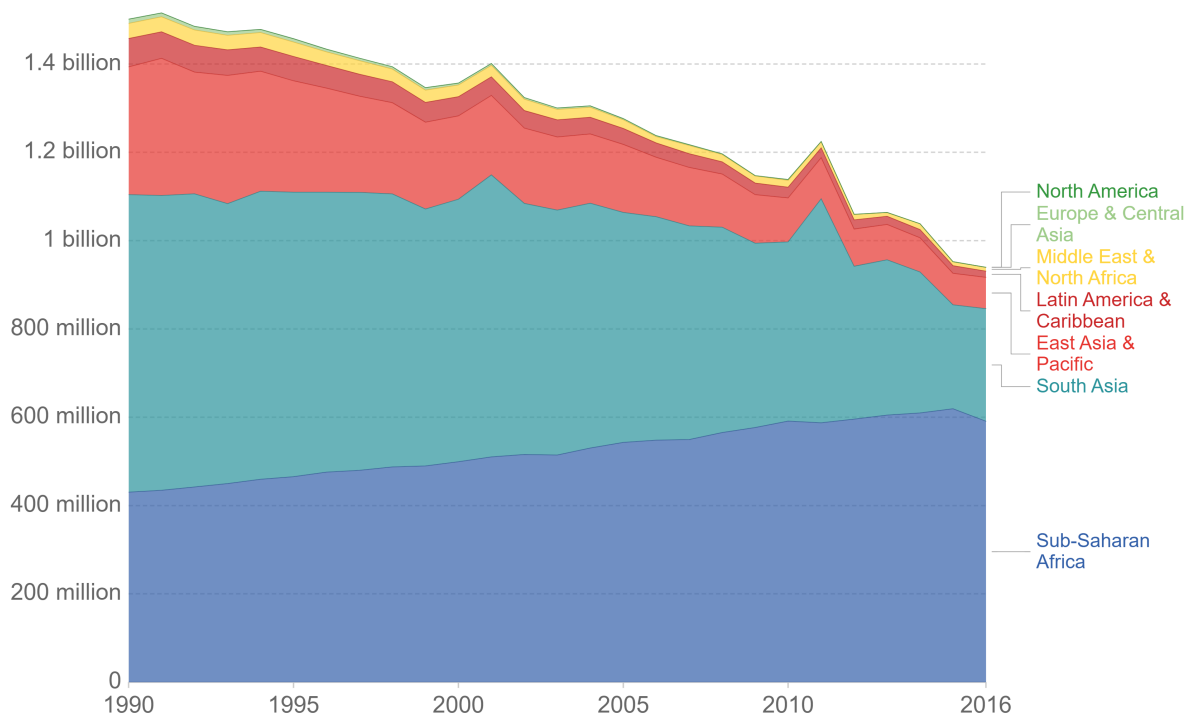


**Figure 1.1:** People without access to electricity from 1990 to 2016 [RITCHIE 2019]

account for around 900 million people without access to electricity, but at the same time favorable circumstances to use renewable energy for electrification purposes are present. The limiting factor with regards to electrification are the remote locations with no access to relevant energy infrastructure. The key question is: How can the abundant renewable energy in these remote locations be used to provide a stable electricity supply at all

times? A self-sufficient energy system based on renewable energy sources can be the solution, but many different configurations of such a system pose the follow-up questions of how to design such a self-sufficient energy system and what technologies are suitable for this application. In particular, due to the volatility of renewable energy sources, an appropriate energy storage solution needs to be provided in order to guarantee security of energy supply. This crucial aspect of the energy system can be solved by using hydrogen as an energy carrier.

As shown in GSTÖHL & PFENNINGER 2020 self-sufficient households will be possible and feasible even in regions with temperate climates, where solar radiation is lower and the area for installation of renewable energies is more limited compared to regions in Sub-Saharan Africa. The evaluated scenarios show that hydrogen as an energy carrier is crucial to guarantee security of supply and can be complementary to storage solutions with batteries or, in certain cases, may even be the optimal solution on its own.

In conclusion, to tackle both challenges of electrification and climate change in remote regions, concepts for self-sufficient energy systems need to be developed. This thesis focuses on the conception and modeling of selfHY<sup>®</sup>, a self-sufficient energy system with hydrogen as energy carrier.

## 2 Objectives and Initial Situation

The main objective of this work is to develop and model a feasible concept for a self-sufficient energy system based on renewable electricity and hydrogen. In order to get a better overview of the necessary components for selfHY<sup>®</sup>, relevant technologies are described and analyzed. Moreover, specific requirements to the energy system are formulated, forming the basis for evaluation of different configurations of the system. As a result, the optimal configuration with regards to the respective requirements is chosen and further analysis on the process design, sizing and costs of the system are conducted.

Based on the results from the detailed system modeling for a period of one year, the individual components of selfHY<sup>®</sup> are sized and arranged within a 20 foot container. For the economic assessment, the system is subdivided in its components and the respective costs are estimated resulting in the identification of main cost drivers. Moreover, a sensitivity analysis is performed to identify the current LCOE of selfHY<sup>®</sup>. At last and taking into account the generated results, an outlook is given discussing benefits and challenges of selfHY<sup>®</sup> and its possible impact on a sustainable future in remote regions.

Figure 2.1 reveals the basic process of selfHY<sup>®</sup> with inputs and outputs as well as the system boundary. Two main parts of the system can be identified: One is considered as the hydrogen part involving the subsystems hydrogen generation, storage and reconversion, the other one is the electrical part consisting of the subsystem renewable energy source.

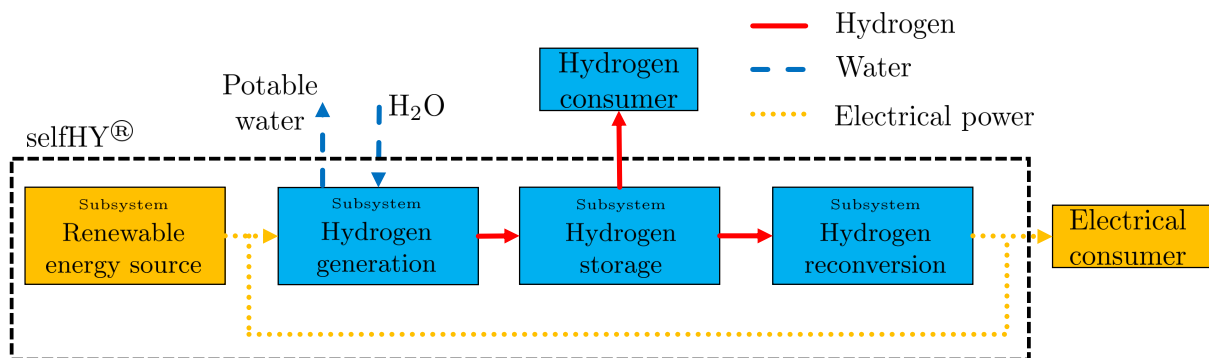


**Figure 2.1:** General process of selfHY<sup>®</sup>

The renewable energy source provides power to two main electrical consumers. As long as electricity is generated and the demand by an electrical consumer is given, the electrical consumer is directly supplied with power by the renewable energy source. Surplus electricity from the renewable energy source simultaneously powers the hydrogen generation to produce hydrogen for times of low or no electrical supply. Depending on the specific use, the hydrogen can be reconverted to electricity or directly used.

Another feature of selfHY<sup>®</sup> is the possibility to produce potable water by using the water treatment system of the hydrogen generation and adapting it accordingly. The installation of this feature highly depends on the local fresh water quality and the potable water demand.

With regards to the identification of suitable components and technologies for the subsystems, an overview of the state of the art is elaborated in the following chapter. This forms the foundation for the assessment on different technologies for selfHY<sup>®</sup> leading to the optimal system configuration.



# 3 State of the Art

In this chapter relevant technologies and components for selfHY<sup>®</sup> are identified and the current state-of-art technology is described. Based on the general top level break down of the system from Figure 2.1, the following subsystems and additional components are assessed:

- Renewable energy
- Hydrogen generation
- Hydrogen storage
- Hydrogen reversion (fuel cells)
- Battery storage
- Electrical components.

The subsystem battery storage can be considered as optional for selfHY<sup>®</sup>. If it is determined that a battery is required to run the system in a proper manner (e.g for fast load changes or start-up), it will be added to the concept and sized accordingly. Nevertheless, the initial idea is to develop a concept without battery due to an intended compact design of selfHY<sup>®</sup> and to attempt a proof of feasibility for a self-sufficient energy system only with hydrogen as energy carrier. Moreover, electrical components (e.g. converters and inverters) are described in the state of the art due to their crucial function within selfHY<sup>®</sup>.

## 3.1 Renewable Energy

The renewable energy source is the core driver of selfHY<sup>®</sup>. Depending on the power generation of the renewable energy source, the electricity demand is covered and the possible hydrogen production determined. There are various renewable energy sources, which need to be considered for selfHY<sup>®</sup> and are described in more detail in the following sections.

### 3.1.1 Photovoltaic

In photovoltaic power plants the energy of photons emitted by the sunlight is converted to an electrical current using solar cells. This is possible due to the transfer of energy from the photons of the sunlight to electrons of an atom resulting in the separation of electrons and the creation of an electrical circuit. The carried energy of a photon depends on its wavelength and can be determined by utilizing the solar radiation spectrum (see Figure 3.1) [KONSTANTIN 2013]. Even though the solar radiation spectrum has a wide range, the wavelengths of only two optical windows can reach the earth surface due to the limited transmission of sunlight wavelengths through the atmosphere. One optical

window is found in the low frequency area with wavelengths from  $10^{-2}$  m to  $10^2$  m. The second and more relevant optical window, due to its higher energy levels of the photons, ranges from 0.3 to 5  $\mu\text{m}$ . The high energy photons used for photovoltaic power generation are found in this range at wavelengths from 0.2 to 1  $\mu\text{m}$  [KALTSCHMITT ET AL. 2013].

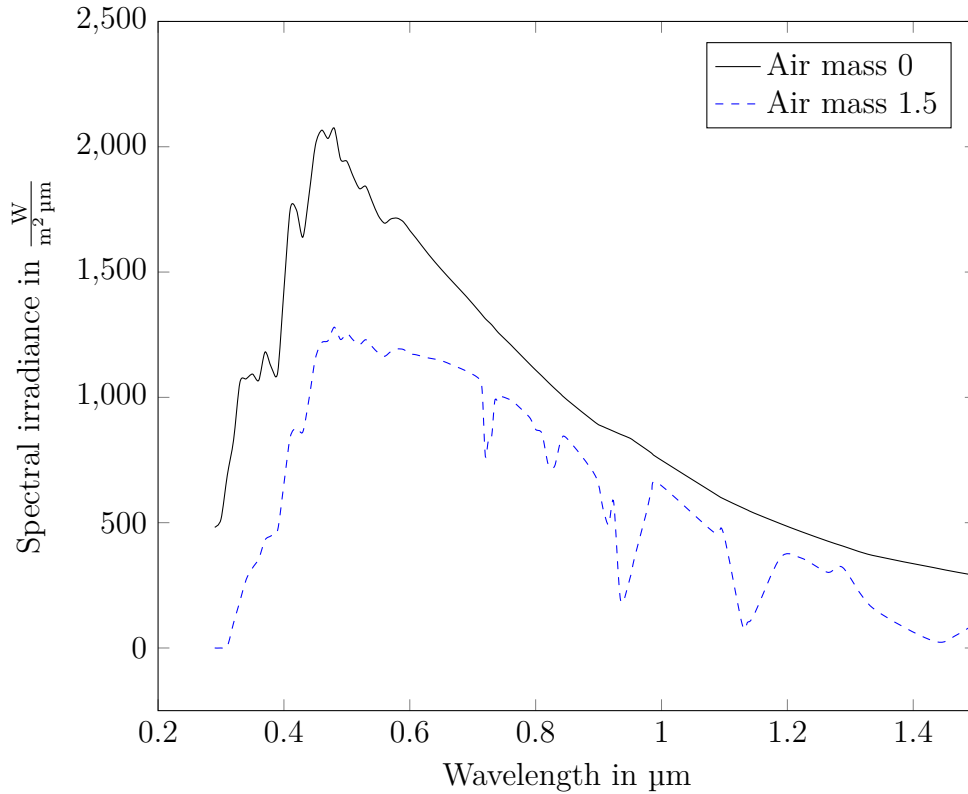


**Figure 3.1:** Solar spectral irradiance for air masses 0 and 1.5 with Ångström turbidity coefficients  $\alpha = 0.66$  and  $\beta = 0.085$  according to MECHERIKUNNEL & RICHMOND 1980

Additionally to the losses in the atmosphere layer, the weather condition, turbulence, humidity and air mass need to be taken into account. Air mass is a measure to describe the amount of air between a light emission source and the receiving point of the light. For air mass 0, it is assumed that no air is present in the path of the light and therefore no transmission losses occur. As shown in Figure 3.1, the air mass factor of 1.5 leads to a lower spectral irradiance due to an inferior angle of the sun with 48.2 degrees from vertical [MECHERIKUNNEL & RICHMOND 1980]. However, the global radiation consisting of the direct and indirect sun irradiation is utilized for the photovoltaic power generation. This is viewed as one advantage compared to solar thermal power generation plants, which can only use direct sun irradiation and are elaborated in more detail in Subsection 3.1.2 [KONSTANTIN 2013].

As now it is clarified where the energy for photovoltaic power originates from, the next step is to understand how the process of electricity generation in solar cells works. The material typically used for solar cells are semiconductors, which permit

electrical conductivity when exposed to light and show insulation characteristics when low temperatures are present. This effect depends on the bandgap width of the material which represents the amount of energy required to move electrons from the valence band to the conduction band. Once the electrons reach the conduction band, the overall conductivity of the material of crystalline character increases. For metals it can be assumed that the valence and conduction band are overlapping and therefore allow metals to have high conductivity even at low temperatures. The opposite is true for insulating materials (e.g. diamonds), which usually have a large bandgap energy  $\Delta W_G$  of above 3 eV leading to low electrical conductivity (see Figure 3.2).

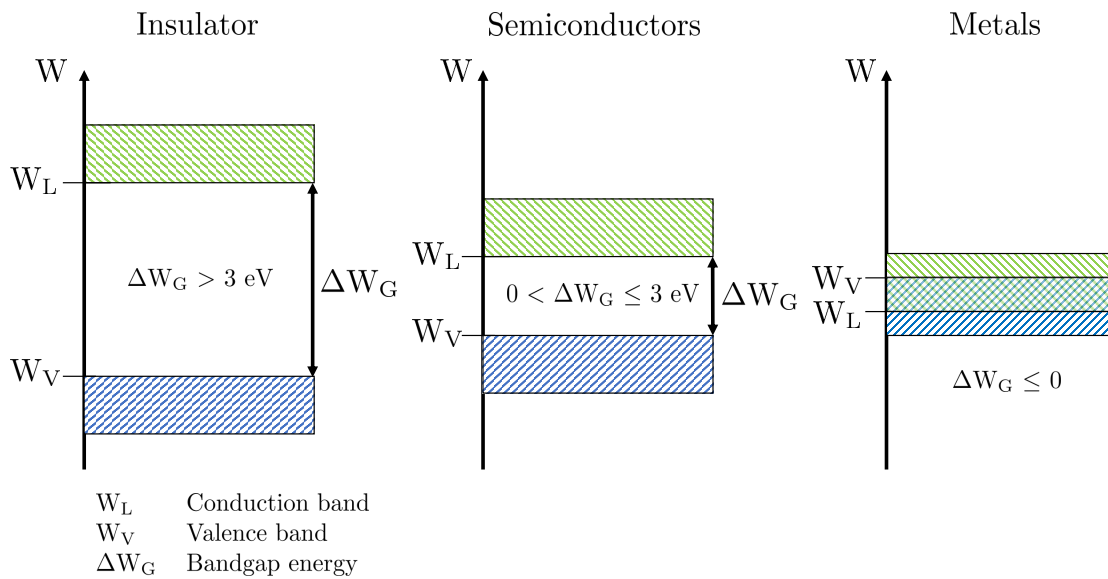


**Figure 3.2:** Energy bands of insulators, semiconductors and metals [MERTENS 2015]

By moving the electron with higher energy to the conduction band, an electron hole pair is generated in the valence band. If an electron falls back from the conduction band to the valence band, a recombination of the electron hole pair occurs. In semiconductors this is a permanent and natural process, which is quantified by the intrinsic carrier density  $n_i$  and depends on the semiconductor material as well as the present temperature (see Equation (3.1)).

$$n_i = N_0 \cdot e^{-\frac{\Delta W_G}{2 \cdot k \cdot T}} \quad (3.1)$$

with  $N_0$  : Density of states in  $\frac{1}{\text{cm}^3}$

$k$  : Boltzmann constant  $\frac{\text{eV}}{\text{K}}$

$T$  : Temperature in K

$\Delta W_G$  : Bandgap energy in eV.

However, semiconductors are not effective conductors until they are combined with foreign atoms in a p- or n-doping leading to similar conductivity characteristics as metals. The n-doping replaces original atoms with elements of the fifth periodic table

group (e.g. phosphor). As a result, free electrons with energy levels very close to the conductivity band are generated (n-doping). The p-doping generates electron holes by implementing elements of the third periodic table group (e.g. boron) resulting in bonding of nearby electrons with the foreign atoms (p-doping).

Both mechanisms combined form a pn-junction, which can be understood as the most simple photodiode. The effect caused by the pn-junction leads to the creation of an electrical field due to the movement of electrons from the n-doped to the p-doped area. As a result a space charge zone on the border between the p-doped and n-doped area is generated, where fixed charge carriers are formed. The initiated voltage is referred to as diffusion voltage  $U_D$  due to the driving force of the concentration difference using energy from the thermal lattice movement. If now photons are absorbed resulting in an increase of electron hole pairs, free electrons and electron holes move towards the outside connections resulting in a photocurrent  $I_{Ph}$  and forming the space charge zone [MERTENS 2015]. This process occurs in a typical solar cell and allows to generate electricity useable for power generation.

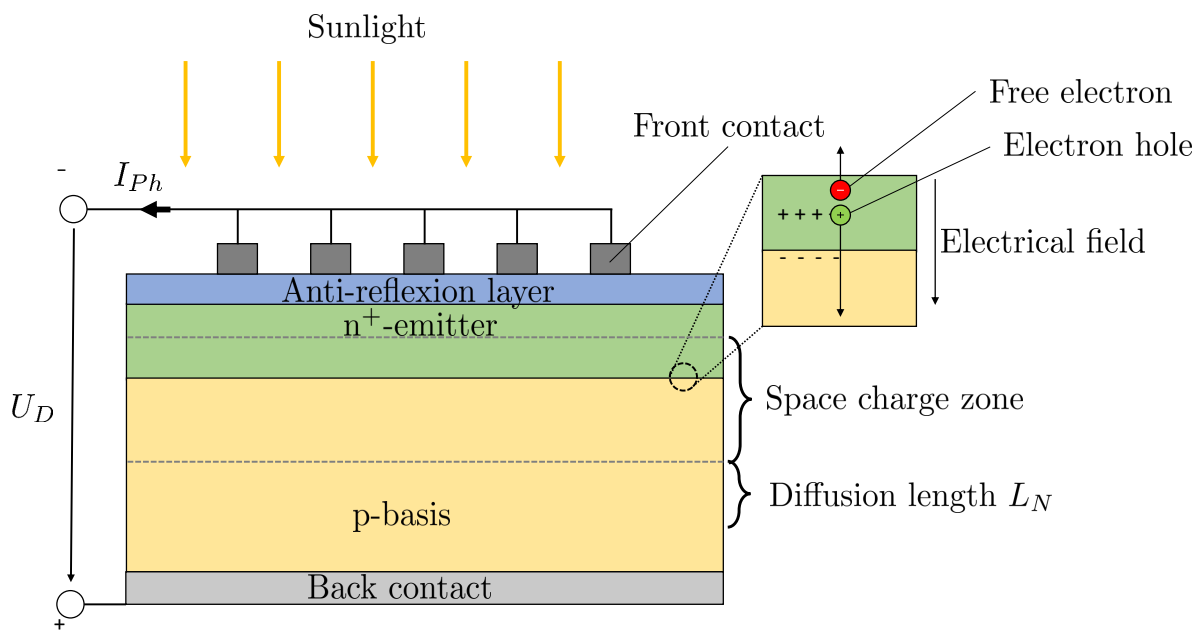


**Figure 3.3:** Structure and photovoltaic processes of a solar cell with characteristics according to MERTENS 2015

As depicted in Figure 3.3, the sunlight passes through the anti-reflection layer and reaches the  $n^+$ -emitter or the p-Basis. Depending on the wavelength of the incoming light different penetration depths are reached, where photons are absorbed. If the photon is absorbed in the  $n^+$ -emitter the likelihood of instant recombination is very high due to the very short diffusion length  $L_N$  in the highly-doped  $n^+$ -emitter. The diffusion length  $L_N$  describes, which distance an electron within a semiconductor can reach until it is recombined.

An absorbed photon in the space charge zone, creates an electron hole pair, which is separated by the electrical field. The electron advances to the  $n^+$ -emitter and further to the negative pole. The hole passes a longer distance through the p-Basis and eventually reaches the plus pole. Thus, the majority of the generated electron pairs in this part of the solar cell are used for the generation of the photocurrent  $I_{Ph}$ .

The important characteristic for the absorption of photons within the diffusion length  $L_N$  is the required occurrence of electron diffusion from the location of the photon absorption in the p-Basis to an area near the space charge zone. On its way, the electron can be recombined, but the likelihood to reach the space charge zone is relatively high as long as it is within the diffusion length  $L_N$ . Once the electron is pulled to the space charge zone the same process as for absorption within the space charge zone occurs. In case the photon is absorbed at a location deeper than the diffusion length  $L_N$ , an electron hole pair is generated but the electron recombines with a hole before reaching the space charge zone having no beneficial contribution to the photocurrent  $I_{Ph}$ . In summary, the diffusion length of electrons within a semiconductor is a crucial parameter for an efficient solar cell. For this reason, the utilization of high-quality crystals with minimal impurities resulting in a higher diffusion length is recommended, so that the absorbed light at deeper locations of the solar cell can also contribute to the photocurrent  $I_{Ph}$  [MERTENS 2015].

Currently, there are different solar cell types available of which the majority is supported by silicon as it is considered the dominant technology in photovoltaic in the world. Undertakings to find more cost-effective and efficient materials (e.g. inorganic, organic and hybrid materials) are on its way [SHARMA & ALI 2020]. Recently, an efficiency of 14.9% was achieved on an area of 1 cm<sup>2</sup> by an improved cell design and use of enhanced high-quality materials [FRAUNHOFER ISE 2020].

The main solar cell types used for industrial photovoltaic power generation can be found in Table 3.1 with an overview of their corresponding efficiencies. To achieve higher power generation, many solar cells are connected to modules. They have slightly lower efficiencies due to higher electrical resistances caused by the connections to multiple solar cells.

**Table 3.1:** Efficiencies of different solar cells and modules according to KONSTANTIN 2013

Material	Cell efficiency in %	Module efficiency in %
Monocrystalline silicon	16 - 22	14 - 20
Polycrystalline silicon	14 - 18	12 - 16
Amorphous silicon	8 - 10	7 - 9
Cadmium telluride (CdTe)	10 - 17	11 - 14
Copper indium aelenide (CIS)	11 - 14	10 - 13

As elaborated earlier, the purity of the crystal has a high influence on the range where the photon energy can be absorbed. Consequently, monocrystalline silicon has the highest efficiency and is therefore in many cases the preferred technical solution.

With worldwide LCOE in 2019 ranging from  $0.04 \frac{\$}{\text{kWh}}$  in India and  $0.14 \frac{\$}{\text{kWh}}$  in Japan, photovoltaic power plants are one of the most cost-effective ways to generate renewable energy. From 2009 to 2019 prices for crystalline silicon modules declined between 87 to 92 % in Europe and a general downward trend in costs for this technology was observed worldwide. With the decrease in costs as the main driver for the improved competitiveness of this technology, more countries (e.g. Vietnam and Ukraine), especially with favorable photovoltaic conditions, consider increasing their photovoltaic energy share [IRENA 2020c]. Moreover, in order to achieve the Paris climate goals a significant scale-up of solar photovoltaic worldwide from 480 GW in 2018 to 2,840 GW installed capacity by 2030 is required, which illustrates the important role of photovoltaic power generation in the future [IRENA 2019a].

### 3.1.2 Concentrating Solar Power

Another technology using the sun directly as energy source is the concentrating solar power technology (CSP). CSP collects and concentrates the radiation from the sun before transforming it to high-temperature thermal energy. The generated energy can be used for numerous thermal applications, but also for electricity production by a steam turbine. One of the advantages is the flexibility of the system to store large amounts of heat intermediately and dispatch it at times when it is needed [BLANCO 2016].

Figure 3.4 depicts a conventional solar-thermal electricity plant with heat storage. The energy from the sun is bundled in the collector and transformed to heat. The generated heat is transferred to a suitable fluid, which is fed to the heat exchangers of the system.

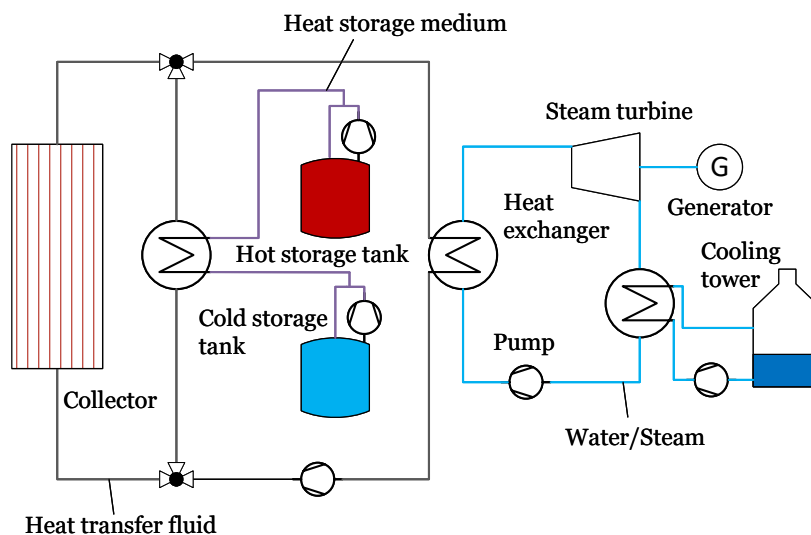


**Figure 3.4:** Schematics of a conventional solar-thermal electricity plant with heat storage according to BLANCO 2016

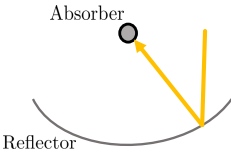
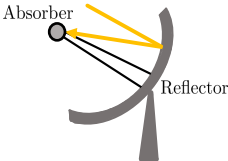
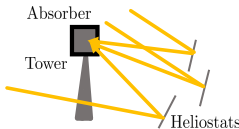
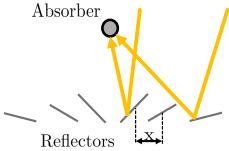
Either the thermal energy is stored in a two tank storage system with different temperature levels or the thermal energy is utilized directly to heat a Clausius-Rankine-Cycle and thereby generating electricity. To maximize the thermal energy available for the process, different concepts for the concentration of the solar radiation have been developed [BLANCO 2016].

The most cost-effective technology with a large number of completed projects are the solar trough power plants. The solar collection field uses reflective troughs, each with a parabolic cross section to concentrate the solar radiation to a tube filled with a heat absorbing fluid [BREEZE 2016].

As opposed to the solar trough power plant, the solar dish power plant does not reflect the solar radiation to a tube, but instead to a single point in the center of the circular reflector. This allows higher intensities and higher temperatures to be achieved. Nevertheless, the limiting factor is the construction of large dish reflectors, which are required for high-capacity generation plants. As a result, only few and relatively small solar dish plants have been constructed to date [BREEZE 2016].

The solar tower uses flat plates or slightly parabolic reflectors, also called heliostats, to focus the solar radiation to an absorber located on the top of a tower. The reflectors are located on the ground and oriented towards the absorber [BREEZE 2016].

Furthermore, a linear Fresnel solar concentrator can be used, which comprises reflectors that are flat or slightly parabolic. Each of the reflectors is laid out in parallel to the ground with a different focal length to its receiver. With increasing distance of reflectors to the absorber, the distance  $x$  (see Fresnel in Figure 3.5) between adjacent reflectors increases as well [BLANCO 2016]. Figure 3.5 summarizes the maximum efficiencies and concentration ratios for the different technologies. The concentration ratio  $C$  describes the ratio between aperture to the absorber area.

Solar trough	Solar dish	Solar tower	Fresnel
			
$\eta_{max} \approx 50 \%$	$\eta_{max} \approx 75 \%$	$\eta_{max} \approx 65 \%$	$\eta_{max} \approx 50 \%$
$C = 50 - 80$	$C > 2000$	$C = 500 - 800$	$C = 50 - 80$

**Figure 3.5:** Overview of technologies for concentrating solar power plants with maximum possible efficiency  $\eta_{max}$  [GIULIANO 2014] and common concentration ratios  $C$  [BLANCO 2016]

The number of installed solar thermal energy capacity increased from 1,266 GW to 6,289 GW over the last decade [IRENA 2020a]. However, with only 0.2% share of installed renewable energy capacity worldwide in 2018 [IRENA 2020b], it is clear that the CSP technology faces limiting factors and challenges. Firstly, it is only

reasonable to install CSP plants in areas with appropriate climate conditions, where direct solar irradiation is predominately present. Consequently, in areas with high shares of indirect solar irradiation CSP plants will not deliver an sufficient energy output to reach acceptable LCOE [QUASCHNING & MURIEL 2001].

Secondly, even though the LCOE for CSP plants has decreased in recent years, it is still more expensive compared to other renewable energy technologies. As an example, a recent study by KOST 2018 has shown that even for areas with high irradiance ( $\approx 2,000 \frac{\text{kWh}}{\text{m}^2}$ ) photovoltaic power plants reach lower LCOE compared to CSP with integrated heat storage of 3,600 full-load hours. LCOE for this specific CSP plant has been calculated below  $0.1 \frac{\text{€}}{\text{kWh}}$ , which is  $0.07 \frac{\text{€}}{\text{kWh}}$  higher compared to the corresponding ground-mounted photovoltaic plant at the same location. Nevertheless, solar thermal technology can be competitive if the heat is used for district heating instead of electricity production. If low electricity prices are present, combined heat and power plants can become unprofitable and be replaced by large-scale solar thermal plants with seasonal heat storage. In Denmark this has become a reasonable use case fostered by local promotion schemes [TSCHOPP ET AL. 2020].

### 3.1.3 Wind

Wind energy can be seen as a secondary form of energy due to its derivation from the sun's uneven heating of the earth surface. Temperature differences cause density and pressure differences, which lead to the movement of air masses. The kinetic energy of this movement can be transformed into electricity [LETCHER 2017]. Today, wind energy is one of the leading renewable energy technologies with a share of 19.1 % of the worldwide electricity generation [IRENA 2020b]. The majority of installed wind turbines are located onshore, but more offshore wind turbines are expected in the future because of favorable wind conditions and the possibility of installing turbines with steadily increasing sizes there. Higher costs for the establishment and maintenance of offshore wind turbines could be compensated by improved efficiencies and higher energy yield [LETCHER 2017].

Wind reaching the blades of a wind turbine causes lift and drag forces along the blade. Depending on the point of action, the intensity of the resulting torque can differ, but as long as a distance between center of rotation and the point of action is given, the wind turbine will rotate [NELSON 2019a]. However, once the wind passes the actuator disc as shown in Figure 3.6, the velocity is decreasing due to the extraction of kinetic energy from the wind by the rotor.

The axial induction factor  $a$  quantifies the efficiency of the rotor and puts the initial wind speed  $V_\infty$  and the wind speed at the rotor disc  $V_D$  in perspective [HEINZELMANN 2011]:

$$a = 1 - \frac{V_D}{V_\infty}. \quad (3.2)$$



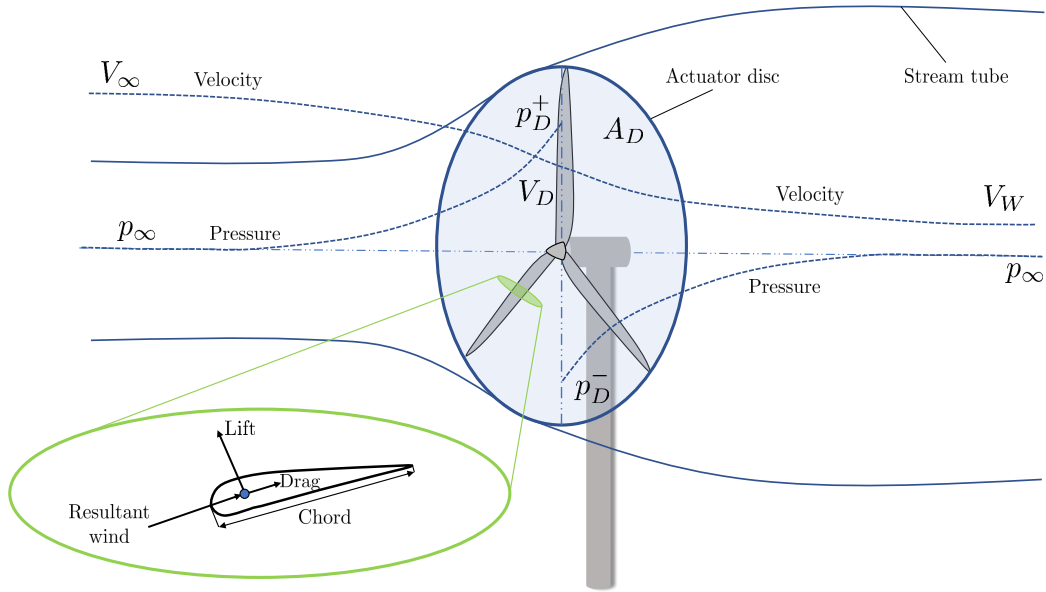


**Figure 3.6:** Wind turbine as energy extracting actuator disc and stream tube according to BURTON ET AL. 2011 with depiction of forces on blade due to airflow of relative wind [NELSON 2019b]

Considering that the rate of change of momentum equals to the overall change of velocity times the mass flow rate, the following correlation can be ascertained, where  $A_D$  is the area covered by the actuator disc,  $\rho_{Air}$  the air density and  $V_W$  the wind velocity downstream of the wind turbine [BURTON ET AL. 2011]:

$$(p_D^+ - p_D^-) A_D = (V_\infty - V_W) \rho_{Air} A_D V_\infty (1 - a). \quad (3.3)$$

Taking also the Bernoulli equation (see Equation (3.4)) into account, which states that under steady condition the total energy flow, consisting of kinetic, static pressure and gravitational potential energy remains constant, the pressure difference ( $p_D^+ - p_D^-$ ) can be obtained [BURTON ET AL. 2011].

$$\frac{1}{2} \rho_\infty V_\infty^2 + p_\infty + \rho_\infty g h_\infty = \frac{1}{2} \rho_D V_D^2 + p_D^+ + \rho_D g h_D \quad (3.4)$$

In case the fluid can be considered incompressible ( $\rho_\infty = \rho_D$ ) and the flow direction is horizontal ( $h_\infty = h_D$ ), the equation can be simplified. The equation is then applied to the downstream and upstream section of the stream tube separately due to the unsteady condition within the actuator disc. Subtracting the equations for the downstream and upstream side results in a simplified term for pressure difference across the actuator disc [BURTON ET AL. 2011]:

$$(p_D^+ - p_D^-) = \frac{1}{2} \rho_{Air} (V_\infty^2 - V_W^2). \quad (3.5)$$

By inserting Equation (3.5) into the correlation for momentum conservation (see Equation (3.3)), it can be concluded that half the axial speed loss in the stream-tube takes place upstream of the actuator disc and half downstream. Equation (3.6) shows the correlation between the initial wind speed and the wind speed behind the wind turbine (see Figure 3.6) [BURTON ET AL. 2011]:

$$V_W = (1 - 2a) V_\infty . \quad (3.6)$$

With regards to the power extraction from the wind, Equation (3.3) can be applied as well for the term of force on the air  $T_W$ . By using the correlation for the wind speed  $V_W$  in Equation (3.6), the force on the air results to [BURTON ET AL. 2011]:

$$T_W = (p_D^+ - p_D^-) A_D = 2 \rho A_D V_\infty^2 a (1 - a) . \quad (3.7)$$

Multiplying the force on the air  $T_W$  with the wind speed at the actuator disc  $V_D$ , the extracted power from the wind  $P_W$  can be calculated [BURTON ET AL. 2011]:

$$P_W = T_W V_D = 2 \rho A_D V_\infty^3 a (1 - a)^2 . \quad (3.8)$$

An important wind design parameter is the power coefficient  $C_P$ , which is the ratio of the useable power from the wind to the theoretically available power of the wind [DAI ET AL. 2016, WATTER 2015]:

$$C_P = \frac{P_W}{\frac{1}{2} \rho V_\infty^3 A_D} = 4 a (1 - a)^2 . \quad (3.9)$$

By differentiating Equation (3.9) in terms of  $a$  and equating it to zero, the maximum and minimum of the function are obtained. The maximum power is reached when  $a = \frac{1}{3}$  (see Equation (3.10)), thus  $C_P$  can reach a theoretical value of up to 59.3 %, also referred to as the Lanchester-Betz limit [BURTON ET AL. 2011].

$$\frac{\partial C_P}{\partial a} = 4 (1 - a) (1 - 3a) = 0 \rightarrow a = \frac{1}{3} \quad (3.10)$$

However, the Lanchester-Betz limit is obviously not a matter of deficiency in design. It is rather a physical circumstance rooting back to the upstream expansion of the stream tube and the resulting smaller area at the upstream cross-section in relation to the actuator disc area [BURTON ET AL. 2011].

In the end, the spinning rotors transfer the kinetic energy from the wind to rotate the low-speed shaft within the nacelle of the wind turbine as shown in Figure 3.7. A gear box, which is coupled to the rotor, transmits the rotary speed from the low-speed shaft to the high-speed shaft so that the correct frequency for the generator is reached. For emergency situations when the rated speed is exceeded, a brake between the gearbox and the high-speed shaft is foreseen. For smaller wind turbines with rotational speeds

in the order of hundreds of revolutions per minute, a direct coupling between rotor and generator without a gearbox might be possible [MCFADDEN & BASU 2016].

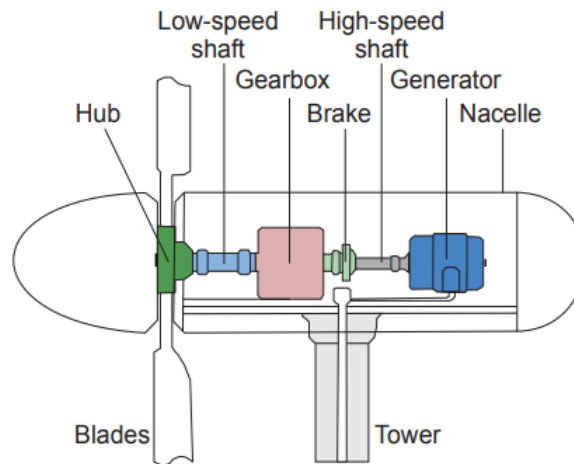


**Figure 3.7:** Overview of basic internal components in the nacelle of a horizontal axis wind turbine according to CENTER FOR SUSTAINABLE SYSTEMS 2020

Modern horizontal axis wind turbines (HAWT) have efficiencies of around 50% and show a steady increase in rotor size and power output over the years. The power output of HAWT ranges from 1 kW with rotor diameters of around 2.5 m to offshore applications with rotor diameters of more than 150 m allowing maximum power outputs of 10 MW. A representative example for the wind turbine scale-up for land-based installations over the last decade is the development in the United States depicted in Figure 3.8 [WISER & BOLINGER 2019, WISER ET AL. 2015, MHI VESTAS OFFSHORE WIND 2018].

This rapid development of wind turbines to one of the most important renewable energy technologies can be traced back to the numerous advantages it brings along. One positive feature is the large area for potential installation areas available, especially offshore. Moreover, wind turbines have shown a substantial cost reduction due to improved design and economy of scale. As a reference, the global LCOE for onshore wind turbines commissioned in 2018 was  $0.056 \frac{\$}{\text{kWh}}$  and for offshore wind turbines  $0.13 \frac{\$}{\text{kWh}}$ . However, noise reduction at onshore sites, interference with nature and stakeholder acceptance represent some of the main challenges for wind turbine technologies [LETCHER 2017, IRENA 2019b].

Research on alternative technologies for wind turbines has been aiming to find more efficient ways to extract the kinetic energy from the wind and possibly overcoming the Lanchester-Betz limit. Also new suitable concepts for wind turbines in specific use cases (e.g. highway electric power generation) are part of modern wind turbine research. The main alternative to HAWTs are vertical axis wind turbines (VAWT), which key advantages are the smaller area, the independency of the wind direction and the possibility of a denser packing of single units compared to HAWTs. However, the

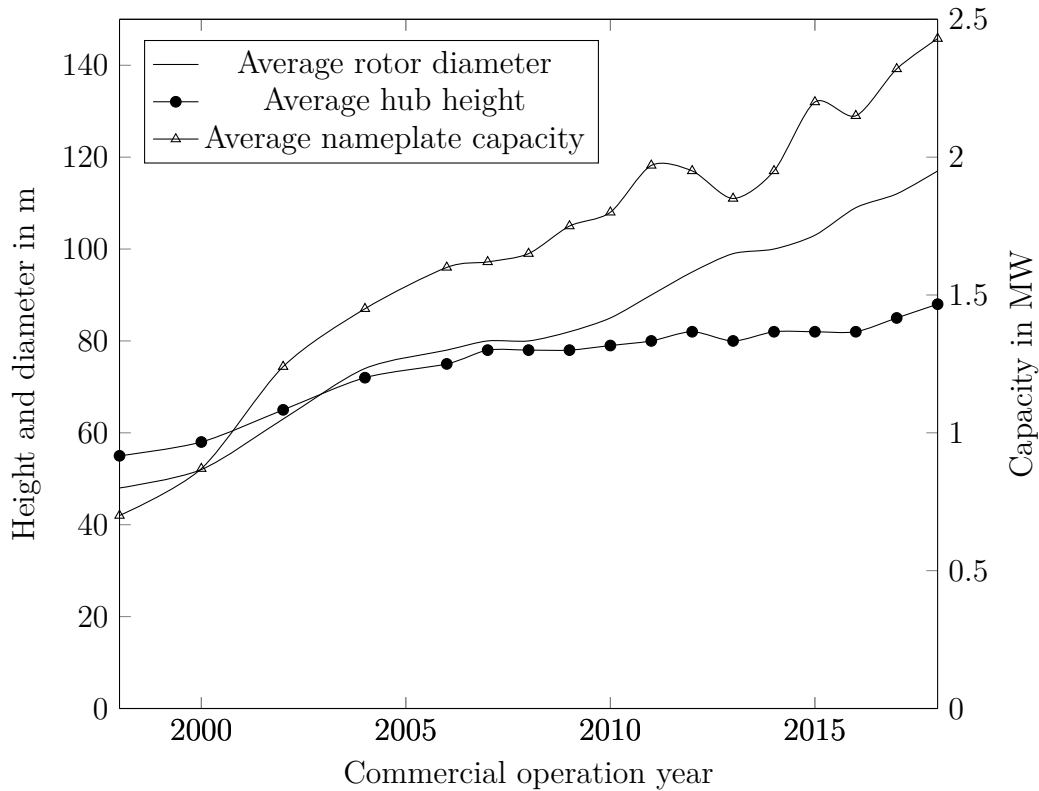


**Figure 3.8:** Wind technology scale-up for land-based wind installations in the United States according to WISER & BOLINGER 2019

relatively slow spinning speed and low efficiency of VAWTs do not allow high power outputs, which would be suitable for large-scale power generation [CORKE 2018].

The Darrieus and the Savonius rotors are the two main configurations for vertical axis wind turbines (see Figure 3.9). The Darrieus wind turbine has the highest efficiency values among VAWTs, but faces problems with regards to low starting torque and possible building integration. Many variants of the Darrieus type wind turbines (e.g. Eggbeater, Giromill, VGOT etc.) are available, all of which are using the lift forces on the blades to rotate the turbine. The other type is the Savonius rotor, which consists of cup-shaped half, hollow cylinders fixed with a central rotating shaft. The drag force acting on the cylinders generates the required torque for the rotation of the turbine [BHUTTA ET AL. 2012].

Vertical axis wind turbines can pose an option for remote locations with low energy demand due to the easy installation, the low complexity of the system and independence of the wind direction [BHUTTA ET AL. 2012, WATTER 2015].

Darrieus rotor    Savonius rotor

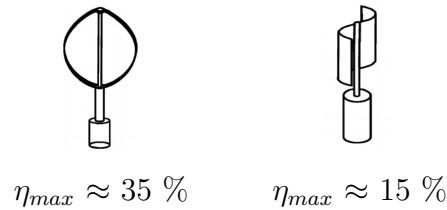


**Figure 3.9:** Main vertical axis wind turbine types [MEHRPOOYA 2014] with maximum efficiencies according to WATTER 2015

### 3.1.4 Hydropower

Hydropower plants are ranging from small-scale modules for isolated locations to hydroelectric power plants with power outputs of more than 10 GW. It is also one of the most established technologies for power generation, which contributed essentially to the development of humanity in the past. Similar to the dependency of solar power generation on solar irradiance, hydropower is limited to areas with natural or artificially created high altitude differences. A typical hydroelectric power plant is shown in Figure 3.10.

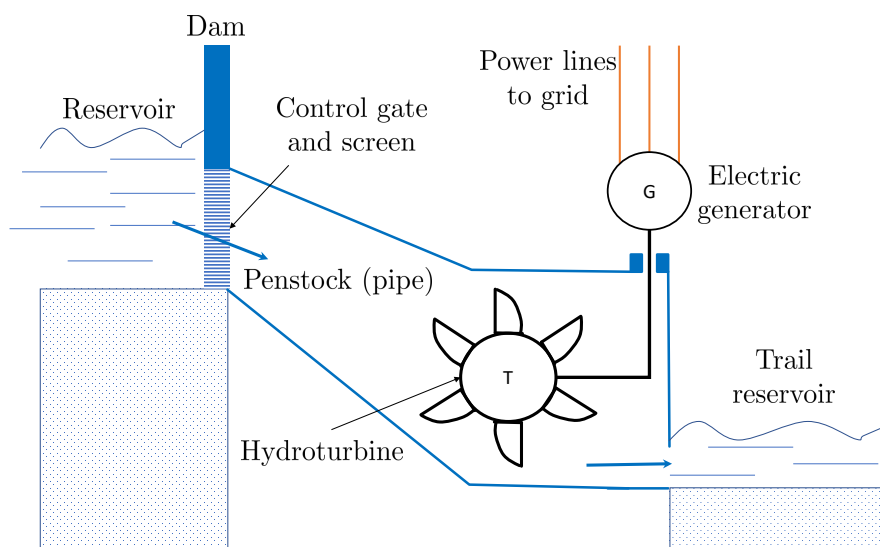


**Figure 3.10:** Cross-section of a typical hydroelectric power facility according to ISMAIL 2017

Water flows from two or more reservoirs from an upper level to the trail reservoir on the lower level due to gravity. The energy from the water flow is extracted with a turbine, which is coupled to a generator producing electricity [ISMAIL 2017, MUNOZ-HERNANDEZ ET AL. 2013].

The most significant operating parameters for hydroelectric power generation are the flow rate and the elevation head. For a steady-state scenario the theoretically available hydropower  $P_{H,th}$  under ideal conditions can be calculated using [ISMAIL 2017]:

$$P_{H,th} = \gamma_W \dot{V}_W h, \quad (3.11)$$

where  $\gamma_W$  is the specific weight for water ( $\approx 9,810 \frac{\text{N}}{\text{m}^3}$ ),  $\dot{V}_W$  the volumetric flow rate and  $h$  the elevation head. Additionally, hydraulic friction losses  $P_{HL}$  in the piping system can be considered:

$$P_{HL} = \varrho_{\text{H}_2\text{O}} \dot{V}_W g \sum H_L \quad (3.12)$$

with  $\sum H_L$  : Total head loss in piping system in m

$\varrho_{\text{H}_2\text{O}}$  : Density of water in  $\frac{\text{kg}}{\text{m}^3}$

$g$  : Gravitational constant =  $9.81 \frac{\text{m}}{\text{s}^2}$ .

The actual available hydropower  $P_H$  can be calculated with [ISMAIL 2017]:



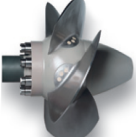
$$P_H = P_{H,th} - P_{HL}. \quad (3.13)$$

The actual available hydropower  $P_H$  represents the maximum possible power in a water flow and is comparable to the restriction of the Lanchester-Betz limit for wind power generation. Additional losses occur on the path from the actual available hydropower  $P_H$  to the electrical power output  $P_E$ . The hydropower plant efficiency  $\eta_{HPP}$  takes into account the efficiency of the hydroturbine  $\eta_{HT}$ , the electric generator efficiency  $\eta_{EG}$  and the electric transformer efficiency  $\eta_{ET}$  resulting in the actual electrical power output [ISMAIL 2017]:

$$P_E = \underbrace{\eta_{HT} \eta_{EG} \eta_{ET}}_{\eta_{HPP}} P_H = \eta_{HPP} P_H. \quad (3.14)$$

Today modern hydropower plants have an efficiency of 85 to 95%, which is regarded as the highest value of all technologies [EURELECTRIC & VGB POWERTECH E.V. 2018]. In particular, the turbine design is crucial for the overall efficiency of the hydropower plant and is chosen by means of the present flow and the head of the specific site location. As depicted in Figure 3.11, there are three main types of hydroturbines with different characteristics [GIESECKE & HEIMERL 2014, MUNOZ-HERNANDEZ ET AL. 2013].

Pelton turbines are considered as impulse turbines using fixed nozzles to convert pressure to kinetic energy of a water jet. Subsequently, the jets of water impinge on the moving plates of the runner where the kinetic energy is used for the rotation of the turbine. An important feature of the Pelton turbine is the absence of change in static pressure across the impeller [MUNOZ-HERNANDEZ ET AL. 2013].

	Pelton turbine	Francis turbine	Kaplan turbine
			
Head in m	100 - 2000	up to 800	5 - 80
Flow in $\frac{\text{m}^3}{\text{s}}$	0.75 - 1000	0.8 - 80	1 - 1000
Power in MW	0.75 - 300	0.05 - 1000	0.05 - 180
Peak efficiency in %	90 - 93	91 - 96	92 - 95

**Figure 3.11:** Overview of hydroturbines with typical application ranges [GIESECKE & HEIMERL 2014, EURELECTRIC & VGB POWERTECH E.V. 2018]

Francis turbines are typical radial reaction turbines, which are radially impinged with a strong swirl of the water flow leading to a further acceleration of the flow within the impeller and a subsequent deflection of the flow to an axial direction. The turbine is controlled by the adjustment of the impeller blade angle, which influences the inflow cross-section and the angle of attack on the impeller [KALTSCHMITT ET AL. 2013]. Francis turbines are utilized for intermediate flow-rates and heights. One advantage is that they can be designed as reversible type, so that pumping of water to the higher reservoirs and turbine operation is possible. For this reason, pumped hydropower plants are usually equipped with reversible Francis turbines, allowing a flexible operation depending on the status of the grid [LAKO & KOYAMA 2015].

The Kaplan turbine is an axial turbine used for higher flows and a comparably moderate head. The specific trait of Kaplan turbines are pitchable impeller vanes, which allow high efficiency over a broad range of operation fields. Moreover, the controlling of the flow can be handled by adapting the pitch angle of the impellers rather than using additional control equipment (e.g. flow control valves). In particular, Kaplan turbines are predestined to be used for hydropower generation at very small scale for remote locations with access to steady water flow (e.g. rivers or irrigation channels) [STOPLE 2011, GIESECKE & HEIMERL 2014].

Moreover, due to the fast response and startup time of minutes, hydropower plants are well suited for peak shaving, which is a term describing the lowering of power generation peaks. One method for this is to power additional electrical consumers (e.g. pumps of pumped hydro reservoirs) to store the surplus energy, hence “shaving” the peak of power generation [LEVRON & SHMILOVITZ 2012, MUNOZ-HERNANDEZ ET AL. 2013]. However, due to the interference in nature, large reservoirs can cause CO<sub>2</sub> emissions, which are lower compared to conventional thermal power plants, but still sufficient to label large-scale hydropower plants as CO<sub>2</sub>-emitting energy sources [SANTOS ET AL. 2006, EURELECTRIC & VGB POWERTECH E.V. 2018].

In conclusion, small scale applications with little impact on the environment cause negligible or no CO<sub>2</sub> emissions. Not only does a mini hydropower plant conserve the environment, but also has potential in remote areas to enable power supply. As one feasibility study for the village of Yuwientsa in Ecuador has shown, even at power scales of around 20 kW, mini hydropower plants can be an option for sustainable electricity generation. The decision on the feasibility of mini hydropower projects highly depends on the local site conditions, the energy demand, the economic situation and the involved stakeholders [ANDERER ET AL. 2010, ZEISELMAIR 2010]. Furthermore, industry leaders have recognized the trend towards an increasing demand on mini hydropower systems and already have respective products in place (e.g. StreamDiver by Voith Hydro), which are needed as basis for a sustainable and self-sufficient energy system in remote areas [VOITH HYDRO HOLDING GMBH & CO.KG 2018].

With 63 % of the worldwide renewable electricity generation in 2018, hydropower accounts by far for the largest share [IRENA 2020b]. As mentioned before the potential of hydropower depends highly on the hydrological and geographical circumstances, which leads to different developments worldwide. Norway, for example, covers almost all of their electricity demand through hydropower due to the very favorable conditions present [HOES ET AL. 2017, ZAHORANSKY ET AL. 2010].

In the last decade the LCOE for hydropower worldwide increased by 21 % from 0.037 to 0.047  $\frac{\$}{\text{kWh}}$  due to more expensive development conditions. This cost rise can be traced back to the more challenging site conditions, in particular for the numerous hydropower projects in Asia [IRENA 2020c]. In summary, hydropower is an important energy source for the future with possible power outputs ranging from couple of kilowatts to hundreds of megawatts. However, it is a site-specific technology, which is limited by geographical and hydrological conditions and its utilization needs to be elaborated in detail prior to a possible project execution [CORÀ 2019].

## 3.2 Hydrogen Generation

The power supplied by the renewable energy source for selfHY<sup>®</sup> is directly used by electrical consumers or for hydrogen generation as shown in Figure 2.1. In the latter case, the produced hydrogen is stored and utilized depending on the energy demand. Hydrogen generation in general can be divided by their sources and method of production as shown in Figure 3.12.

Steam Methane Reforming (SMR) is the most established and cost-effective process to produce hydrogen. Hereby, natural gas, mainly containing methane, reacts with steam at temperatures of 700 to 1,000 °C forming carbon monoxide, carbon dioxide and hydrogen. Downstream the reactor, carbon monoxide further reacts with steam leading to additional hydrogen output. However, for one kilogram of hydrogen, 7 kilograms of CO<sub>2</sub> are emitted in the atmosphere and thereby negatively influencing the climate. Today, less than 0.7 % of hydrogen is produced from renewable energy or reforming



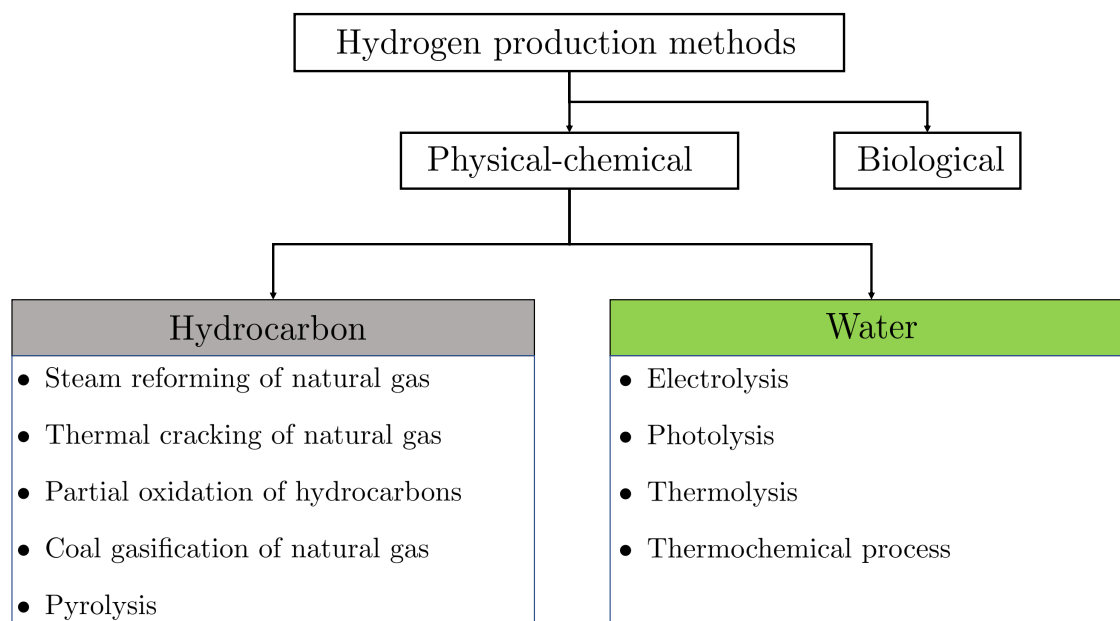


**Figure 3.12:** Overview of hydrogen production methods with typical feedstocks according to KUMAR 2015

processes equipped with CCUS while fossil fuels remain the main source for hydrogen production [BASSANI ET AL. 2020, KUMAR 2015].

All other methods to generate hydrogen without carbon emission can be considered as less relevant due to low technology readiness levels and lack of utilization in commercial applications [INTERNATIONAL ENERGY AGENCY (IEA) 2019, KUMAR 2015].

Electrolysis powered by renewable energy is a sustainable option to generate hydrogen without CO<sub>2</sub> emission and it is expected to gain more importance in the future. Many hydrogen strategies published in recent years include the goal of up-scaling electrolyzer capacities. By 2025 it can be expected that countries with 80 % of global GDP will have hydrogen strategies in place, providing the framework for the development of a hydrogen economy [ALBRECHT ET AL. 2020].

Moreover, the development of a regulation for transparent guarantees of hydrogen origin is an important task for fostering hydrogen as energy carrier. Therefore, initiatives by many companies in the hydrogen field have been undertaken to categorize hydrogen production methods according to their emission intensity. On European level, CertifHy<sup>®</sup>, a project funded by the FCH 2 JU, aims at developing a framework for guarantees of origin for green and low-carbon hydrogen. Currently, CertifHy<sup>®</sup> is focusing on ensuring the compatibility with EU legislation. According to CertifHy<sup>®</sup> the origin of the hydrogen and its greenhouse gas (GHG) intensity is taken into account resulting in three possible labels for hydrogen production methods.

As depicted in Figure 3.13, there are two labels defined for hydrogen with greenhouse gas intensity that is lower than the benchmark by at least 60 %. All hydrogen production methods above a threshold of 40 % of the greenhouse gas emissions produced by a

state-of-the-art natural gas steam methane reformer are labeled as not low-carbon. For low-carbon hydrogen there is an additional division by the origin of energy for hydrogen production. If hydrogen is produced by using renewable energy, it is labeled as green hydrogen, otherwise as low-carbon hydrogen [FUEL CELLS AND HYDROGEN JOINT UNDERTAKING 2019].

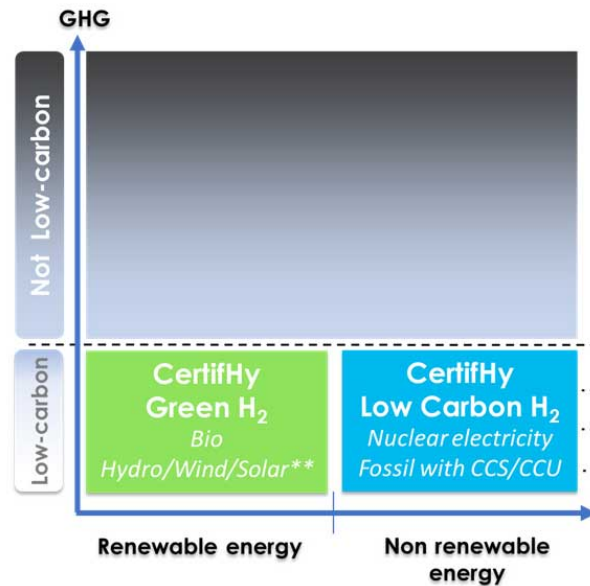


**Figure 3.13:** Labels for hydrogen production methods according to FUEL CELLS AND HYDROGEN JOINT UNDERTAKING 2019

With regards to selfHY<sup>®</sup> only green hydrogen production methods are relevant due to the intention of developing a sustainable energy system with zero CO<sub>2</sub> emissions. Thus, water electrolysis is the eligible green hydrogen process for selfHY<sup>®</sup>, which consists in general of a water treatment, electrolysis and hydrogen purification process and will be described in the following subsections [NIKOLAIDIS & POULLIKKAS 2017].

### 3.2.1 Water Treatment

Water treatment is the first step of the hydrogen generation process and relevant to ensure long-term operability of the electrolyzer and consistent efficiency of the process. The main goal of water treatment is to sufficiently purify the feed water for the subsequent electrolysis process. For this reason, all organic matter, particles, dissolved gases and even ions need to be removed prior to reaching the electrolysis cells in which the reaction takes place. Depending on the quality of the feed water, different methods and technologies are required for water purification.

In general, the target is to remove all ions from the feed water, thereby producing demineralized water with an electrical conductivity below  $1 \frac{\mu\text{S}}{\text{cm}}$  and without any harmful substances for the electrolysis process. Even though the international standard for hydrogen generators using water electrolysis ISO 22734 leaves the definition of the feed

water quality for a hydrogen generator solely up to the manufacturer, it is recommended to ensure a minimum water quality in accordance with ASTM D 1193 Type II Deionized Water [BLUMENTHAL 2020, NEL ASA 2019].

Different water sources are used as feed water for hydrogen generation, which can differ gravely in its composition. Sea water is considered as one of the most difficult to treat for hydrogen generation due to the high number of dissolved solids and the elaborate purification process connected to it. Nevertheless, large desalination plants are being used to purify sea water to potable water in areas with water scarcity and also concepts for stand-alone solutions at smaller scale are objects of current research [CLARKE 2015, GHERMANDI & MESSALEM 2009].

Moreover, waste water, brackish water and sweet water from rivers, lakes or ground are possible water sources and require fitted water treatment solutions for hydrogen generation [ISLAM ET AL. 2018].

Feed water can contain numerous harmful pollutants (e.g. heavy metals, dyes, pharmaceuticals, fluoride or arsenic) potentially causing negative effects on the electrolysis process if not previously removed [BONILLA-PETRICIOLET ET AL. 2017]. Due to the wide range of possible pollutants and their different chemical and physical characteristics, suitable methods need to be utilized in order to reach the desired water quality for hydrogen generation. The most common methods and technologies utilized in water purification systems for hydrogen generation will be explained in more detail in the following, starting with the membrane technologies.

As shown in Figure 3.14, there are different membrane processes ranging from solute sizes of 10,000 to 0.1 nm. The membrane processes are categorized in microfiltration, ultrafiltration, nanofiltration and reverse osmosis (RO) [BONILLA-PETRICIOLET ET AL. 2017].

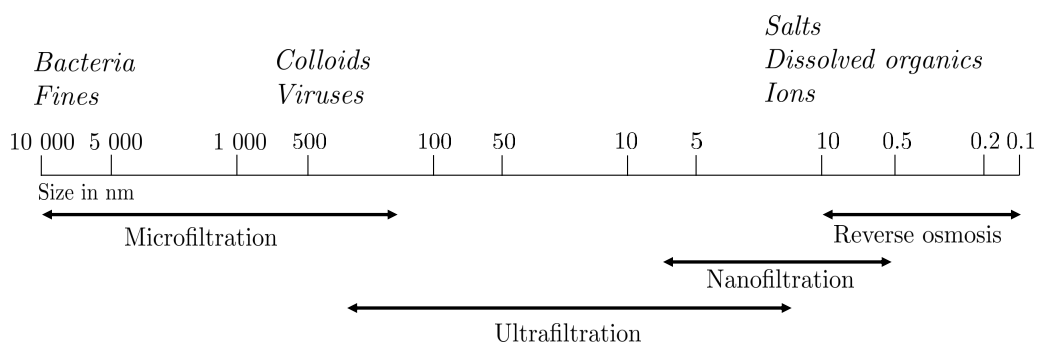


**Figure 3.14:** Overview of membrane processes according to SINGH 2015

For all four relevant membrane processes, the driving force is the pressure difference between two homogeneous phases, which are separated by a permselective barrier (see Figure 3.15). Each represents a steady-state operation at different pressure levels consisting of three streams: feed, product or permeate and reject or retentate. Depending

on the characteristics of the membrane, components are able to pass through or are rejected and removed from the process.

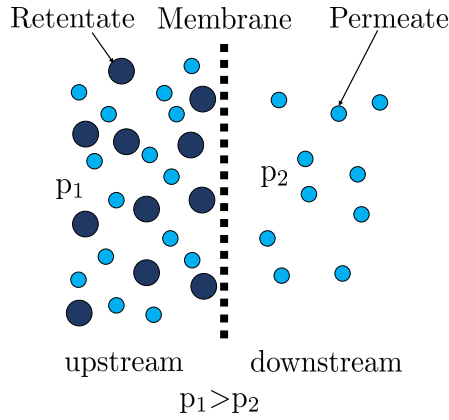


**Figure 3.15:** Basic membrane process according to SARBATLY 2020b

For the purification of water for hydrogen generation, the reverse osmosis is the most relevant treatment due to the high efficiency of ion and salt rejection required for the low electrical conductivity of the water. Each membrane installed is unique and shows differences in structure and basic characteristics such as porosity, pore size, pore size distribution, surface roughness, tortuosity and thickness. These characteristics influence the process parameters such as the flux, permeability retention and recovery rate. Due to the pressure difference being the driving force of the separation, the flux can be expressed as [SINGH 2015, SARBATLY 2020b]:

$$J_T = \frac{\Delta p}{\mu_T R_T} = K \frac{\Delta p}{l} \quad (3.15)$$

with  $J_T$  : Flux at operating temperature in  $\frac{\text{kg}}{\text{m}^2 \text{ s}}$

$\Delta p$  : Transmembrane pressure in Pa

$\mu_T$  : Viscosity at operating temperature Pa s

$R_T$  : Total resistance in the membrane system  $\frac{\text{m}^2}{\text{kg}}$

$K$  : Membrane permeability constant  $\frac{\text{mol}}{\text{m s Pa}}$

$l$  : Membrane thickness in  $\mu\text{m}$ .

As it is depicted in Equation (3.15), the flux is inversely proportional to the membrane thickness leading to higher flux rates at smaller membrane thicknesses provided the other parameters remain constant. As an example, Loeb–Sourirajan RO membrane produced by the phase-inversion technique have an effective skin thickness of 0.1 to 0.2  $\mu\text{m}$  at feed pressures of 30 to 60 bar resulting in fluxes of 2 to 20  $\frac{\text{L}}{\text{m}^2 \text{ h}}$ . For ultrafiltration the flux is estimated to be 7.5 times higher due to larger pore sizes of the membranes used. As a result, the control of the membrane morphology with the goal to avoid introducing defects is an important aspect to consider during fabrication [SINGH 2015].

Membranes for RO usually have a pore radius of 0.6 nm enabling pure water molecules with a radius of 0.1 nm to pass through the membrane freely while salts and organic solutes remain on the pressurized side. The retentate either is rejected at the membrane surface or bonds with solvents in the water phase. In both ways it is removed from the process flow and disposed. The ratio between the permeate flow  $f_P$  for hydrogen generation and the feed water flow  $f_{Feed}$  is defined as the recovery rate  $RR$  and is regarded as one of the key performance indicators. Typically, a recovery rate  $RR$  of around 50 % per array is common for RO [SINGH 2015, DESHMUKH 2020]:

$$RR = \frac{f_P}{f_{Feed}}. \quad (3.16)$$

In case the membrane features a non-porous structure, the dominant transport mechanism changes from convective flow, which is the characteristic mechanism for reverse osmosis, to a pore-free solution-diffusion in the membrane polymer used for describing the transportation mechanisms in gas separation and pervaporation. Besides the already noted membrane separation processes in Figure 3.15, there are various others, e.g. dialysis or electro dialysis to mention.

However, they are not further analyzed due to insignificant relevance in the water treatment for hydrogen generation. In summary, the membrane performance in a RO system is a trade-off between membrane selectivity, which is defined as the ratio of the water permeability and solute permeability coefficient, and the desired permeate flux. RO removes typically 98 % of all TDS and TOC and is therefore considered the key component of the water treatment system for hydrogen generation [SINGH 2015, SARBATLY 2020b].

Even though the RO part is the central element of the water treatment system for hydrogen production, other components are required to reach the optimal water quality for the RO. Prior to reaching the RO system larger particles, e.g. sands, need to be removed from the water flow. This can be performed by dual media filters, which use a filter media, e.g. a combination of gravel, sand and anthracite media, to trap suspended solids in the interstitial spaces.

In some cases an additional upstream rack is installed to prevent clogging or damage by large non-biodegradable solids (e.g. plastics, papers or rags), which have been dragged into the water flow. Similarly, a fine filter sieve with pore ratings of 3 to 5  $\mu\text{m}$  is usually located upstream the RO in order to remove particles, which would otherwise block the feed spacer [DESHMUKH 2020, MATTER 2018, THOMAS MELIN 2007, SARBATLY 2020a].

Moreover, if the feed water contains larger amounts of chlorine, activated carbon filters can be utilized to remove free chlorine as well as adsorbing organic compounds. On the contrary, it needs to be considered that chlorine is an effective agent for removing microbial pathogens, which is especially relevant for potable water treatment. Another option for water disinfection and removal of biological traces in the water is the use of UV light, although it has limited effects for water with high levels of suspended solids,

turbidity or soluble organic matter. In general, UV sterilization aims at the reduction of biological organisms and is able to remove 99.5 % of bacteria and organic compounds within the water flow. UV light operates with different wave lengths depending on the primary function of the system. At wave lengths of 185 nm, UV light typically reduces organic compounds while at wave lengths of 254 nm bacteria is mostly destroyed [DESHMUKH 2020, MATTER 2018, BONILLA-PETRICIOLET ET AL. 2017, SARBATLY 2020a].

Another important process step of the water treatment for hydrogen generation is the water softening unit. It adapts the water hardness by exchanging calcium and magnesium ions with sodium or potassium ions and therefore reduces the likeliness of potential scaling of the RO membranes [DESHMUKH 2020, SCHOLZ 2006].

Depending on the required water quality after RO, additional ions can be removed from the water stream in a electrodeionization (EDI) unit, where ion exchange resins are constantly using electricity to regenerate. The removed ions are pulled from the resins by charged electrodes rejecting 5 to 10 % of the feed water. In case larger amounts of TDS are within the feed water, for example due to an ineffective RO, the EDI unit would likely suffer from fouling by salt formation at the membranes [DESHMUKH 2020]. Based on the elaborated components for water treatment in hydrogen generation, Figure 3.16 shows an exemplary general scheme of such a system with potable water as feed stream.

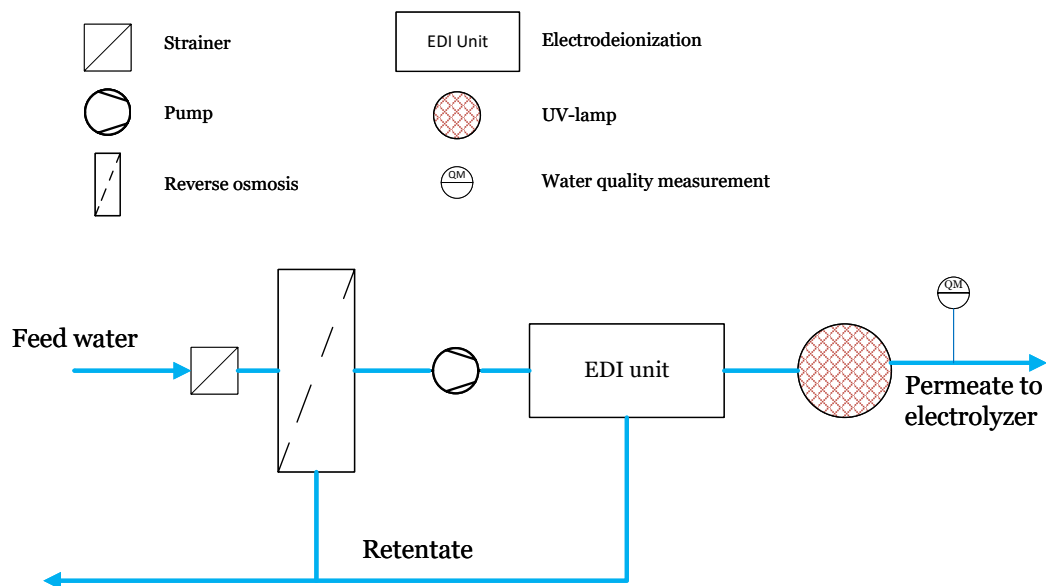


**Figure 3.16:** General scheme of possible water purification system for hydrogen generation

However, the optimized design of the water purification system depends highly on the composition of the feed water and the required purity of water for the specific electrolysis technology. Water treatment for hydrogen generation still poses challenges, thus new technologies and membranes, e.g. for direct electrolysis from sea water as

described by TONG ET AL. 2020, are being researched in order to possibly reduce or even eliminate the need for conventional water purification systems in the future.

### 3.2.2 Electrolysis

In the electrolysis process purified water is split into hydrogen and oxygen using electrical current. There are currently four relevant technologies, of which the most established one is the alkaline electrolysis (AE<sup>1</sup>). Over recent years new technologies, i. e. proton exchange membrane electrolysis (PEME) and solid oxide electrolysis (SOE), entered the commercial hydrogen generation field gaining constantly in relevance. One of the newest technologies commercially available in small scale is the anion exchange membrane electrolysis (AEME), which is expected to gain importance due to merging advantages of PEME and AE [SCOTT 2020, NAVARRO ET AL. 2015, VINCENT & BESSARABOV 2018].

Regardless of the electrolysis technology for hydrogen generation, the overall chemical reaction remains the same. Water molecules are decomposed to hydrogen and oxygen by applying voltage to cells resulting in a direct current between two electrodes and the following overall reaction [SCOTT 2020, IDRIS ET AL. 2015]:



The minimum cell voltage required to initiate the separation of water molecules and maintain the reaction is referred to as thermoneutral voltage  $U_{th}$ . It is defined as the ratio of the reaction enthalpy  $\Delta_R \bar{H}$  and the product of the Faraday constant  $F$  with the number of exchanged electrons  $z$  and takes the irreversible thermal losses into account:

$$U_{th} = -\frac{\Delta_R \bar{H}}{zF}. \quad (3.18)$$

For standard conditions with  $\Delta_R \bar{H} = 286 \frac{\text{kJ}}{\text{kmol}}$ , the thermoneutral voltage results to  $U_{th} = -1.48 \text{ V}$  [BRAUNS & TUREK 2020, NAVARRO ET AL. 2015]. In order to operate an electrolyzer efficiently, the cell voltage should be as close as possible to the thermoneutral voltage at the given conditions. In general, the cell efficiency depends on the reversible thermodynamic decomposition voltage, anode and cathode overpotential as well as the ohmic drop across the cell. Modern electrolyzer cells run with 1.8 to 2 V at high current densities of 0.3 to 1  $\frac{\text{A}}{\text{cm}^2}$  [LEE ET AL. 2020, NAVARRO ET AL. 2015]. However, there are different electrolysis technologies to achieve this reaction, which are classified based on the applied electrolyte and are presented in the following sections [ZHANG 2020].

<sup>1</sup> Although in scientific literature the abbreviation AEL is commonly used for alkaline electrolysis, in this work the abbreviation AE is utilized for purpose of consistency while comparing other electrolysis technologies.

### 3.2.2.1 Alkaline Electrolysis

Alkaline water electrolysis is the longest commercially available electrolysis technology. It uses a 20 to 40 % KOH solution at operating temperatures between 60 to 90 °C to provide sufficient ionic conductivity for the process. In most cases two nickel-based electrodes immersed in the alkaline electrolyte are divided by a diaphragm only allowing  $\text{OH}^-$  ions to pass through from the cathode to the anode. Hydrogen is generated at the cathode side according to the hydrogen evolution reaction (HER) in Equation (3.19) and the  $\text{OH}^-$  ions react to oxygen on the anode side in the so called the oxygen evolution reaction (OER) (see Equation (3.20)) resulting in the overall reaction in Equation (3.17).



Another task of the diaphragm, besides allowing only  $\text{OH}^-$  ions to pass, is to ensure that no short circuits between the electrodes can occur, as well as to avoid gas crossover when operating at balanced pressure.

Modern alkaline electrolyzers use a zero-gap design (see Figure 3.17) in order to reduce the ohmic voltage drop across the cells [HAUG 2019].

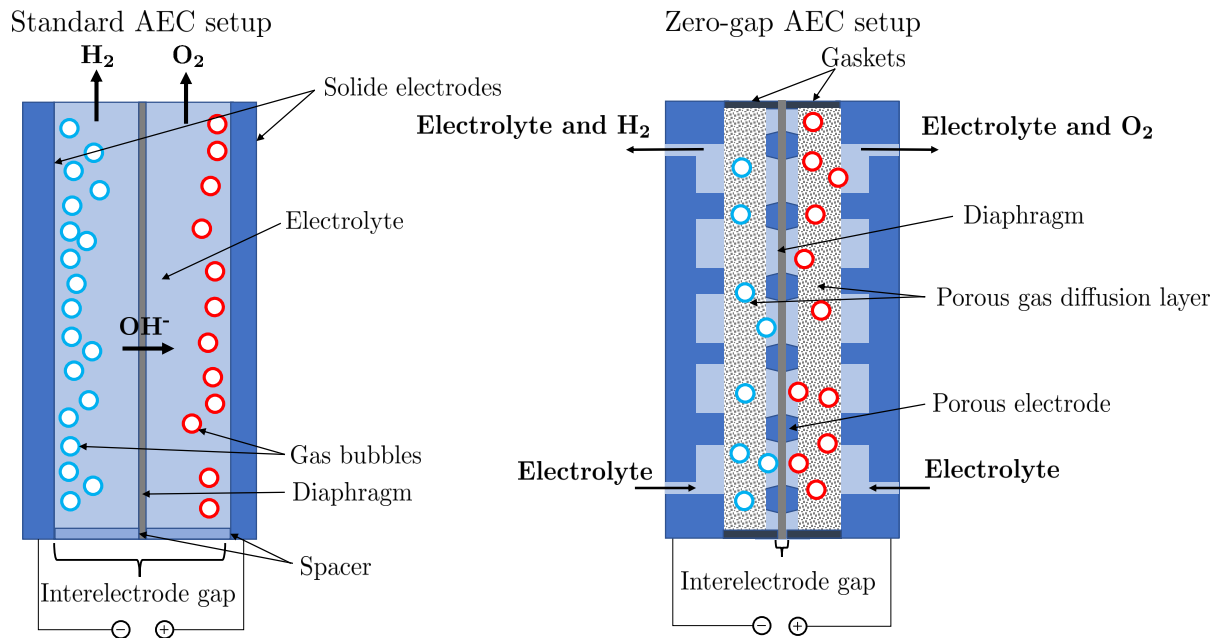


**Figure 3.17:** Alkaline water electrolysis with standard and zero-gap setup [HAUG 2019, PHILLIPS & DUNNILL 2016]

Traditional alkaline electrolysis suffers from low current densities of below  $0.25 \frac{\text{A}}{\text{cm}^2}$  with efficiencies typically of up to 60 %. However, the use of cheap and abundant metals for catalysts and other cell components still pose major advantages compared to other more



costly technologies such as PEME (see Subsection 3.2.2.2). In order to improve the efficiency and in particular to reduce the ohmic resistance across the cell, the zero gap cell design (see Figure 3.17) has been developed for the alkaline environment. As defined by name, this design reduces the gap between the two electrodes from approximately more than 2 mm to less than 0.5 mm.

Additionally, this setup uses a gas diffusion layer to provide an electrical connection from the porous electrode to the bipolar plate, while feeding the electrolytic solution and removing gas products at the same time. Moreover, gas bubbles are forced to the outside also leading to a positive effect on the cell voltage. The design optimization of alkaline electrolysis focuses on three main areas: catalysts, diaphragm and cell design, all of which influence the efficiency and costs of the cell. Catalysts for AEC have been researched in the past extensively leading to the conclusion by PLETCHER & LI 2011, LI ET AL. 2011 of Ni-Mo being currently the best catalyst for the cathode and NiFe(OH)<sub>2</sub> for the anode. The diaphragm's main characteristic are effective gas separation capabilities with low electrical resistance and long stability in the alkaline environment.

Furthermore, the constructional design optimization of the cell, which is connected to the manufacturing and assembling techniques of the stacks, leaves room for improvement. However, the challenges of AEC have encouraged the research for alternative technologies [PHILLIPS & DUNNILL 2016]. One promising technology is PEME, which shows advantages in hydrogen production when combined with intermittent renewable energy sources.

### 3.2.2.2 Proton Exchange Membrane Electrolysis

Key advantages of the PEMEC are higher power densities, high cell efficiencies, flexible operation and the possibility to operate the cell at higher, unbalanced pressure to produce pressurized hydrogen during the generation process [SCHMIDT ET AL. 2017]. The downside of the latter is possible cross-permeation of the product gases through the membrane due to higher pressure. In particular, for pressures above 100 bar, thicker membranes and internal gas combiners are required to prevent critical conditions. Although the PEMEC operates at similar temperature levels as the AEC (< 100 °C) (see Subsection 3.2.2.1), the main difference is the high proton conductivity resulting in current densities beyond  $2 \frac{\text{A}}{\text{cm}^2}$ . Another disparity is the nature of the reaction, which requires a stable and highly acidic environment provided by the proton exchange membrane for the catalyst. Under these harsh conditions, usually platinum metal is utilized as catalyst in the HER (see Equation (3.21)) and iridium oxide for the OER (see Equation (3.22)). Such scarce and noble catalysts are a main cost factor

for manufacturing PEME cells and represent one of the main challenges for PEME technology [ZHANG 2020, CARMO ET AL. 2013].

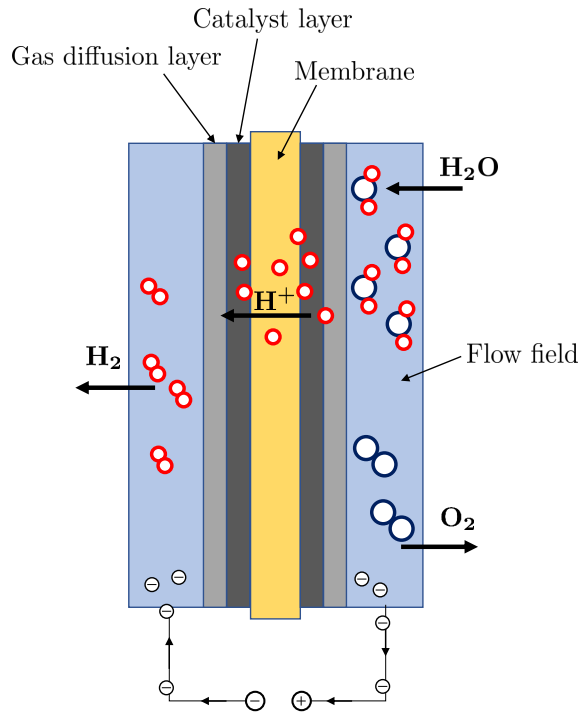


**Figure 3.18:** General schematic and process of proton exchange membrane electrolyzer cell according to SELAMET ET AL. 2011, MARTINSON ET AL. 2014

As depicted in Figure 3.18, purified water enters on the anode and the electrical current is applied to the molecules leading to the separation into protons, electrons and oxygen. The oxygen is released from the process while the electrons and protons recombine at the cathode to hydrogen [MARTINSON ET AL. 2014]. The core mechanism to enable this process is the passing of the protons through the membrane. While PEME can respond quickly to power input changes, AE is limited due to the inertia of the liquid electrolyte. This feature of PEME is beneficial for hydrogen production with renewable energy, where the power input is naturally fluctuating.

Moreover, the safety aspects regarding the gas crossover rate needs to be considered. In part load the rate of hydrogen and oxygen production decreases, but the permeability of the membrane remains constant leading to accumulation of hydrogen on the anode side, thus potentially creating a safety hazard [CARMO ET AL. 2013].

### 3.2.2.3 Solid Oxide Electrolysis

As opposed to the low temperature electrolysis, the SOE is utilized for high temperature electrolysis with operating temperatures in the range of 700 to 900 °C. SOE uses steam as water source and therefore requires less energy to be introduced to the electrolysis process compared to low temperature electrolysis with water. By splitting the water molecules at high temperatures, less reaction enthalpy compared to the AEC and PEMEC is required and operation at thermoneutral voltage gets economically viable, which leads to an overall higher efficiency. Moreover, the high temperatures lead to favorable conditions for conductivity at the electrodes resulting in reduced electrode overpotentials [MOUGIN 2015, LAGUNA-BERCERO 2012].

On the contrary, challenges regarding the stability of materials and sealing issues arise as well as the need for higher investments for an elaborate hydrogen purification unit due to the necessity of steam removal in the hydrogen production stream. Nevertheless, the main challenge remains the long-term stability of the cell, which is caused by comparably fast electrolyte aging and electrodes deactivation [URSUA ET AL. 2012].

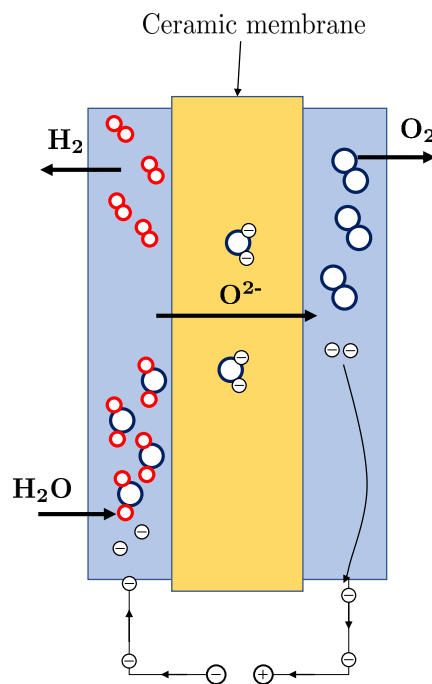


**Figure 3.19:** General schematic and process of solid oxide electrolyzer cell according to URSUA ET AL. 2012

Figure 3.19 shows the principle in a typical SOEC. Water is split to hydrogen and oxygen ions at the cathode side. Latter are transported to the anode side through the solid oxide electrolyte, recombining there to oxygen molecules. The HER (see Equation (3.23)) and

OER (see Equation (3.24)) describe the processes on the electrodes [LAGUNA-BERCERO 2012].



The promising feature of SOEC compared to other electrolysis technologies is the possibility of reversible operation allowing electrolyzer as well as fuel cell operation. This dual-use permits higher operating hours with minimized investment costs leading to a higher return on investment [MOUGIN 2015]. However, the commercialization of reversible solid oxide cells is currently still limited due to severe degradation of the electrodes during electrolysis operation [KHAN ET AL. 2020].

### 3.2.2.4 Anion Exchange Membrane Electrolysis

The AEMEC can be regarded as a mixture of AEC and PEMEC combining their advantages but also leading to new challenges. While the hydrogen is generated at the cathode side,  $\text{OH}^-$  ions pass to the anode side forming oxygen, identically to the process in a AEC. However, the electrode chambers are separated by a thin, dense and porous polymer membrane as in PEMEC. The main motivation for development of AEMEC is the possibility to use abundant material combinations as catalysts and thereby reducing costs while still benefiting from high current densities, fast response times and a compact system with large operational capacity.

However, one of the issues of anion exchange membranes is the 3 to 10 times lower ionic conductivity compared to proton exchange membranes (e.g. Nafion<sup>®</sup>). By increasing the ionic conductivity through addition of functional groups within the polymer, the chemical degradation rate rises accordingly due to higher water absorption causing nucleophilic substitutions of the functional groups. As a result, current research strategies to increase the ionic conductivity of the membrane are based on suppressing this mechanism and handling the degradation processes under alkaline conditions in an AEMEC. The HER and OER are identical to the AEC reaction (see Equation (3.19) and 3.20) and the structure of the cell is depicted in Figure 3.20 [HENKENSMEIER ET AL. 2020, HÖFNER 2016].

Today's AEM electrolyzers use a water feed with electrolytes (e.g.  $\text{HCO}_3^-$ ) or dilutes (e.g. KOH) in order to obtain sufficient performance. With improvements of the anion exchange membrane and the shift towards the use of demineralized water, an increase in the overall performance and efficiency of the AEMEC is expected. Recent developments in the AEMEC research have reported current densities of  $0.47 \frac{\text{A}}{\text{cm}^2}$  using a 1%  $\text{K}_2\text{CO}_3/\text{KHCO}_3$  feed at 50 °C with PGM-free catalysts [MILLER ET AL. 2020]. Commercially available electrolyzer modules are restricted to small scale applications. As an example the electrolyzer EL 2.1 by Enapter with a power input of 2.4 kW and hydrogen output of  $0.5 \frac{\text{Nm}^3}{\text{h}}$  can be used for energy storage systems for integration in a

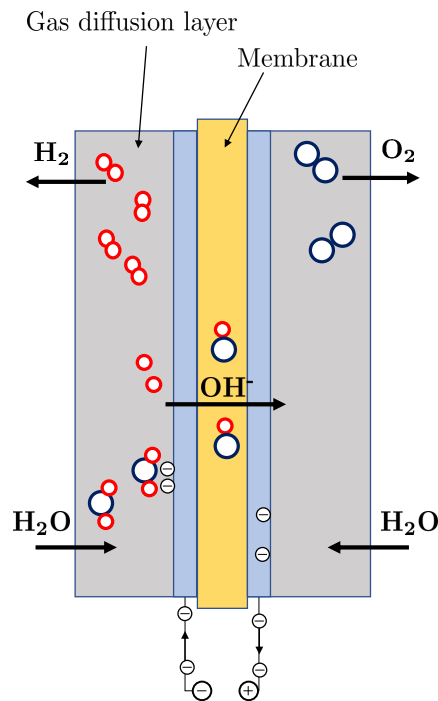


**Figure 3.20:** General schematic and process of anion exchange membrane electrolyzer cell according to MILLER ET AL. 2020

remote microgrid. Nevertheless, AEME technology is still at a research and development stage when larger stack sizes and hydrogen outputs are needed [CHROMETZKA ET AL. 2020, MILLER ET AL. 2020].

### 3.2.3 Hydrogen Purification

The produced hydrogen from the electrolyzer still has traces of water, oxygen and possibly nitrogen in it. In order to reach the required hydrogen quality for the specific application, a purification unit is included in the hydrogen generation process.

There are many existing methods of purifying hydrogen which include combinations of mechanical compression with cryogenic cleanup, palladium membranes and passive membrane separators [PINGITORE ET AL. 2017]. However, aiming to reach a hydrogen purity for the use in fuel cell vehicles and in accordance with ISO 14687, the hydrogen purification process consists in most cases at least of a deoxidizer and hydrogen dryer. The deoxidizer removes oxygen by a passive catalytic recombination forming water while the hydrogen dryer uses a temperature (TSA) swing or pressure (PSA) swing adsorption.

In case of alkaline electrolyzers, an upstream scrubber ensures the removal of KOH and particulate (see Figure 3.21). Moreover, nitrogen in higher concentration within the hydrogen product gas can reduce fuel cell power and tamper hydrogen-related control measurements. Therefore, it needs to be ensured that no nitrogen ingress due

to purge operation can occur. In particular, dissolved nitrogen in the feed water can cause higher concentration of nitrogen in the process. As a countermeasure degassing of the feed water within the water treatment and prior to the deionization is required. Provided the nitrogen is properly vented and thereby removed from the process, no dedicated nitrogen post-treatment unit is necessary [LIGEN ET AL. 2020, PESCHEL 2020, BESSARABOV 2018].

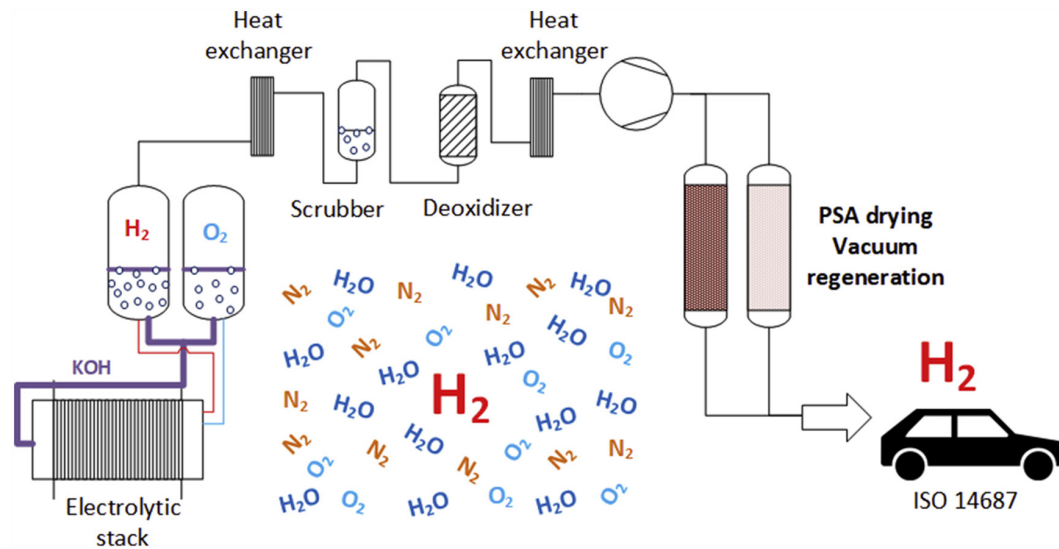


**Figure 3.21:** Typical components and process flow of hydrogen purification for alkaline electrolysis [LIGEN ET AL. 2020]

As depicted in Figure 3.21, the PSA process is the last step of the hydrogen generation and needs to reduce the water content according to thresholds of ISO 14687, so that the hydrogen is eligible for use in numerous applications (e.g. mobility, heating, admixing to gas grid). In order to prevent ice formation affecting the flow and control components of the system, up to 5 ppm of water in the hydrogen gas stream is acceptable. It is also taken into regard that this threshold prevents corrosion of metallic components within high pressure cylinders even at low ambient temperatures.

Current research in this field developed a novel PSA dryer using vacuum with recovery rates of 98.4% [LIGEN ET AL. 2020]. However, hydrogen dryers for water electrolysis usually use the temperature swing technology with a dry gas recycle or a zero loss drier. The adsorbent is in most cases a 3A mole sieve or silica gel leading to water contents below 1 ppm [PESCHEL 2020].

### 3.3 Hydrogen Storage

The low volumetric energy density of gaseous hydrogen poses challenges on the subsequent storage and use of hydrogen. At storage pressures of around 30 bar large vessels are required to store hydrogen in sufficient amounts resulting in extensive use of land. As a result, many hydrogen generation plants use a downstream compressor

to increase the volumetric energy density and thereby reducing the necessary storage volume. However, higher storage pressure requires additional energy for compression and appropriate design of high pressure storage systems. For compressed gaseous hydrogen ( $\text{CH}_2$ ), the theoretical energy consumption can be approximated as an isothermal compression with ideal cooling keeping the gas at constant temperature [SANKIR & SANKIR 2018].

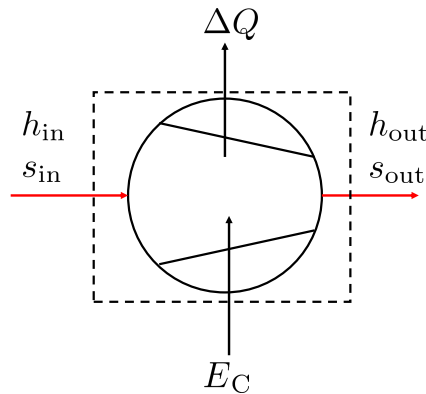


**Figure 3.22:** Thermodynamic system of an isothermal compression

Using the values in Table 3.2 the energy for an ideal isothermal compression from 1 bar at  $20^\circ\text{C}$  to 700 bar can be estimated to  $2.35 \frac{\text{kWh}}{\text{kg}}$ . This is more than 7% of the lower heating value of hydrogen with the tendency to rise due to inefficiencies in compression and the cooling process. According to the first law of thermodynamics the compression energy can be calculated by balancing the energy in- and outputs of the thermodynamic system (see Figure 3.22). This allows the expression of the compression energy  $E_C$  in terms of the constant temperature  $T$  and the changes of entropy  $\Delta s$  and enthalpy  $\Delta h$  [KLELL ET AL. 2018]:

$$E_C = h_{out} - h_{in} + \Delta Q = h_{out} - h_{in} + T\Delta s = h_{out} - h_{in} + T(s_{in} - s_{out}). \quad (3.25)$$

**Table 3.2:** Properties of hydrogen at constant temperature of  $20^\circ\text{C}$  with compression energy  $E_C$  and ratio  $R_{LHV}$  of compression energy to  $LHV_{\text{H}_2}$  based on hydrogen properties from LINSTROM 1997

$p$ in bar	$h$ in $\frac{\text{kJ}}{\text{kg}}$	$s$ in $\frac{\text{kJ}}{\text{kgK}}$	$E_C$ in $\frac{\text{kWh}}{\text{kg}}$	$R_{LHV}$ in %
1	3860.2	53.2	-	-
30	3872.5	39.1	1.15	3.5
100	3905.5	34.1	1.57	4.7
350	4054.8	28.8	2.04	6.1
700	4306.5	25.9	2.35	7.1

There are numerous compression technologies available for the use in hydrogen applications. One of the most established and commercially available types are the mechanical

compressors and in particular reciprocating piston compressors. The movement of the piston from the bottom dead center (BDC) to the top dead center (TDC) while the intake and outtake valves are closed, compresses the hydrogen within the cylinder. Once the outlet valve opens the hydrogen flows to the respective storage tank or is further compressed in a subsequent compression stage. In order to reach sufficient storage pressure multiple reciprocating compression stages are usually needed.

Reciprocating compressors are suitable for lower flow and high pressure output (see Figure 3.23). The possible flow depends on the size of the cylinder and speed of the piston, which is also referred to as the speed of compression. By increasing the cylinder dimensions to reach higher flow rates heavier and bigger components are necessary causing an increase of inertial force. Handling the mechanical stress is then only possible by reducing the speed of compression. Consequently, high compression speeds are only obtained in small cylinder at costs of decreasing flow rates. Main advantages of this mature compression technology is the large adaptability of flow rates and high discharge pressure. On the contrary, side issues with embrittlement, complexity in manufacturing and thermal transfer design pose challenges to this technology [SDANGHI ET AL. 2019, ZÜTTEL 2004].

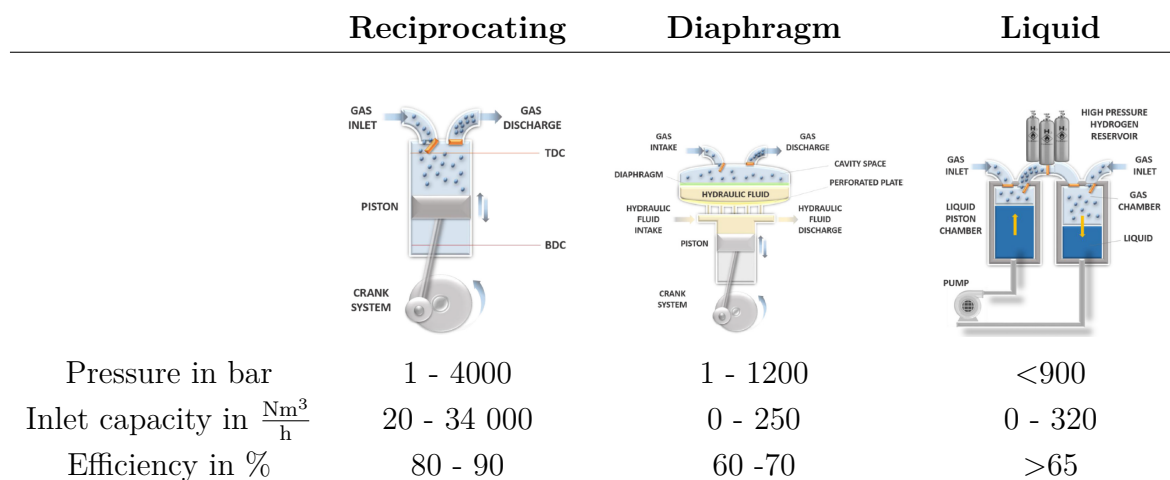


**Figure 3.23:** Overview of mechanical compression technologies for hydrogen according to SDANGHI ET AL. 2019 with typical operation ranges according to PROCESS INDUSTRY PRACTICES (PIP) 2013, SDANGHI ET AL. 2019, LINDE GMBH 2019

Diaphragm compressors avoid the direct contact of the piston with hydrogen by using a diaphragm, which separates a hydraulic fluid with the cavity space where hydrogen is compressed. In order to prevent leakage of hydraulic fluid or hydrogen, the diaphragm material requires high corrosion resistance as well as high durability. As a result, stainless steel, stainless chrome nickel steel, alloys from copper-beryllium and duplex steels are mainly utilized as diaphragm materials. Even though high throughput is possible with this technology, it is appropriate for low flow rates due to the limited volume of the compression chambers. In particular, the high efficiency and compact design are main advantages in micro scale applications. Further research to reduce the size of diaphragm compressors include the replacement of pistons with an electrical



field generated by DC voltage. In this case the movement of the diaphragm is caused by the cyclical varying polarity of the applied voltage. However, challenges regarding diaphragm failure and a complex design of the system remain drawbacks of diaphragm compressor technology [SDANGHI ET AL. 2019].

In general, liquid compressors are positive displacement devices using pressurized liquids to directly compress gas without the necessity of mechanical sliding seals. Efficiencies of more than 83 % are possible due to better heat absorption capabilities, which result from the higher density and heat capacity of the liquid. One of the most common types of liquid compressors in hydrogen refueling stations is the ionic compressor. Its name derives from the use of an ionic liquid, which is a low-melting point salt with beneficial characteristics such as low vapor pressure, excellent tribological behavior and very low solubility of most gases into them. As a result, the ionic compression can be regarded as nearly isothermal due to the significant lower outlet temperatures achieved compared to conventional reciprocating compressors [SDANGHI ET AL. 2019, PREUSTER ET AL. 2017].

It needs to be noted that dynamic compressors such as centrifugal and axial compressors are not available for hydrogen compression so far due to low pressure ratios, complexity and high costs of this system. Potentially, dynamic compressors could be a solution for application with very high flow rates and moderate pressure increases, e.g. for transport via pipelines. However, in this stage of the hydrogen technology evolution the value proposition of dynamic compressors for hydrogen transport has not been found yet. The primary focus is to test and validate the operation of centrifugal compressors with small admixtures of hydrogen in existing pipelines [TIMMERBERG & KALTSCHMITT 2019, PREUSTER ET AL. 2017].

Besides compressing hydrogen there is also the option to liquefy hydrogen in order to reach higher energy density at low temperatures of  $-252\text{ }^{\circ}\text{C}$ . Nevertheless, the main issue of liquid hydrogen ( $\text{LH}_2$ ) is the intensive energy use for liquefaction. Approximately 20 to 30 % of the lower heating value of hydrogen is consumed for this process. In 2010 around 355 t of liquid hydrogen were produced at hydrogen liquefaction plants worldwide with the United States holding the largest share and hydrogen outputs per plant ranging from 0.6 to  $34\frac{\text{t}}{\text{d}}$  [KLELL ET AL. 2018, KRASAE-IN ET AL. 2010]. Due to economic reasons, the tendency for the future is to increase plant sizes and liquid hydrogen outputs [CARDELLA 2018], thus it is unlikely that hydrogen storage in liquid form is a relevant option for smaller scale energy storage systems.

A new hydrogen storage technology approaching the market are liquid organic hydrogen carriers (LOHC). As opposed to the processing of pure hydrogen to achieve higher energy densities, a carrier medium is used to store the hydrogen. The carrier can either be loaded and have an energy-rich state or be unloaded and have a lean energy state. The process of loading and unloading the LOHC is referred to as hydrogenation, respectively dehydrogenation and can be carried out without loss of LOHC (see Figure 3.24)[TEICHMANN ET AL. 2012, MÜLLER 2018b].

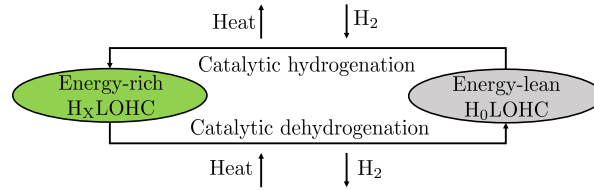


**Figure 3.24:** Process of loading and unloading of the LOHC with hydrogen according to MÜLLER 2018b

Main benefits of the technology are the storage at ambient pressure as well as the easy handling of the LOHC due to its physical properties. Moreover, it is expected that LOHC can be transported via existing mineral-oil based infrastructure with only minor modification needed [TEICHMANN ET AL. 2012, MÜLLER 2018b]. According to MÜLLER 2018b the efficiency of the hydrogenation and dehydrogenation processes can be estimated to 80 % in case a proton exchange membrane fuel cell (PEMFC) is used. It needs to be considered that in this scenario an additional hydrogen burner is needed to provide sufficient heat for the dehydrogenation process. Typical compound pairs of LOHC are shown in Table 3.3 with properties related to the loaded LOHC state.

**Table 3.3:** Overview of compound pairs applicable for LOHC use according to MÜLLER 2018b

$H_0LOHC$	Benzene	Toluene	Naphthalene	$H_0NEC$	$H_0NEC$
$H_xLOHC$	Cyclohexane	MCH	Decalin	$H_{12}NEC$	$H_{12}NEC$
$H_2$ content in wt %	7.2	6.2	7.3	5.8	6.2
$\Delta H_{hydr}$ in $\frac{kJ}{mol}$	-68.7	-70.0	-59.5	-50.5	-65.4
$T_{melt}$ in $^{\circ}C$	6	-93	81	71	-34
$T_{boil}$ in $^{\circ}C$	80	110	218	270	371

A similar concept is used by metal hydrides to store hydrogen. Metal hydrides use solid materials such as  $LaNi_5$ ,  $TiCr_{1.6}Mn_{0.2}$  or hydro-alloy C5 graphite to bond hydrogen within the grid structure of the materials. The efficiency of storage depends on the thermophysical properties of the material and recent research has shown that metal hydrides are a feasible option of storing hydrogen for microgrid applications with overall energy efficiencies of 95.5 % [KUMAR ET AL. 2020].

However, it is a new technology still in intensive research with currently commercial availability only for very small storage capacities. Main advantages of metal hydrides besides the high storage capacity is the possibility to compress hydrogen using only thermal energy, thus eliminating the need for moving parts as they are necessary in conventional hydrogen compressors [ERIKSEN 2018].

### 3.4 Hydrogen Reconversion

In general, the stored hydrogen can be used for numerous applications, such as ammonia synthesis, production of synfuels or even as fuel for internal combustion engines. Additional storage energy can be required if hydrogen needs to be stored in an energy carrier molecule such as LOHC or simply in compressed or liquefied state. The desired way of conversion with regards to zero emissions is usually the reaction in a fuel cell. A fuel cell is an energy converter which performs the inverse chemical reaction of electrolysis (see Subsection 3.2.2) and consequently enables hydrogen to react with oxygen from air, only producing electrical current and water as by-product [KURZWEIL 2016]. With the production of electrical current the hydrogen loop (see Figure 3.25) is closed and assuming that green hydrogen was produced no carbon emissions occurred along the way.

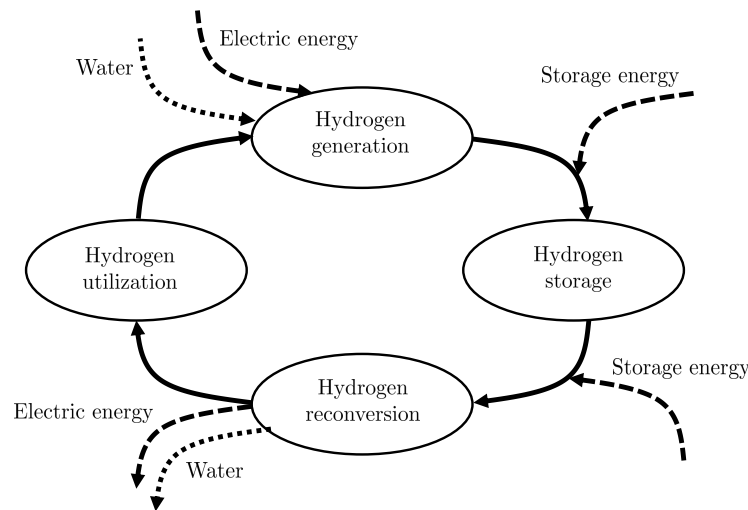


**Figure 3.25:** Carbon-free hydrogen energy loop

The maximum output of electrical energy  $E_{el}$  corresponds to the maximum amount of external work available  $\Delta G$ , neglecting any work done by changes in pressure or volume. By including the Faraday constant  $F$  the electrical energy can be calculated by:

$$E_{el} = -\frac{\Delta G}{2F}. \quad (3.26)$$

For operating temperatures of fuel cells below 100 °C, this correlation leads to an ideal voltage of 1.2 V. Due to crossover of the reactants the open circuit voltage results to 1 V and activation, ohmic and concentration losses decrease the operating voltage even further in the range of 0.8 to 1.0 V. Activation losses are caused by the nature of the chemical reaction and depend on the catalyst material, microstructure of the MEA, reactant activities and the current density. Ohmic losses are caused by the electrical resistance within the system and concentration losses occur when a drop in concentration of reactants at the surface of the electrodes is observed. Figure 3.26 shows

the zones of voltage loss for an exemplary PEMFC. The polarization curve characterizes the relation between the voltage and the current density [LI ET AL. 2019].

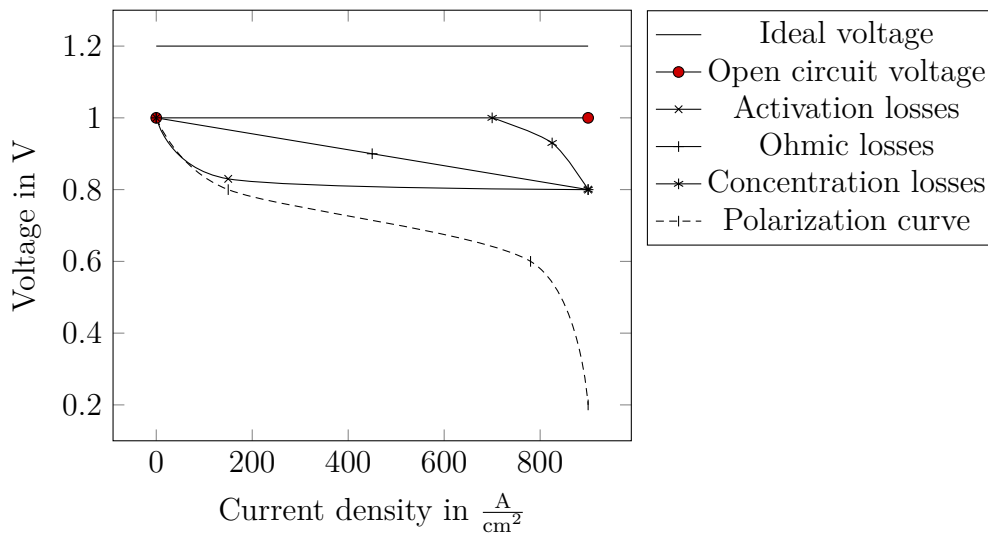


**Figure 3.26:** Voltage losses and polarization curve of an PEMFC according to LI ET AL. 2019

As a result, regular operating voltages of PEMFC are between 0.6 and 0.7 V. The detailed chemical reaction of electrolysis depends on the electrolyte used, but always results in the overall reaction [DAUD ET AL. 2017]:



In almost the same manner as for electrolysis, the different fuel cell technologies are categorized by the electrolyte used in the process and can be divided in high-, medium- and low-temperature fuel cells [KURZWEIL 2016]:

- Low-temperature fuel cells
  - Alkaline fuel cell (AFC)
  - Proton exchange membrane fuel cell (PEMFC)
  - Direct methanol fuel cell (DMFC)
- Medium-temperature fuel cell
  - Phosphoric acid fuel cell (PAFC)
- High-temperature fuel cells
  - Molten carbonate fuel cell (MCFC)
  - Solid oxide fuel cell (SOFC)

The highest share of all fuel cell types with 589.1 MW of the total 803.1 MW in the year 2018 belongs to the PEMFCs. In particular, the use of PEMFC in mobile applications such as cars, trucks, trains and ships has increased its importance in the market. Due to the high load response flexibility compared to other fuel cell technologies, PEMFC is the

predominate solution for mobility application with hydrogen. But also for stationary power supply or even for emergency backup power PEMFC are utilized [E4TECH 2018]. Challenges for PEMFC remain the high costs of the material caused by acidic process conditions and the noble catalysts needed. Half of the costs for a 80 kW fuel cell unit are traced back to the stack and around half of these costs are related to the catalysts. Current research focuses on finding substitution materials for noble catalysts, thus leading to cost reduction while keeping constant fuel cell performance [FRANK BRUIJN & JANSSEN 2017].

In Figure 3.27 a state-of-the-art PEMFC schematic with the corresponding process is depicted. Hydrogen is entering on the anode side and is split in positive hydrogen ions and negative electrons (see Equation 3.28) while emitting heat. The hydrogen ions pass through the membrane and react on the cathode side with oxygen and electrons to water (see Equation 3.29). The free electrons induce an electrical current between the electrodes, thus providing power to an electrical consumer (e.g. electrical motor). Unused hydrogen is recirculated on the anode side of the cell [YUAN ET AL. 2020].

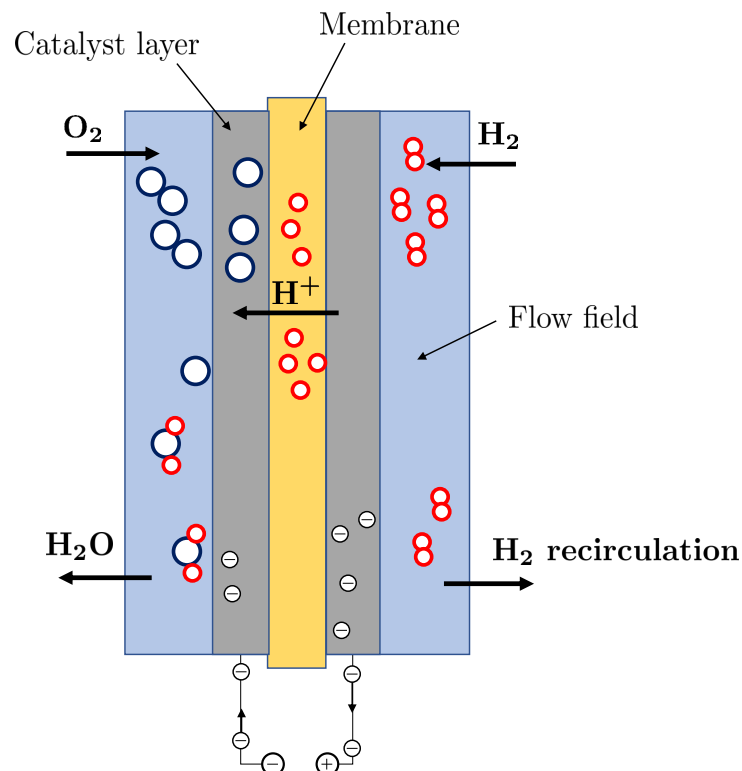


**Figure 3.27:** Schematic of PEMFC according to YUAN ET AL. 2020

PEMFC are also used in off-grid energy systems and posing an environmental-friendly alternative of power supply. Higher efficiency, quiet operation, high load flexibility, simple maintenance and operation at low temperature without danger of causing

fire are major advantages compared to conventional generators (e.g. diesel generators) [BEZMALINOVIĆ ET AL. 2013]. As a result, PEMFC are mostly used for off-grid power provision with available power ratings of less than 1 kW. However, if multiple PEMFC units are combined together, the energy demand of remote villages can be covered in a clean and safe manner [ESMAP 2020].

Very similar to the setup of the PEMFC is the DMFC. It uses also a proton exchange membrane and can be regarded as an exception in the naming convention for fuel cells due to the name derivation based on the fuel used. The mixture of water and methanol eliminates the necessity for gas moisturizing, air cooling and reformation. However, the methanol-water mixture needs to be dosed precisely by a respective pump. With efficiencies of 20 to 30 % and challenges with gas crossover, methanol oxidation and low active anode catalysts the development and wide commercial availability has damped [KURZWEIL 2016, SLADE ET AL. 2018].

Major drawbacks due to corrosion issues and required clean gas operation causing blockage hazard by potassium carbonate have also limited AFC for hydrogen application. Although AFC has the highest efficiency of all fuel cell technologies with 60 to 70 % and is able to use cost-effective catalysts, it had a limited field of application so far. However, the up-scaling of the hydrogen economy is in progress and the demand for large fuel cell system will rise, potentially placing AFC in a more beneficial position due to lower system costs. Research in this field involves also the development of anion exchange membranes for alkaline fuel cells evolving the AFC to a AEMFC. By utilizing this type of membrane and removing the liquid electrolyte, the hydroxide ions have enhanced oxygen reduction kinetics and increased CO<sub>2</sub> tolerance [KURZWEIL 2016, SUN ET AL. 2017].

As the single type of a medium-temperature fuel cell, the PAFC is to mention. It operates at temperatures of 180 °C, utilizes a phosphoric acid as a proton conductor and tolerates 1 to 3 % CO and H<sub>2</sub>S in the fuel, making it possible to process hydrogen-rich fossil fuels. The higher operating temperatures of a PAFC are a compromise between electrolyte conductivity and cell degradation. Furthermore, they are mostly used for stationary applications with power outputs of several 100 kW and first pilot plants in the MW range are already installed. Even though the technology is proven and has high reliability, cost challenges need to be overcome for broad commercialization [KURZWEIL 2016, KANURI & MOTUPALLY 2012].

As opposed to the low temperature operation of the AFC, PEMFC, DMFC and PAFC, high-temperature fuel cells work with carbonate or oxide ions instead of hydroxide ions and protons. There are two types of fuel cells relevant for high-temperature operation between 600 to 800 °C which use molten carbonate (MCFC) or solid oxide (SOFC) as electrolytes. In general, the higher operating temperature enhances electrochemical reactions at the electrodes, thus increasing the efficiency while working with inexpensive materials as catalysts. MCFC as well as SOFC are mainly used for stationary power generation profiting from heat integration potential, which can lead to higher overall efficiencies of the process. Although the technology struggles with low power densities

and stability in the corrosive environment, numerous field tests have proven the feasibility for stationary applications. In a MCFC hydrogen or reformat from methane reaches the anode side of the fuel cell bonding with carbonate ions and producing  $\text{CO}_2$  and free electrons. The electrons initiate an electric current while on the cathode side oxygen, carbon dioxide and electrons form carbonate ions, which are transported through the molten carbonate salt electrolyte to the anode. One likely reason why the MCFC has not commercialized at large scale is the initial intention to only use it as an interim solution in order to be able to reform hydrogen from natural gas and at the same time push the needle on decarbonization. However, with climate goals becoming more ambitious, the necessity for  $\text{CO}_2$  to run a clean process seemed contradicting. As a result, the development of MCFC slowed down in the beginning of the last decade from worldwide 70.5 MW installed in 2014 to only 25.2 MW in 2018 [KURZWEIL 2016, HEMMES 2021, KULKARNI & GIDDEY 2012, LEE 2017, MCPHAIL ET AL. 2011].

Instead the SOFC technology was witnessed to gain momentum and increased the installed capacity from 38.2 to 91 MW per year, being currently the dominant technology in the field of high-temperature fuel cells. SOFCs have low pollution characteristics, high efficiencies of approximately 60 % and an expanded spectrum of fuels, that can be used. The electric current is generated by free electrons resulting from hydrogen reacting with oxygen ions and thereby creating water and heat. On the cathode side oxygen is reduced with electrons to oxygen ions, which pass through the metal oxide electrolyte to maintain the reaction.

Unlike the low-temperature fuel cells, the SOFC and MCFC can reform light hydrocarbons by a methane steam reforming and water-gas shift reaction at the anode. However, the targets are set to use hydrogen as fuel in order to ensure a clean energy production and additionally utilize the produced heat in the best way. In particular, the SOFC is promising in applications for combined heat and power as well as for large-scale power generation. Nevertheless, material issues caused by the high operating temperature, catalyst poisoning and interface problems due to deviated thermal expansion characteristics of the components installed remain challenges for the SOFC and are subject to industrial and academic research [E4TECH 2018, HEMMES 2021, HUSSAIN & YANGPING 2020, ATKINSON ET AL. 2012, KEUSCHNIGG 2016, ZAKARIA ET AL. 2019].

## 3.5 Battery Storage and Electrical Components

Instead of converting electrical energy to hydrogen, there is also the possibility to store it directly in a battery. This storage option excludes components such as fuel cells and electrolyzers, thus representing a compact and more efficient path for energy storage. However, batteries are also often used in combination with fuel cells due to their fast response time and as backup option for power supply. For mobile applications such as cars, trains and ships, batteries are installed to cover peak power demands and relieve load on the fuel cell [FLETCHER & EBRAHIMI 2020]. Batteries convert chemical energy

into electricity, which is the main purpose of disposable primary batteries. On the other hand, secondary batteries or accumulators use reversible electrochemical reactions to recharge the battery. This is achieved by applying voltage in the opposite direction of the discharge. By connecting electrochemical cells in parallel the residing current can be increased while the voltage remains constant. In case the cells are connected in series the voltage rises while the current remains constant [SUNDÉN 2019].

Batteries and fuel cells are types of galvanic cells, which are electrochemical devices producing electricity in spontaneous reactions. They are characterized by connected electrodes in contact with an electrolyte and a connection to an electrical consumer. Depending on the fuel cell type, hydrogen or light hydrocarbons can be processed and generate electricity as long as fuel from an external source is available. On the other side, batteries have a limited and predetermined amount of energy they can deliver. However, instead of only functioning as an energy converter like a fuel cell, the battery can store energy directly without depending on external connections or fuel supply. The driving mechanism of charging and discharging of an accumulator is the reduction–oxidation reaction, which is the overall reaction consisting of an oxidation at the anode and reduction reaction at the cathode.

In Figure 3.28 a basic cross section of a battery is depicted, where the electrodes and the separator are immersed in electrolyte. The separator prevents a short-circuit while the electrolyte functions as carrier for electrical charge [PETROVIC 2020].

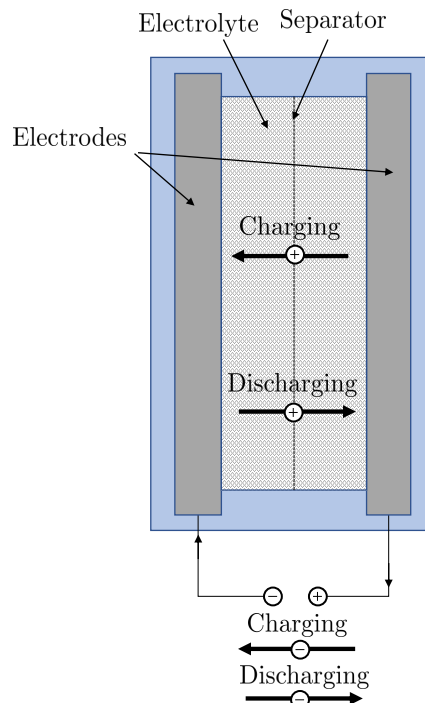


**Figure 3.28:** Basic cross-section of a battery cell according to PETROVIC 2020

During discharge electrons are released by an oxidation reaction and move to the cathode by passing through the load and thereby powering a device. The ions from the oxidation are transported via electrolyte to the cathode. The reverse reaction takes place during



charging, where the load is replaced by a charger or power supply. Although the polarity of the electrodes remains the same, the power supply overcomes the potential difference and enables the transport of electrons from the less negative electrode (right side in Figure 3.28) to the more negative electrode (left side in Figure 3.28).

Depending on the reduction potential of the electrode material different theoretical cell voltages are obtained. Under standard conditions the cell voltage  $E_{Cell,th}$  is the difference between the reduction potential of the cathode  $E_{Cathode}$  and the anode  $E_{Anode}$  as shown in Equation (3.30) [PETROVIC 2020].

$$E_{Cell,th} = E_{Cathode} - E_{Anode} \quad (3.30)$$

However, in reality effects of concentration in the solution, effective pressure and temperature influence the cell voltage. The Nernst equation (see Equation (3.31)) takes these aspects into account and puts the cell voltage  $E_{Cell}$  with the reaction quotient  $Q$  for battery reaction into correlation. The reaction quotient  $Q$  is the ratio of concentration of products over concentration of reactants. By using a factor consisting of the universal gas constant  $R$ , the absolute temperature  $T_{abs}$ , the Faraday constant  $F$  and the number of electrons  $z$  involved, the reaction quotient is converted to voltage units [PETROVIC 2020].

$$E_{Cell} = E_{Cell,th} - \frac{RT_{abs}}{zF} \ln Q \quad (3.31)$$

By applying Faraday's first law of electrolysis, which states that the mass of a substance consumed in a battery is directly proportional to the quantity of electricity involved, the following equation is used to calculate the theoretical specific battery capacity  $c_{th}$ :

$$c_{th} = \frac{Fz}{M} \cdot \quad (3.32)$$

The Faraday constant  $F$  represents the electric charge and equals to 26,855 mA h. Considering the molecular mass  $M$  and the number of electrons in the reaction  $z$  the relationship between the amount of battery active mass and the quantity of electricity is established resulting in the theoretical specific battery capacity  $c_{th}$ . Different elements and their specific battery capacities can be compared now as shown for selected elements in Table 3.4 [PETROVIC 2020].

By multiplying the battery voltage  $U_{Bat}$  with the specific capacity  $c_{th}$  the specific energy  $e$  of the battery is calculated:

$$e = c_{th} \cdot U_{bat} \cdot \quad (3.33)$$

Besides the active mass of a battery, the total weight of a battery includes other additional components. Typically current collectors, electrolytes, separators, terminal

**Table 3.4:** Overview of electrochemical characteristics for selected elements according to BRATSCH 1989, PETROVIC 2020

Element	Molar mass in $\frac{\text{g}}{\text{mol}}$	Standard reduction potential in V	Number of electrons	Specific capacity $c_{th}$ in $\frac{\text{Ah}}{\text{g}}$
Pb	207	- 0.35	2	0.26
Cd	112	- 0.4	2	0.48
Zn	65	- 0.76	2	0.82
Li	7	- 3.05	1	3.86

seals and a housing are installed, which increase the volume and weight of the battery without contributing to the stored energy. The ratio of specific energy and overall mass of the battery is referred to as practical specific energy.

Moreover, electrochemical losses in the battery due to slow reaction activation, incomplete utilization of active materials, ohmic and mass transport losses reduce the stored energy output. As the overview of different battery systems in Table 3.5 depicts, only 11 to 27 % of the theoretical specific energy of the active materials can be used practically for battery storage [KURZWEIL & DIETLMEIER 2018, PETROVIC 2020].

**Table 3.5:** Overview of theoretical and practical specific energy according to PETROVIC 2020

System	Theoretical specific energy in $\frac{\text{Wh}}{\text{kg}}$	Practical specific energy in $\frac{\text{Wh}}{\text{kg}}$	Fraction in %
LAB	167	33	20
NiCd	240	45	19
NiMH	300	79	26
NiZn	320	80	25
ZnBr	435	90	21
Li	450	120	27
NaS	795	90	11

It can be recognized from Table 3.5 that the lithium battery system has by far the highest practical specific energy, which is the reason why lithium-ion batteries are the preferred option for energy storage in BEV. Lithium-ion batteries rely on the transport of positive lithium ions ( $\text{Li}^+$ ) and their intercalation on both electrodes, therefore they remain  $\text{Li}^+$  ions throughout the process and are not converted to any other compound. Depending on the structure of the electrodes and the given cell chemistry lithium-ion batteries can vary strongly in performance. In general, they are distinguished in batteries for high power or high energy application with different requirements for charging and discharging.

In order to guarantee a safe operation of the cell, the main parameters such as current, voltage and temperature are monitored and a BMS is used to protect and manage the battery. However, a main drawback of batteries is the limited cell life, which

is continuously reduced by two degradation processes. One is the degradation by charging and discharging of the cell while in use, the other is the calendar life, which is a degradation over longer time periods but independent of the battery utilization. There are four main parameters affecting the process of degradation and depending on the cycle number the intensity varies (see Figure 3.29) [ANDREA 2020, STERNER & STADLER 2017].

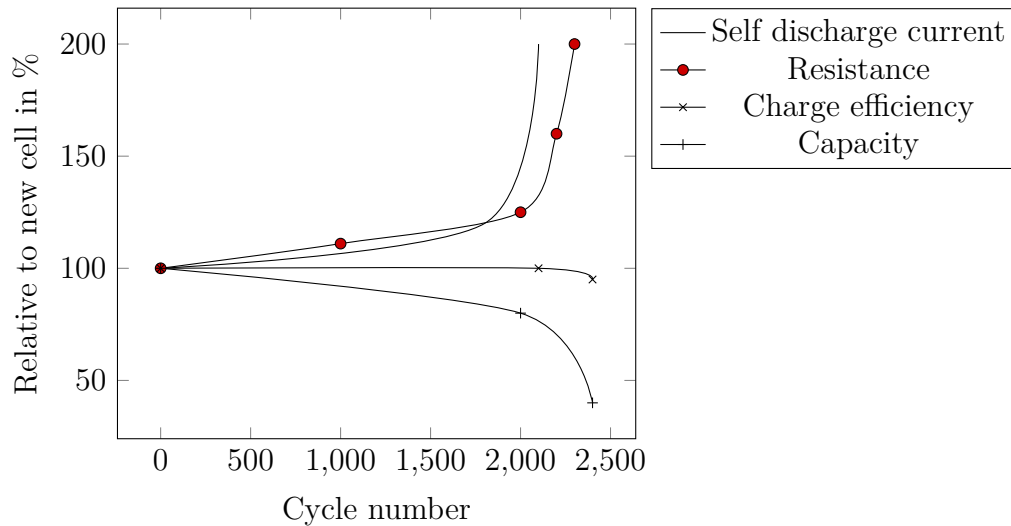


**Figure 3.29:** Typical cycle life of a lithium-ion battery with parameters affecting degradation according to ANDREA 2020

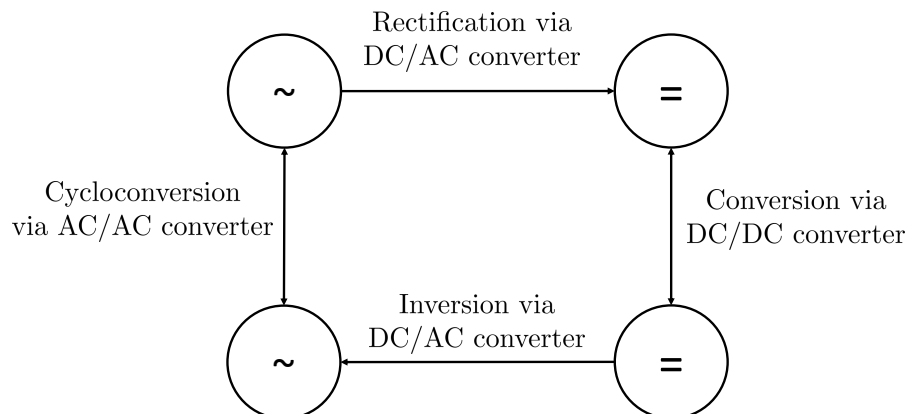
Lithium-ion batteries are used in numerous applications such as mobility, stationary or residential power supply. As the requirements differ in the respective fields, so do the costs. In 2017 costs for energy-designed systems were  $500 \frac{\text{€}}{\text{kWh}}$ , for power-designed systems  $800 \frac{\text{€}}{\text{kWh}}$  and  $750 \frac{\text{€}}{\text{kWh}}$  for residential batteries used for example in combination with a PVPP. It is expected that by 2040 the costs for stationary storage systems will decrease and be in the range of  $165$  to  $240 \frac{\text{€}}{\text{kWh}}$  for energy-designed systems,  $280$  to  $410 \frac{\text{€}}{\text{kWh}}$  for power-designed systems and  $250$  to  $365 \frac{\text{€}}{\text{kWh}}$  for households [CENTRE. 2018]. The largest fraction of these costs are caused by the material for the anode and especially the cathode. As a result, a lot of effort has been put in the improvement of electrode materials leading to a variety of anode and cathode material combinations (see Table 3.6) [IRENA 2017, MÜLLER 2018a].

Based on the specific use case and application, the battery technology is chosen. For electric vehicles the NCA/C and NMC/C are utilized due to their high energy and power density. Challenges with reduced lifetime and lower safety performance are accepted drawbacks. On the other side, LFP/LTO or LFP/C cells have excellent safety properties and a long life cycle at low costs. As a result, they are predestined for stationary applications. Batteries with LMO/C represent a compromise with high power but low capacity and a relatively safe design. Common applications for this technology are power tools, medical devices or power trains [MÜLLER 2018a, PETROVIC 2020].

**Table 3.6:** Overview of common chemistry for lithium-ion batteries according to MÜLLER 2018a

Cathode/Anode	Safety	Power density	Energy density	Cell costs	Lifetime
LFP/LTO	++	+	o	-	++
NMC/C	+	+	++	+	+
LFP/C	++	+	o	+	++
LMO/C	+	+	+	+	o
NCA/C	o	++	++	o	++

Regardless of the battery technology, additional components are necessary to operate an energy storage system. In particular, power electronics are required to ensure proper voltages and currents for the electrical loads and sources. As shown in Figure 3.30 direct current (DC) can be transformed to alternating current (AC) with a DC/AC-converter and vice versa with an AC/DC-converter. Also, DC can be changed from one voltage level and polarity to different ones by a DC/DC-converter. Respectively, alternating current can be changed to different voltages and frequencies using an AC/AC-converter.

**Figure 3.30:** Energy conversion using power electronics according to MARENBAACH ET AL. 2020

Key element of these electronic devices are switching converters, which consist of a power input, a control input port as well as a power output port (see Figure 3.31).

By combining devices for electrical circuit design such as switches, resistors, capacitors, inductors and semiconductor devices, the desired electrical properties at the output can be reached. In general, any input voltage can be converted into the desired output voltage using a converter consisting of switching devices embedded within a network of reactive elements [MARENBAACH ET AL. 2020, ERICKSON & MAKSIMOVIĆ 2020]. In a hydrogen energy system as depicted in Figure 2.1 many loads with different electrical input specifications demand adequate power. Therefore, sizes and amounts of the power electronics equipment need to be considered in the overall design of selfHY®.

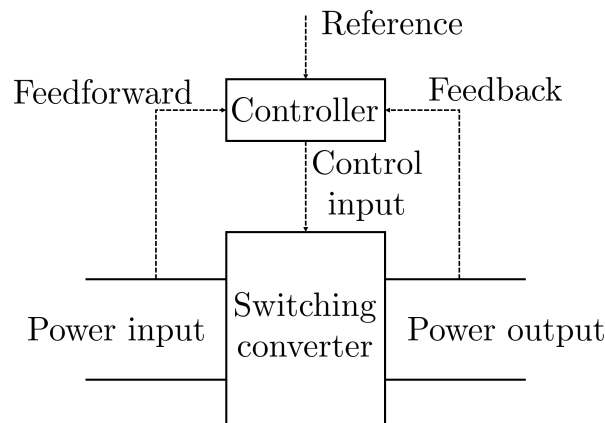


**Figure 3.31:** Power processing block with controller according to ERICKSON & MAKSIMOVIĆ 2020

### 3.6 Self-Sufficient Energy Systems with Hydrogen

The idea of self-sufficient energy systems is not new and was subject to research in the past. ULLEBERG 1998 developed simulation models for a stand-alone hydrogen energy system using TRNSYS [UNIVERSITY OF WISCONSIN MADISON 1975] concluding sufficient accuracy for system simulation of short and long-term operation. The model was validated by respective data from a demonstration plant at the research center in Jülich, Germany. Moreover, DINCER 2002 analyzed the technical, environmental and exergetic aspects of hydrogen energy systems with a focus on conventional hydrogen generation paths and for large scale. At high costs of 2.4 to 3.6  $\frac{\$}{\text{kg}}$  for hydrogen production with fossil-source electricity, electrolysis was only viable in niche markets.

Since then the technologies and components used in hydrogen energy systems improved and became commercially available. The relevance of green hydrogen production via electrolysis increased with the expansion of renewable energy sources and the rising awareness of climate protection, which can be witnessed currently. Over the last two decades major milestones have been reached to pave the way for the commercialization of hydrogen energy systems by reducing costs significantly. Today we even reached the point where hydrogen could be more economic than diesel for microgrids [CHROMETZKA ET AL. 2020]. As a result, first commercially available products at small scale using hydrogen in remote energy systems were introduced to the market, not all of which are still available.

Sunfire Fuel Cells GmbH is specialized on high-temperature fuel cells with focus on the solid oxide technologies. For remote power generation, the Sunfire-Remote 900 with 850 W average electrical output has been designed and promises reliable power and heat generation by utilizing low-cost propane. A smaller version, the Sunfire-Remote 400 with average electrical output of 350 W, is also available and uses propane or natural gas as fuel. An aspect to consider is that the process generates minimum emissions and therefore it cannot be considered a zero emission technology [SUNFIRE FUEL CELLS

GMBH 2021]. Moreover, the power generation via fuel cell represents only one part of a complete hydrogen energy system and requires further components as well as their integration.

Toshiba Energy Systems & Solutions Corporation (TESSC) developed the hydrogen energy system H2One™ aiming to install it off-grid on an Indonesian island. Using a combination of long-term hydrogen storage and short-term battery storage, the system is intended to supply stable and low cost energy. Renewable energy powers the electrolyzer and other electrical consumers of the system. Heat from the hydrogen generation process is used to bring warm water to villages. In summary, H2One™ is a renewable hydrogen energy system providing clean energy for remote locations. Current specifications of the H2One™ container model define small scale fuel cell power outputs of 3.5 kW with 200 Nm<sup>3</sup> hydrogen storage, which leads to the conclusion that the system is intended for long-term energy supply at relatively low power output rates [TOSHIBA ENERGY SYSTEMS & SOLUTIONS CORPORATION 2021].

Similar to H2One™ the Belgium company Tiger Power developed together with VITO/EnergyVille a small scale hydrogen energy system to provide energy for small villages in Uganda. By mounting a special mechanical structure on the container, which carries the PV-modules, a compact system has been achieved. The containerized solution is capable of producing 11 to 27 kWh of green energy per day and store up to 300 kWh of hydrogen, which can be used in times of energy shortage [VITO NV 2018].

Another system with higher power output of 30 kW has been presented by the french company Powidian. The MobHyl Power® M30 uses an external hydrogen supply, preferably in 200 bar gas bottles, to provide energy for 3.5 hours at rated power. An additional 20 kWh LFP battery allows flexible operation and short-term energy storage [POWIDIAN 2019]. In Table 3.7 the mentioned hydrogen energy systems are summarized.

**Table 3.7:** Overview of available solutions for self-sufficient hydrogen energy systems according to SUNFIRE FUEL CELLS GMBH 2021, TOSHIBA ENERGY SYSTEMS & SOLUTIONS CORPORATION 2021, VITO NV 2018, POWIDIAN 2019

	Sunfire	TESSC	Tiger Power	Powidian
Power in kW	0.85	3.5	3	30
H <sub>2</sub> storage in kWh	N/A	≈ 600	300	N/A
Battery in kWh	N/A	44	undisclosed	20
Application	Backup power	Electrification	Electrification	Backup power

Based on the elaboration of available hydrogen energy systems and the corresponding technologies as described in Chapter 3, an improved concept for a self-sufficient energy system with hydrogen as energy carrier is developed in this work. Moreover, a water treatment unit for potable water installed within the hydrogen energy system is foreseen. Starting with the definition of requirements of selfHY®, an evaluation of the technologies

is performed resulting in the optimized configuration for the use case. For the hydrogen energy system as well as the energy inputs and outputs of the plant, a model is created in MATLAB/Simulink<sup>®</sup> allowing to compare different sizing scenarios in order to agree on the most favorable concept. At last, the suitability of selfHY<sup>®</sup> for a specific location as well as the economic feasibility are assessed.





# 4 Specification of selfHY<sup>®</sup>

In this chapter, the methodology of the concept development and the product requirements of selfHY<sup>®</sup> are elaborated, concluding a decision on technology for each subsystem of selfHY<sup>®</sup>. For a new concept development of an off-grid energy system with hydrogen, the Munich Procedural Model (MPM) [BOBBE ET AL. 2016] is used to structure the methodology and ensure a holistic view on the product design. The MPM as depicted in Figure 4.1 is based on established procedural models (e.g. V-model according to VDI/VDE 2206) and influenced by numerous research projects and industrial applications. With the intention to integrate beneficial aspects and eliminate weaknesses of different approaches, this methodology is commonly used for concept designs of products in an early stage as it is the case in this work [LINDEMANN 2007].

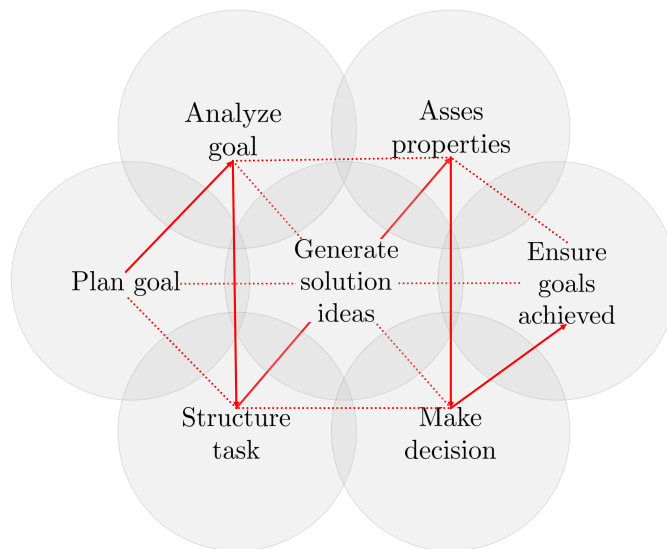


**Figure 4.1:** Munich Procedural Model according to LINDEMANN 2007 applied for development of selfHY<sup>®</sup>

In general, the MPM can be divided in seven different steps and has a standard path which can deviate according to the approach and circumstances of the specific project. The first step of planning a goal of the project is covered in Chapter 2 describing the goal to develop a self-sufficient energy system with hydrogen for rural areas. Following this definition, the particular goal is analyzed and the overall system is divided into smaller subsystems in order to reduce the complexity. Moreover, potential solution ideas are generated in Chapter 3 by identifying and describing current state of the art technology for each subsystem. The last step of the MPM is to ensure the goals are achieved. This requires a final check of the decisions made in the previous step in order to mitigate potential negative consequences in the development process. As previously mentioned, the focus in this chapter lies on assessing and evaluating general and specific requirements of selfHY<sup>®</sup> in order to conclude the optimal choice of technology for

each subsystem. In Figure 4.1 the approach of the concept development for selfHY® according to the MPM is visualized as described previously using the standard path.

## 4.1 Requirement Analysis

In the interest of finding the best configuration of technologies for selfHY®, each subsystem is rated depending on different criteria. Moreover, each criteria is weighed according to its importance for the specific subsystem, but also considering the effects on the overall system. For this reason, the use of the weighted sum method (WSM) is applied in order to compare the different technology options described in Chapter 3. The weighted sum method combines a performance value  $a_{ij}$  of different alternatives  $i$  in terms of the  $j^{\text{th}}$  criterion with the relative weight of importance of the criterion  $w_j$ . As a result the WSM score  $A_{WSM}$  is calculated as shown in Equation (4.1) and the alternative with the maximum value is considered the best for the maximization case [TRIANANTAPHYLLOU 2000].

$$A_{WSM} = \max_i \sum_{j=1}^n a_{ij} w_j \quad \text{for } i = 1, 2, 3, \dots, m \quad \text{and } j = 1, 2, 3, \dots, n \quad (4.1)$$

Before performing the WSM for each subsystem, the general requirements of selfHY® need to be formulated for consideration in the WSM.

### 4.1.1 System

The intended use of selfHY® is for reliable and emission-free electrification of remote regions with limited infrastructure. The general idea is to develop a product with proven design and fully integrated components within a containerized system, which is convenient for transport in rural areas. For this reason, a standardized 20 foot container ( $L = 6.058$  m,  $H = 2.591$  m,  $W = 2.438$  m) according to ISO 668 is used as platform for integration of the system components. With further investigation, it might occur that the needed installed power of the renewable energy source exceeds the possibilities of integration within a 20 foot container or is technically not feasible. This would lead to a spatial split of the renewable energy source (see Figure 2.1) and the other subsystems of selfHY®. Nevertheless, the renewable energy source is still regarded as part of selfHY® in this case and a conducive solution for the installation and connection of the renewable energy source needs to be found, preferably also within another 20 foot container. Furthermore, the installation on site needs to be as simple as possible due to expected demanding conditions on-site and limited options for civil works. Connected to this is also the requirement for an automated start-up procedure and low maintenance intervals. The product lifetime of selfHY® shall be at least twenty five years in accordance to industry standards.

For better overview and to enable a clear methodological approach, the general system requirements described in the prior paragraph are summarized to one single criterion “system” for the WSM. This criterion rates the suitability of the technology alternatives collectively with regards to the following aspects:

- Integration potential in standardized 20 foot container
- Installation effort
- Start-up effort
- System complexity
- Product lifetime

Based on the state of the art mapped out in Chapter 3, the weighting of the criteria and rating of the technology alternatives are conducted for each subsystem. The criteria are weighted with a factor  $w_j$  from 0 to 1 and the rating of the technology is set to a value from 0 to 10 for the respective criterion using the maximization case.

### 4.1.2 Renewable Energy

As described in Section 3.1, there are four main renewable energy technologies, which are considered for selfHY<sup>®</sup>. The WSM is performed using the criteria for the overall system described in Subsection 4.1.1, the technology readiness level (TRL), the area required for installation and the expected costs. The TRL categorizes a product or system according to its technology maturity and is based on a scale from 1 to 9 with 9 being the most mature technology [NEILL & HASHEMI 2018]. A more detailed overview of the single levels is shown in Table 4.1.

**Table 4.1:** Scale of technology readiness levels (TRL) according to FASTERHOLDT ET AL. 2018

TRL	Description
9	System proven in operational environment
8	System complete and qualified
7	Integrated pilot system demonstrated
6	Prototype verified
5	Laboratory testing of integrated system
4	Laboratory testing of prototype component or process
3	Critical function, proof of concept established
2	Technology concept and/or application formulated
1	Basic principles are observed and reported

The criterion with the highest importance for the subsystem of the renewable energy source is the TRL<sup>2</sup> due to the requirement of a proven design and availability on the market. Costs of the technology play a slightly less important role compared to the TRL, but remain crucial due to the main goal of providing affordable energy for remote areas. In most cases these remote locations will provide sufficient area for installation resulting in the lowest priority for the choice of the renewable energy source. At last, the system criterion described in Subsection 4.1.1 is considered in a moderate way due to the necessity of integration and high product lifetime of the renewable energy source. The weigh factors  $w_j$  for each criterion are summarized in Table 4.2.

For the renewable energy source the integration within selfHY<sup>®</sup> is one of the main challenges since it is expected to be the subsystem with the largest footprint. This poses special difficulties on facile, but compact transport of the renewable energy unit. Comparing the renewable energy technologies elaborated in Section 3.1, PV is considered the best solution with regards to the overall system. PV modules can be placed on top of a container as well as folded inside for transport and expanded with a mechanical structure on-site. Furthermore, PV modules are established for small-scale power applications and proven technology, especially for off-grid locations. In terms of the installation area, PV and CSP account for the lowest area per installed power [ZALK & BEHRENS 2018]. However, the CSP is commercially only used in large-scale applications and is difficult to integrate for small off-grid systems due to necessity of an additional fluid cycle with generator as described in 3.1.2. Another positive aspect of PV are the low costs compared to other renewable energy sources, especially in areas with high solar irradiation. The main obstacles for hydropower and wind energy are the higher costs and compared to PV the more difficult container integration, which causes increased installation effort on-site. The results of the WSM for the subsystem renewable energy source are summarized in Table 4.2.

**Table 4.2:** Results of WSM for subsystem renewable energy source

	System	TRL	Footprint	Cost	$A_{WSM,RE}$
$w_j$	0.2	0.4	0.1	0.3	
PV	10	10	6	10	9.6
CSP	5	7	6	4	5.6
Wind	6	10	5	8	8.1
Hydropower	8	8	3	6	6.9

### 4.1.3 Hydrogen Generation

One of the key components of selfHY<sup>®</sup> is the hydrogen generation system. Hydrogen generation includes usually a unit for water purification, electrolysis and hydrogen

<sup>2</sup> Although the scale of the TRL ranges from 1 to 9 as shown in Table 4.1, for the purpose of a more consistent comparison of the weigh factors  $w_j$ , the highest TRL is quantified with 10 and the lowest with 1.

purification. While the water and hydrogen purification units have marginal differences along the technologies, the distinguishing feature is the electrolysis technology. As described in Section 3.2, each technology has its pros and cons and is utilized depending on the specific circumstances. The aim of this subsection is to identify the most appropriate technology for the off-grid use in selfHY<sup>®</sup>. For this reason, the suitability of the technologies with regards to the system as described in Subsection 4.1.1, the TRL (see Figure 4.1), the footprint, the cost, the possible pressure difference and the flexibility of operation are valued. The choice for the weighing factor  $w_j$  is shown in Table 4.3 and stresses the importance of a simple system with high integration potential in a container by setting the highest priority on the system criterion. Moreover, the aspect of integrating a remineralization unit for potable water treatment is considered in the system criterion due to the benefit of demineralized water availability for the electrolysis anyway. For a compact design and integration in a container, the footprint is also crucial and accounts for the same priority as the TRL. Furthermore, the criteria pressure is used to rate the possibility of higher outlet pressures downstream the electrolyzer. The higher the outlet pressure of the electrolyzer, the higher the density at which compressed hydrogen is stored, enabling a lower footprint for the subsequent hydrogen storage unit. Moreover, higher outlet pressures of the electrolyzer potentially compensate the necessity for an additional compressor in the system and might lead to cost advantages.

**Table 4.3:** Results of WSM for subsystem hydrogen generation

	System	TRL	Footprint	Cost	Pressure	Flexibility	$A_{WSM,H_2Gen}$
$w_j$	0.3	0.2	0.2	0.1	0.1	0.1	
AE	5	10	5	10	6	6	7.3
PEME	8	9	8	8	8	8	9
SOE	4	6	5	5	6	6	5.7
AEME	8	8	8	8	6	8	8.4

On the same priority level as the differential pressure are the costs as well as the operational flexibility of the unit. The comparably low priority for cost can be explained by the much higher importance of technical feasibility in the concept phase rather than a focus on the economic perspective of the technology. Therefore, also the operational flexibility of the unit is regarded as a major technical criterion for rating dynamic operation, which is required due to the use of volatile renewable energy. As depicted in Table 4.3, PEME is the preferred technology for off-grid use in selfHY<sup>®</sup>.

Even though the differences to AEME are not severe, the PEME shows advantages with regards to TRL and higher differential pressure operation as described in Subsection 3.2.2. Higher differential pressure operation of PEME is possible due to improved membrane design and more operational experience as compared to AEME, which is viewed as a rather new technology entering the market in recent years. AE on the other hand is the technology with the longest presence in the market and the lowest cost. For these

reasons AE is the preferred solution when it comes to the realization of large-scale electrolysis plants (e.g. NEOM Green Hydrogen Project in Saudi-Arabia) and is usually avoided when compact design, operational flexibility and differential pressure operation is required. As the single representative of the high-temperature electrolysis, the main issues for a use of SOE in selfHY<sup>®</sup> are the demanding material requirements, the low product lifetime and challenges with system integration of this technology. However, it needs to be mentioned that the SOE allows reversible operation as electrolyzer or fuel cell due to similarities in membrane and unit design. Until now, this advantage has not exploited its maximum potential and with its very low TRL it is not relevant for commercial applications.

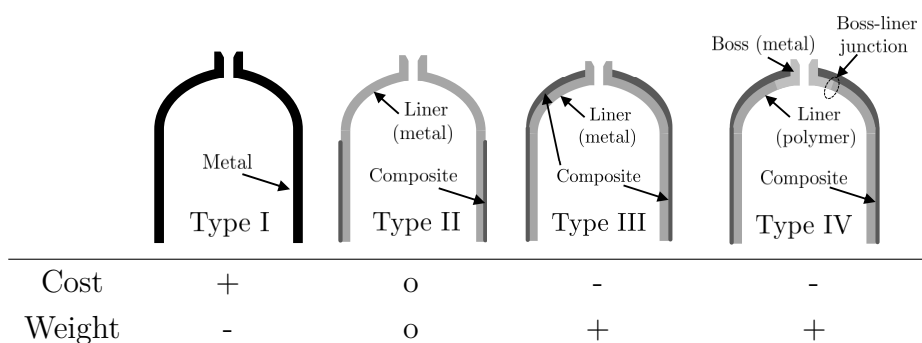
#### 4.1.4 Hydrogen Storage

As presented in Section 3.3, there are four main technologies for hydrogen storage to consider for selfHY<sup>®</sup>. In the following they are valued according to the suitability in the overall system, TRL, footprint, cost and energy demand for enabling the storage (e.g. electrical energy required for compression in case of CH<sub>2</sub>). The criterion with the highest priority is the footprint of the storage solution owed to the requirement of a compact integration of the storage system in the container. This is followed by the three criteria with the same weighing factor  $w_j$ : system, TRL and cost. The energy demand for enabling storage is considered as separate criterion due to high influence on the costs for a potential expansion of the renewable energy source resulting also in a larger footprint of selfHY<sup>®</sup>.

In order to store hydrogen, it is practicable to condition hydrogen in such a manner that beneficial storage conditions are achieved. As an example, hydrogen produced by electrolysis can be liquefied and therefore brought to state of higher density. However, the liquefaction process is very energy consuming and requires additional equipment such as heat exchangers and compressors as explained in Section 3.3. This is the reason why conditioning hydrogen to liquid state or storing hydrogen in carrier molecules such as LOHC is only reasonable for large-scale applications and in most cases connected to more efficient transportation of energy over longer distances. On the other hand, for off-grid and small-scale applications, it can be presumed that the fewer process steps are needed from the initial state of hydrogen to the storage state, the more favorable this solution appears. As a result, a simple and compact design of the system can be achieved with a minimum number of components required. This is the main reason why in the case of selfHY<sup>®</sup> compressed hydrogen prevails as the optimal storage solution. It is assumed that the hydrogen is already sufficiently pressurized in the hydrogen generation process and thereby the need for a compressor is eliminated. With regards to technology readiness level CH<sub>2</sub> has been an established way of storing hydrogen in small amounts as well as in bulk. Compared to the other options, CH<sub>2</sub> is the preferred choice for small-scale storage and backup power supply. Depending on the amount and storage pressure of hydrogen, different types of vessels can be utilized.

In general, there are four types of storage vessels used in commercial applications today differing in their structural design. Type I pressure vessels are made of metal while type II vessels use a thick metal liner hoop wrapped with composite material made from a fiber and resin. Type III vessels utilize composite material with a metal liner while type IV pressure vessels are built with composite material and a polymer liner. The outside is wrapped with carbon fibers embedded in a polymer matrix. If the liner contributes less than 5% to the mechanical resistance, the pressure vessel is of type IV, otherwise type III [BARTHELEMY ET AL. 2017]. Figure 4.2 visualizes the structure of the different pressure vessel types as previously described.

**Figure 4.2:** Layer structure of type I, II, III, IV according to BARTHELEMY ET AL. 2017



For the integration in a standardized container, it is important not to exceed the maximum payload of the container. Therefore, the weight of the hydrogen storage solution is an important aspect and the reason why type IV vessels as evaluated in Table 4.4 are preferred for selfHY<sup>®</sup>. LH<sub>2</sub> and LOHC show major disadvantages with regards to footprint, cost and energy required for hydrogen processing. In particular, additional equipment and system complexity as mentioned in Section 3.3 impedes the use of LH<sub>2</sub> or LOHC for small-scale off-grid applications. On the contrary, metal hydrides do not need additional energy for conditioning hydrogen, have a very low footprint in relation to the amount of stored hydrogen and allow integration in a containerized system. However, the technology is not widely used, has disadvantages with regards to weight and is in general more expensive than CH<sub>2</sub>. Another downside is that the dehydration of hydrogen from the metal hydride usually occurs at ambient pressure posing challenges to subsequent components such as fuel cells, which require higher inlet pressure.

**Table 4.4:** Results of WSM for subsystem hydrogen storage

	System	TRL	Footprint	Cost	Energy	$A_{WSM, H_2Store}$
$w_j$	0.3	0.15	0.2	0.1	0.1	
CH <sub>2</sub>	8	10	7	8	6	8.5
LH <sub>2</sub>	2	8	4	2	5	4.6
LOHC	3	7	3	3	3	4.1
Metal hydrid	6	5	10	4	10	8

### 4.1.5 Hydrogen Reconversion

The subsystem hydrogen reconversion changes the chemical energy of hydrogen to electrical energy and heat. This can be carried out by internal combustion engines (ICE) with generators or fuel cells. Even though combustion of hydrogen does not produce CO<sub>2</sub>, except for very small traces due to possible oil ingress in the burning chamber, NO<sub>x</sub>-emissions are an important factor to look at. In general, the faster the combustion occurs, the higher the efficiency of the energy conversion, but also the NO<sub>x</sub>-emissions increase. In contrast to that, fuel cells powered by hydrogen only emit water and heat without any harmful emissions locally [KLELL ET AL. 2018]. For this reason, the following evaluation excludes internal combustion engines with hydrogen and focuses on fuel cell solutions for the subsystem hydrogen reconversion.

As elaborated in Section 3.4, there have been numerous fuel cell technologies developed in the past. In conformity with the criteria and weighing factors  $w_j$  from the subsystem hydrogen generation (see Subsection 4.1.3), the WSM is performed for the subsystem hydrogen reconversion. The criteria pressure and flexibility of operation are exchanged by efficiency and product life due to higher relevance for the subsystem hydrogen reconversion.

In Table 4.5 the results of the WSM are shown, concluding PEMFC as the best available technology for hydrogen reconversion. DMFC disqualifies due to the circumstance that methanol is required as fuel, which is not foreseen in selfHY®. High temperature fuel cells such as MCFC and SOFC are difficult to integrate in the container system and the handling of high temperatures of above 600 °C requires high-grade material resulting in higher costs of the components and the system.

Even though PAFC show the best performance in terms of product life time, the low volumetric energy density causes problems for integration in a container and leads to a larger footprint compared to PEMFC. Similar as in the subsystem hydrogen generation, the alkaline solution for the fuel cell is preferable over PEMFC with regards to costs and efficiency. However, a more difficult integration due to an additional loop for the liquid electrolyte and a larger footprint per kW installed hinders AFC to be the optimal solution.

PEMFC as a low-temperature fuel cell with the lowest footprint and complexity of system design is the most suitable choice for selfHY® as it is for many stationary and



**Table 4.5:** Results of WSM for subsystem hydrogen reconversion

	System	TRL	Footprint	Cost	Efficiency	Product Life	$A_{WSM,H_2Rec}$
$w_j$	0.3	0.2	0.2	0.1	0.1	0.1	
AFC	6	9	5	10	6	5	6.7
PEMFC	8	10	9	8	5	6	8.1
DMFC	0	10	4	4	5	4	4.1
PAFC	5	7	4	7	5	9	5.8
MCFC	3	7	5	4	7	5	4.9
SOFC	3	5	8	6	8	6	5.5

mobility applications. Reasonable cost and life span as well as high TRL round up the characteristics of PEMFC [AKINYELE ET AL. 2020].

#### 4.1.6 Auxiliary Equipment

Besides the main components represented by the subsystems, auxiliary equipment is necessary for full functionality. For sizing and modeling of selfHY<sup>®</sup> size, power and weight of the auxiliary components need to be taken into account, in particular with regards to the integration of auxiliary equipment within the container. Typical components required for balance of plant include the following:

- Rectifiers
- Transformers
- Electrical converters
- Air compressor
- Control units
- Chillers
- Separator tanks
- Ventilation
- Mounting

These components need to be commercially available, proven technology and as compact as possible for the integration in or on a container.

## 4.2 Configuration of selfHY<sup>®</sup>

As a result, from the requirement analysis in Section 4.1, the optimal configuration of selfHY<sup>®</sup> is determined and the general process is further evolved resulting in a top-level block flow diagram shown in Figure 4.3. For a better overview of all energy consumers

in the system, the subsystem hydrogen generation is split into its three process steps of water treatment, electrolysis and hydrogen purification.

Moreover, electrical converters are considered as well as a battery system with its respective battery charger, which includes a bidirectional AC/DC converter with a control unit. The battery is foreseen in order to ensure sufficient energy for start-up of the fuel cell, a fast response on possible peak loads and to store electrical energy at times of insufficient power for the electrolyzer.

However, the degree of hybridization  $DOH$  of the system, as defined in Equation (4.2), needs to be as low as possible so that the power  $P_{FC,AC}$  provided by the fuel cell over a time period  $t$  is primarily used to cover the major portion of electrical energy demand [SONG ET AL. 2019]. Equation (4.2) is relevant for times when renewable energy is not available and reconversion of hydrogen is used to cover  $P_{Load}$ . The battery discharge power  $P_{Bat,AC}$  is particularly required at times when no renewable energy is available and the electrical energy demand  $P_{Load}$  is below the minimum operating threshold  $P_{Ely,DC,min}$  of the fuel cell. Once the minimum operating threshold of the fuel cell is reached again, the electrical consumers are supplied with power from the fuel cell directly and the battery is recharged.

$$DOH = \frac{\int_0^t P(t)_{FC,AC} dt}{\int_0^t P(t)_{Load} dt} = \frac{\int_0^t P(t)_{Load} - \int_0^t P(t)_{Bat,AC} dt}{\int_0^t P(t)_{Load} dt} \quad (4.2)$$

In Figure 4.3 and Table 4.6 the process and energy streams as well as the respective technologies used in the subsystems are depicted. Based on this configuration with PV, PEME, CH<sub>2</sub> and PEMFC the modeling and sizing of selfHY<sup>®</sup> is performed.

**Table 4.6:** Stream table of selfHY<sup>®</sup>

Stream	Type	Variable	Stream	Type	Variable
1	Electrical	$P_{PV,DC}$	12	Hydrogen	$\dot{V}_{H_2,Ely}$
2	Electrical	$P_{PV,AC}$	13	Electrical	$P_{HP}$
3	Electrical	$P_{WT}$	14	Hydrogen	$\dot{V}_{H_2,Store}$
4	Feed water	$\dot{V}_{W,in}$	15	Electrical	$P_C$
5	Potable water	$\dot{V}_{W,pot}$	16	Hydrogen	$\dot{V}_{H_2,Rec}$
6	Waste Water	$\dot{V}_{W,out}$	17	Electrical	$P_{FC,DC}$
7	Demineralized Water	$\dot{V}_{W,demi}$	18	Electrical	$P_{FC,AC}$
8	Electrical	$P_{Ely,AC}$	19	Heat	$\dot{Q}_{FC}$
9	Electrical	$P_{Ely,DC}$	20	Electrical	$P_{Bat,AC}$
10	Heat	$\dot{Q}_{Ely}$	21	Electrical	$P_{Bat,DC}$
11	Oxygen	$\dot{V}_{O_2}$	22	Electrical	$P_{Load}$

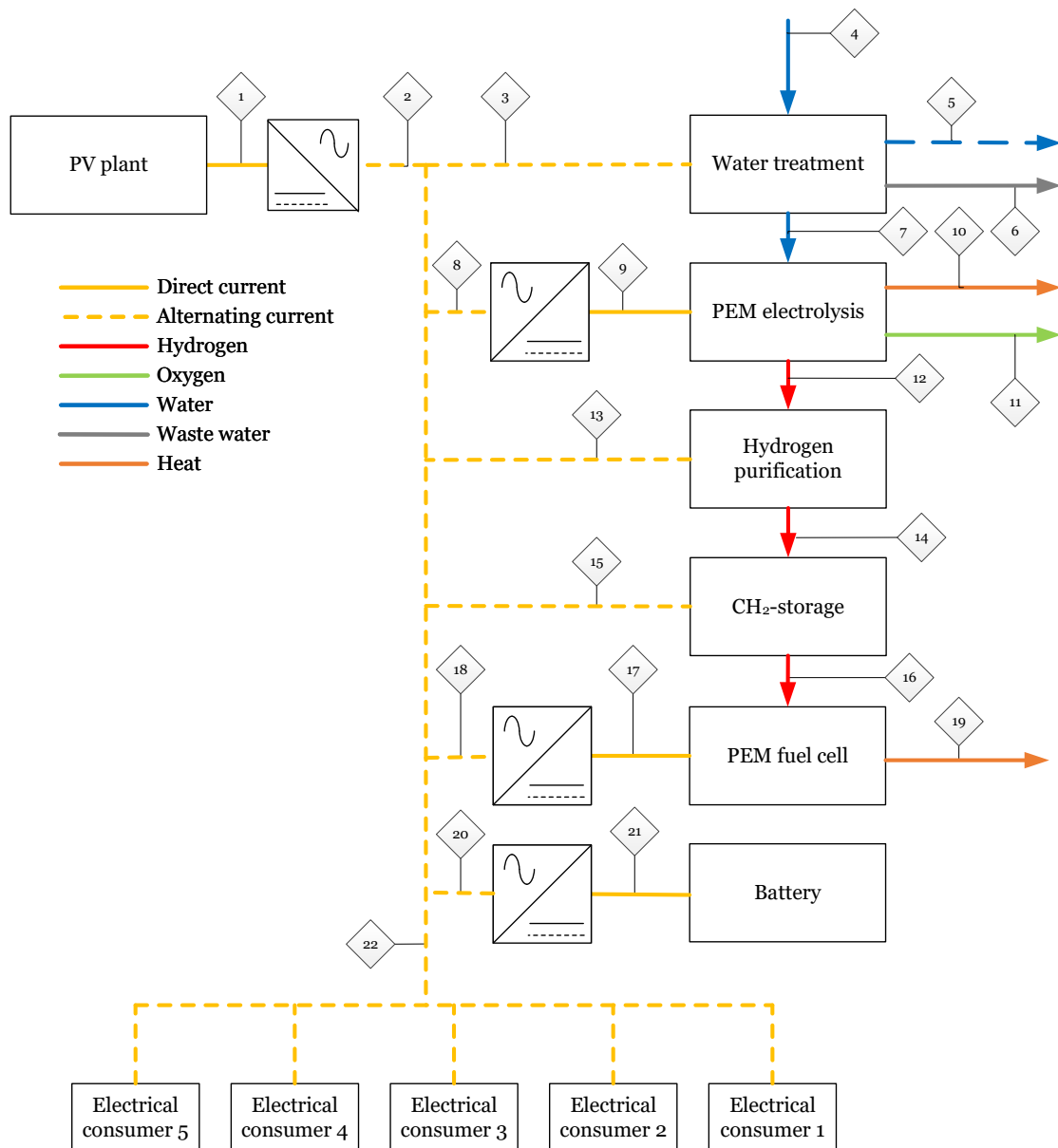


**Figure 4.3:** Block flow diagram of selfHY<sup>®</sup> with streams from Table 4.6



# 5 Modeling of selfHY<sup>®</sup>

As shown in Figure 4.3, selfHY<sup>®</sup> can be viewed as a system consisting of electrical energy and process streams with its corresponding components. The main modeling goal is to determine the power and size requirements for each component while ensuring sufficient energy supply to meet electrical consumer demands. In this chapter, the general operating philosophy is described before going into detail on the system modeling for hydrogen generation, storage and reversion. Moreover, sizing of additional equipment needed for balance of plant such as chillers, separator vessels, batteries and converters are included in the model. At last, the modeling of the PV plant is conducted based on the renewable energy supply  $P_{PV,DC}$  required to power selfHY<sup>®</sup>.

## 5.1 Operating Philosophy

There are four main operating modes of selfHY<sup>®</sup>, which can be differentiated based on their active energy and process streams. The most direct way is to use available power from the PV plant  $P_{PV,AC}$  to supply the electrical consumers with energy  $P_{Load}$ . In that case  $P_{PV,AC}$  equals  $P_{Load}$  and no hydrogen is produced. However, at times when  $P_{PV,AC}$  is larger than  $P_{Load}$ , the electrical energy demand is met and additionally hydrogen is generated via electrolysis by the surplus energy, representing the hydrogen generation operating mode as shown in Appendix A.

The second operating mode is the hydrogen reversion of the stored hydrogen via fuel cell, which is only active at times when no renewable energy is available (see Appendix A). Hydrogen is taken from the hydrogen storage, reconverted to electrical energy and heat, thereby covering the energy demand of the electrical consumers. A buffer battery ensures start-up of the fuel cell, peak-load coverage and energy supply for operation below the minimum operating threshold for hydrogen generation.

The third operating mode occurs if surplus energy from the PV plant is available, but lies below the threshold of minimum hydrogen generation power  $P_{Ely,DC,min}$  (see Appendix A). In order to use this energy, the battery is charged with it. Once the minimum hydrogen generation power  $P_{Ely,DC,min}$  is exceeded, the battery charging stops and the operation is shifted to hydrogen generation.

The fourth operating mode includes unsteady operations such as maintenance, start-up and emergency venting. These operations are needed for a functioning system, but due to their seldom occurrence and irrelevance for regular operation, they are not considered in this modeling of selfHY<sup>®</sup>.

In order to determine the operating mode depending on the renewable energy  $P_{PV,AC}$  available and the given load  $P_{Load}$ , the parameter  $\Delta P$  is introduced and defined as shown in Equation (5.1).

$$\Delta P(t) = P_{PV,AC}(t) - P_{Load}(t) \quad (5.1)$$

$\Delta P$  describes the surplus or lack of power in the system and thereby identifies the operating mode. If  $\Delta P$  is positive the operating mode hydrogen generation with its corresponding streams is active, otherwise if  $\Delta P$  is negative hydrogen reconversion is active. In the case of  $\Delta P$  being positive but below the threshold for minimum hydrogen generation  $P_{Ely,DC,min}$ , the third operating mode is enabled and the battery is charged. The operating modes and streams as well as the conditions when they are active are summarized in Appendix A.

The main challenge for selfHY<sup>®</sup> is to ensure that at all times sufficient hydrogen can be taken from the storage to cover the electrical load  $P_{Load}$  while the size of the storage system needs to be as compact as possible in order to fit into the container. For this reason, the parameter for hydrogen balance  $\Delta E_{H_2}$  is defined as shown in Equation (5.1).

$$\Delta E_{H_2}(t) = \int_{t_0}^{t_{End}} \dot{V}_{H_2,Store}(t) \cdot LHV_{H_2} dt - \int_{t_0}^{t_{End}} \dot{V}_{H_2,Rec}(t) \cdot LHV_{H_2} dt \quad (5.2)$$

By ensuring that the hydrogen balance  $\Delta E_{H_2}$  is equal or greater than zero, the availability of hydrogen for reconversion is guaranteed at all times. If the hydrogen balance  $\Delta E_{H_2}$  is below zero, the renewable power  $P_{PV,AC}$  is increased iteratively and the size and power of the components are determined in line with the modeling approach. In Figure 5.1 the iteration process used in the model is visualized, using the hydrogen balance  $\Delta E_{H_2}$  as criterion for stop of the iteration and simulation.

If the initial data input of the simulation results in a positive hydrogen balance  $\Delta E_{H_2}$  at all times, the iteration process decreases  $P_{PV,AC}$  in order to ensure the most compact hydrogen storage and is stopped prior to the iteration step when the hydrogen balance  $\Delta E_{H_2}$  becomes negative. In contrast, if the initial data input leads to negative hydrogen balance, the renewable energy  $P_{PV,AC}$  is raised until the positive hydrogen balance is reached. As the operating philosophy and iteration process of the model is clarified, the next sections include the detailed modeling approach of the relevant subsystems.

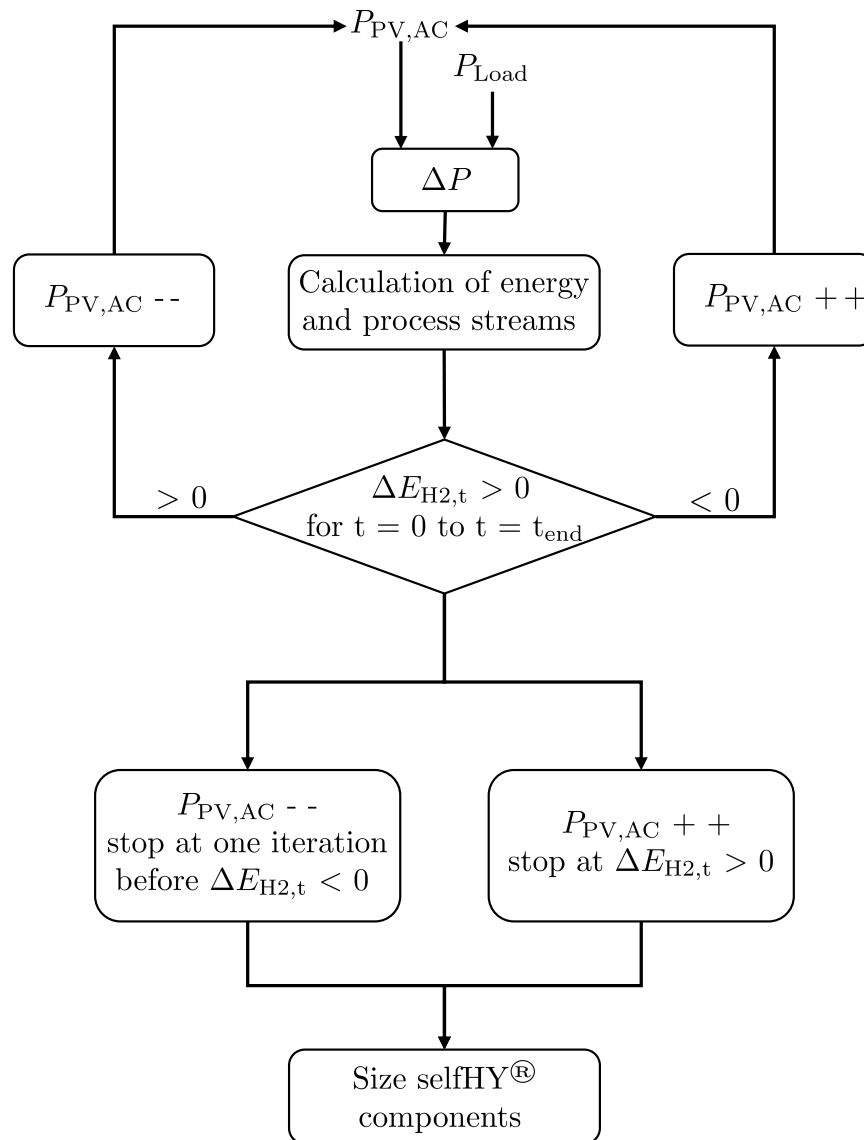


**Figure 5.1:** Iteration process for sizing of selfHY<sup>®</sup>

## 5.2 Hydrogen Generation

As described in Section 5.1, the hydrogen generation is the core element of selfHY® to ensure reliable energy supply. If the electrical load  $P_{Load}$  is covered by the renewable energy supply and  $\Delta P$  is positive as well as above the threshold of minimum power for hydrogen generation  $P_{Ely,DC,min}$ , the hydrogen generation components such as water treatment, electrolysis and hydrogen purification are active energy consumers. Based on the electrolysis and the corresponding hydrogen output  $\dot{V}_{H_2,Store}$ , the energy and process parameters of the water treatment and purification are determined.

For modeling the electrolysis process, the input variables and parameters from Table 5.1 are used. The first step is to consider the efficiency of the AC/DC converter  $\eta_{AC/DC,Ely}$  and scaling  $\Delta P$  accordingly as per Equation (5.3):

$$P_{Ely,DC}(t) = \eta_{AC/DC,Ely} \cdot \Delta P(t). \quad (5.3)$$

By taking  $P_{Ely,DC}$  and dividing it with the maximum value of  $P_{Ely,DC}$  (see Equation (5.4)) of the entire time series, the load  $L_{Ely}$  of the electrolyzer is defined:

$$L_{Ely}(t) = \frac{P_{Ely,DC}(t)}{\max[P_{Ely,DC}(t)]} = \frac{P_{Ely,DC}(t)}{P_{Ely,DC,max}}. \quad (5.4)$$

For electrolysis, as well as for fuel cells, polarization curves are used to determine the electrical current or current densities in relation to the operating voltage of a cell. In order to determine the operating voltage  $U_{Ely,Cell}$  of a single cell, the load  $L_{Ely}$  of the electrolyzer and the operating voltage boundaries  $U_{Ely,min}$  and  $U_{Ely,max}$  are set in correlation as per Equation (5.5):

$$U_{Ely,Cell}(t) = U_{Ely,min} + L_{Ely}(t) \cdot (U_{Ely,max} - U_{Ely,min}). \quad (5.5)$$

The relation of the electrolyzer load  $L_{Ely}$  and the operating voltage  $U_{Ely}$  is assumed linear between the operating boundaries in this model. However, the behavior can vary depending on the electrolyzer, available power and implemented controls of the system and needs to be adapted accordingly. Using the operating voltage  $U_{Ely}$  and the polarization curve of the electrolyzer cell, the current density  $i_{Ely}$  is determined and allows the conclusion of the power density per area  $j_{Ely,Cell}$  of a single cell:

$$j_{Ely,Cell}(t) = U_{Ely,Cell}(t) \cdot i_{Ely}(t). \quad (5.6)$$

The polarization curve for this model is shown in Figure 5.2 and represents a typical PEME polarization curve with a 150  $\mu\text{m}$  thick Nafion® membrane according to KLOSE ET AL. 2020. For the membrane electrode assembly (MEA) on the anode side IrO<sub>2</sub> and Nafion® are utilized, for the cathode side a Pt/C catalyst and Nafion® are used.



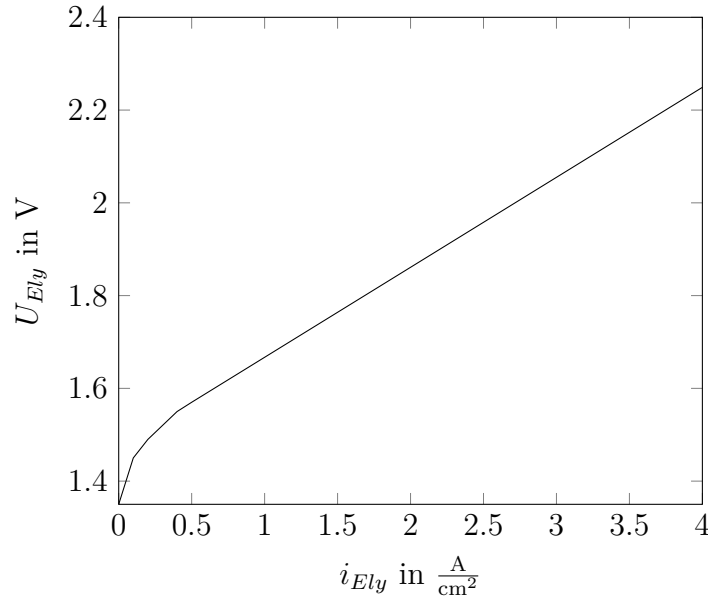


**Figure 5.2:** Polarization curve of PEME used in model

The total active area  $A_{Ely,act}$  needed in one electrolyzer stack is determined by dividing the available power for electrolysis  $P_{Ely,DC}$  with the power per area of one single cell  $j_{Ely,Cell}$  (see Equation (5.7)). The active area per stack  $A_{Ely,Stack}$  and the cells per stack  $N_{Ely,Stack,Cell}$  can be calculated using Equation (5.8) and (5.9), where  $N_{Ely,Stack}$  is the number of electrolyzer stacks and  $A_{Ely,Cell}$  the active area per cell. In case  $N_{Ely,Stack} = 1$ , the  $A_{Ely,Stack}$  equals to  $A_{Ely,act}$ . The single cells in a electrolyzer stack are connected in series, therefore the product of the electrolyzer cells per stack  $N_{Ely,Stack,Cells}$  with the operating voltage  $U_{Ely,Cell}$  results in the voltage across one stack  $U_{Ely,Stack}$  (see Equation (5.10)).

$$A_{Ely,act}(t) = \frac{P_{Ely,DC}(t)}{j_{Ely,Cell}(t)} \quad (5.7)$$

$$A_{Ely,Stack}(t) = \frac{A_{Ely,act}(t)}{N_{Ely,Stack}} \quad (5.8)$$

$$N_{Ely,Stack,Cell}(t) = \frac{A_{Ely,Stack}(t)}{A_{Ely,Cell}} \quad (5.9)$$

$$U_{Ely,Stack}(t) = N_{Ely,Stack,Cell}(t) \cdot U_{Ely,Cell}(t) \quad (5.10)$$

As elaborated in Subsection 3.2.2, the correlation between the electrical current  $I_{Ely}$  for electrolysis and the hydrogen production  $\dot{V}_{H_2,Store}$  is in context with the law of Faraday and therefore the hydrogen generation is proportional to the applied current in the electrolyzer [STERNER & STADLER 2017]:

$$\dot{V}_{H_2,Store}(t) = \eta_F \frac{i_{Ely}(t) \cdot A_{Ely,act}(t) \cdot \Delta t \cdot M_{H_2}}{z \cdot F \cdot \varrho_{H_2,st}} = \eta_F \frac{I_{Ely}(t) \cdot \Delta t \cdot M_{H_2}}{z \cdot F \cdot \varrho_{H_2,st}}. \quad (5.11)$$

Equation (5.11) is used to calculate the hydrogen generation for each time step  $\Delta t$ , thereby expanding the conventional Faraday relation with the molar mass of hydrogen  $M_{H_2}$  and its standard density  $\rho_{H_2, st}$ . In this model, no hydrogen losses in the downstream processing are assumed. The constant  $z = 2$  describes the number of electrons exchanged when water is split, whereas  $F$  is the Faraday constant. Another aspect to consider is the Faraday efficiency  $\eta_F$ . It accounts for numerous loss mechanisms in the electrolysis process such as hydrogen diffusion losses through the membrane or electrical current losses.

With increasing operating temperature, the Faraday efficiency  $\eta_F$  decreases and leads to efficiency and operating problems, especially at lower current densities. As the operating window of electrolysis in this model is above a current density of  $0.1 \frac{A}{cm^2}$ , the Faraday efficiency can be assumed as constant resulting from the trend depicted in Figure 5.3 [YODWONG ET AL. 2020].

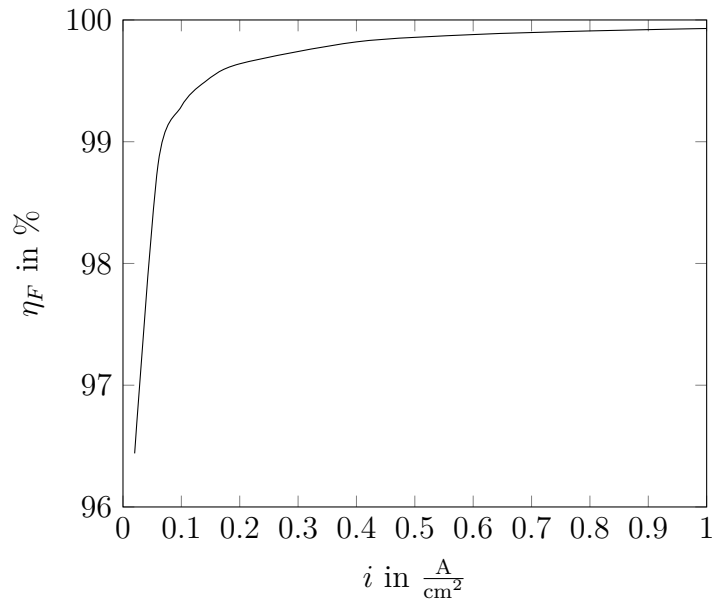


**Figure 5.3:** Faraday efficiency curve according to YODWONG ET AL. 2020

In order to calculate the overall efficiency of the electrolysis, which is the ratio of energy contained in the produced hydrogen and the electrical energy input, either the lower or the higher heating value of hydrogen can be used. In this model the efficiency  $\eta_{Ely}$  is calculated by using the lower heating value  $LHV_{H_2}$  and the following equation:

$$\eta_{Ely}(t) = \frac{\dot{V}_{H_2, Store}(t) \cdot LHV_{H_2}}{\Delta P_{DC}(t)}. \quad (5.12)$$

As depicted in Figure 4.3, electrolysis produces oxygen and also heat. The oxygen output  $\dot{V}_{O_2}$  can be calculated with the Faraday relation applied on the hydrogen generation in Equation (5.11) and by changing the molar mass and standard density to the values for oxygen.

Moreover, the endothermic reaction of electrolysis produces heat  $\dot{Q}_{Ely}$ , which needs to be dissipated in order to maintain the constant operating temperature of the electrolyzer. Assuming that all energy not used for hydrogen generation is dissipated as heat, the cooling duty equals to the produced heat  $\dot{Q}_{Ely}$  as defined per Equation (5.13). The corresponding mass flow  $\dot{m}_{Ely,cool}$  for cooling is determined by division with the enthalpy difference  $\Delta h_{Ely,cool}$  of the inlet and outlet water for electrolysis (see Equation (5.14)).

$$\dot{Q}_{Ely}(t) = \Delta P(t) - \dot{V}_{H_2,Store}(t) \cdot LHV_{H_2} \quad (5.13)$$

$$\dot{m}_{Ely,cool}(t) = \frac{\dot{Q}_{Ely}(t)}{\Delta h_{Ely,cool}} \quad (5.14)$$

As a result of this calculation, relevant valve positions of control valves in the cooling circuit can be adjusted accordingly to ensure sufficient cooling of the water used for electrolysis. All variables and parameter relevant for the electrolysis modeling are summarized in Table 5.1 and identified as input or output from the model.

**Table 5.1:** In- and output variables and parameters of electrolysis model

	Variable	Parameter	Input	Output
$A_{Ely,act}$	✓			✓
$A_{Ely,Cell}$		✓	✓	
$A_{Ely,Stack}$	✓			✓
$F$		✓	✓	
$\Delta h_{Ely,cool}$		✓	✓	
$i_{Ely}$	✓			✓
$I_{Ely}$	✓			✓
$j_{Ely,Cell}$	✓			✓
$L_{Ely}$	✓			✓
$LHV_{H_2}$		✓	✓	
$\dot{m}_{Ely,cool}$	✓			✓
$M_{H_2}$		✓	✓	
$N_{Ely,Stack}$		✓	✓	
$N_{Ely,Stack,Cell}$		✓		✓
$P_{Load}$	✓		✓	
$P_{Ely,DC}$	✓			✓
$P_{Ely,DC,max}$			✓	✓
$P_{Ely,DC,min}$			✓	✓
$\dot{Q}_{Ely}$	✓			✓
$\Delta t$		✓	✓	
$U_{Ely,Cell}$	✓			✓
$U_{Ely,max}$		✓		✓
$U_{Ely,min}$		✓		✓
$U_{Ely,Stack}$	✓			✓
$\dot{V}_{H_2,Store}$	✓			✓
$z$		✓	✓	
$\eta_{AC/DC,Ely}$		✓	✓	
$\eta_{Ely}$	✓			✓
$\eta_F$		✓	✓	
$\varrho_{H_2,st}$		✓	✓	

By determining the hydrogen output  $\dot{V}_{H_2,Store}$ , other system components such as water treatment system, oxygen and hydrogen separator can be sized. If applicable, their power consumption is estimated as well.

Starting with the water treatment system as subsystem of the hydrogen generation upstream the electrolysis, it can be stated that the process design and component size is affected by the expected feed water quality. The water quality can range from pure seawater with a high number of total dissolved solids (TDS) to tap water or rain water with relatively low amounts of TDS. In this model it is assumed that groundwater is provided as feed water and purified via softening unit, reverse osmosis and electrical deionization. The main parameters for input water quality and the desired output quality of the deionized water are summarized in Table 5.2. As input variables for the

**Table 5.2:** Water specification used in model

	Feed water	Deionized water	Potable water
Hardness in °dH	15	0	< 14
TDS in $\frac{mg}{l}$	380	$\approx 0$	300 - 500
Conductivity in $\frac{\mu S}{cm}$	500	<1	>2790
pH-Value	8	7	6.5 - 9.5

water treatment system, the hydrogen output  $\dot{V}_{H_2,Store}$  and the demand for potable water  $\dot{V}_{W,pot}$  over the given time period  $t$  is needed. The hydrogen output  $\dot{V}_{H_2,Store}$  is derived from the electrolysis modeling and the potable water demand  $\dot{V}_{W,pot}$  is estimated according to the average potable water consumption  $\dot{V}_{W,pot,p.P.}$  per person at the foreseen location.

The required deionized water  $\dot{V}_{W,demi}$  for hydrogen generation is calculated by using the stoichiometric relation of the electrolysis process shown in Subsection 3.2.2, which leads to the conclusion that under ideal conditions for each standard cubic meter of hydrogen generated, 0.803 L of deionized water are needed. This conversion factor  $c_{W,demi}$  is multiplied with the hydrogen output  $\dot{V}_{H_2,Store}$  and results in the ideal demineralized water demand. In order to model inefficiencies caused by deviation from an ideal water treatment process and the rejection rate of the feed water, the efficiency  $\eta_{WT}$  of the water purification is applied as depicted in Equation (5.15).

$$\dot{V}_{W,demi}(t) = \frac{\dot{V}_{H_2,Store}(t) \cdot c_{W,demi}}{\eta_{WT}} = \frac{\dot{V}_{H_2,Store}(t) \cdot \frac{\frac{\Delta N_{H_2O} M_{H_2O}}{\varrho_{H_2O,st}}}{\frac{\Delta N_{H_2} M_{H_2}}{\varrho_{H_2,st}}}}{\eta_{WT}} \quad (5.15)$$

By applying the efficiency  $\eta_{WT}$  of the water purification also on the potable water demand  $\dot{V}_{W,pot}$  and adding the water required for electrolysis  $\dot{V}_{W,demi}$ , the total amount of feed water  $\dot{V}_{W,in}$  is determined according to Equation (5.16).

$$\dot{V}_{W,in}(t) = \frac{\dot{V}_{W,pot}(t)}{\eta_{WT}} + \dot{V}_{W,demi}(t) \quad (5.16)$$

The demineralized water stream intended for potable water generation is remineralized in an additional unit, but this process is not relevant for the further modeling approach. However, the installation of the remineralization unit is to be considered in the spatial integration within the container. Based on the total demineralized water generation  $\dot{V}_{W,in}$ , the respective waste water stream  $\dot{V}_{W,out}$  is calculated with the efficiency of the water treatment system  $\eta_{WT}$  according to Equation (5.17).

$$\dot{V}_{W,out}(t) = (1 - \eta_{WT}) \cdot \dot{V}_{W,in}(t) \quad (5.17)$$

The power  $P_{WT}$  needed to operate the water treatment unit is modeled using the output rate of demineralized water  $\dot{V}_{W,in}$ . Depending on the water quality and the water treatment technology, the specific energy consumption  $e_{WT}$  can range between 2 and  $5 \frac{\text{kWh}}{\text{m}^3}$ , thus the power for water treatment is calculated by Equation (5.18).

$$P_{WT}(t) = \dot{V}_{W,out}(t) \cdot e_{WT} \quad (5.18)$$

The variables and parameters relevant for the model of the water treatment are shown in Table 5.3.

**Table 5.3:** In- and output variables and parameters of water treatment model

	Variable	Parameter	Input	Output
	$e_{WT}$	✓	✓	
	$c_{W,demi}$	✓	✓	
	$M_{H_2}$	✓	✓	
	$M_{H_2O}$	✓	✓	
	$\Delta N_{H_2}$	✓	✓	
	$\Delta N_{H_2O}$	✓	✓	
	$P_{WT}$	✓		✓
	$\dot{V}_{H_2,Store}$	✓	✓	
	$\dot{V}_{W,demi}$	✓		✓
	$\dot{V}_{W,out}$	✓		✓
	$\dot{V}_{W,pot}$	✓		✓
	$V_{W,pot,p.P.}$	✓	✓	
	$\dot{V}_{W,in}$	✓		✓
	$\eta_{WT}$	✓	✓	
	$\varrho_{H_2,st}$	✓	✓	
	$\varrho_{H_2O,st}$	✓	✓	

Downstream of the water treatment, the demineralized water reaches the oxygen separator tank, where the generated oxygen  $\dot{V}_{O_2,out}$  at the anode of the PEME is vented and the demineralized water used for electrolysis is contained. As depicted in Figure 5.4, the water  $\dot{V}_{W,demi}$  enters the oxygen separator and compensates the water amount which is processed in the electrolyzer. The demineralized water is brought to the inlet of the electrolyzer  $\dot{V}_{W,Ely,in}$  from the oxygen separator by a transfer pump and is processed at the anode of the PEME, where gaseous oxygen  $\dot{V}_{O_2,Ely,out}$  and unprocessed demineralized water  $\dot{V}_{W,Ely,out}$  are recycled to the oxygen separator. Furthermore, it is assumed that the oxygen separator works at ambient pressure and that the maximum mass flow for cooling is used to size the separator.

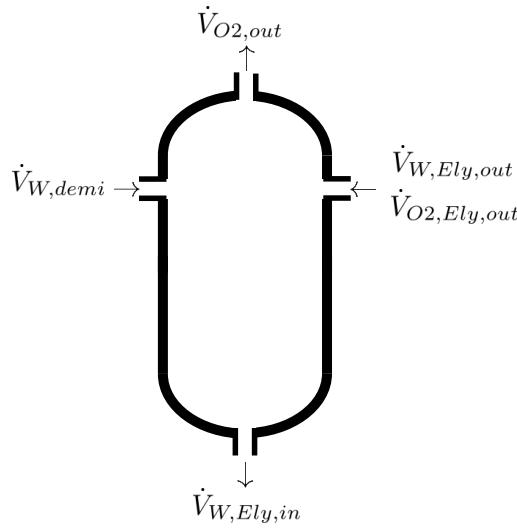


**Figure 5.4:** In- and Outlet streams of the oxygen separator

The volume flow  $\dot{V}_{W,Ely,in}$  functions on one side as water supply for the electrolysis process, but also needs to ensure a sufficient flow rate in order to maintain the desired operating temperature of the electrolyzer. For this reason, the required mass flow is calculated as shown prior in Equation (5.14) allowing also to determine the respective volume flow for sufficient cooling  $\dot{V}_{W,Ely,in}$ :

$$\dot{V}_{W,Ely,in} = \frac{\max[\dot{m}_{Ely,cool}(t)]}{\rho_{H_2O,cool}}. \quad (5.19)$$

With the correlation of the processed water in the electrolysis being equal to the amount of supplied water  $\dot{V}_{W,demi}$ , the volume flow  $\dot{V}_{W,Ely,out}$  recycled to the oxygen separator is calculated as per Equation (5.20). The vented oxygen  $\dot{V}_{O_2,out}$  equals to  $\dot{V}_{O_2,Ely,out}$  and can be calculated with the Faraday relation, exemplary shown for hydrogen in Equation (5.11).

$$\dot{V}_{W,Ely,out} = \dot{V}_{W,Ely,in} - \dot{V}_{W,demi} \quad (5.20)$$



Another aspect to consider for the design of the oxygen separator is a sufficient liquid level at all times preventing the downstream pump to reach a critical operating mode. By using the parameter for retention time  $\tau$  in the separator and the volume flow  $\dot{V}_{W,Ely,in}$ , the liquid volume  $V_{W,liq}$  held up in the separator is determined according to following equation:

$$V_{W,liq} = \tau \cdot \dot{V}_{W,Ely,in} \quad (5.21)$$

Based on the liquid volume  $V_{W,liq}$  in the oxygen separator and the ratio of height and diameter  $r_{HD}$ , the total inner volume of the separator is calculated with its corresponding radius  $R_{Sep}$  and height  $H_{Sep}$  as shown in Equation (5.22) through (5.24).

$$V_{Sep} = r_{HD} \cdot V_{W,liq} = \frac{H_{Sep}}{R_{Sep}} \cdot V_{W,liq} \quad (5.22)$$

$$R_{Sep} = \left[ \frac{V_{Sep}}{2\pi r_{HD}} \right]^{\frac{1}{3}} \quad (5.23)$$

$$H_{Sep} = R_{Sep} \cdot r_{HD} \quad (5.24)$$

At last, it needs to be ensured, that the flow velocity  $u_{G,O_2}$  of oxygen (see Equation (5.25)) is below a certain threshold  $u_{G,max}$  at all times in order to make the separation of liquid water and gaseous oxygen possible. It can be assumed that if  $u_{G,O_2}$  remains below  $u_{G,max} \approx 0.5 \frac{m}{s}$ , thus the criterion can be seen as fulfilled.

$$u_{G,O_2} = \frac{\dot{V}_{O_2,Ely,out}}{\pi R_{Sep}^2} \quad (5.25)$$

Table 5.4 gives an overview of the variables and parameters used for the oxygen separator model.

**Table 5.4:** In- and output variables and parameters of oxygen separator model

	Variable	Parameter	Input	Output
	$H_{Sep}$	✓		✓
	$\dot{m}_{Elly,cool}$	✓	✓	
	$r_{HD}$	✓	✓	
	$R_{Sep}$	✓		✓
	$u_{G,O_2}$	✓		✓
	$u_{G,max}$	✓		✓
	$\dot{V}_{O_2,Elly,out}$	✓	✓	
	$\dot{V}_{O_2,out}$	✓	✓	
	$V_{Sep}$	✓		✓
	$\dot{V}_{W,demi}$	✓	✓	
	$\dot{V}_{W,Elly,in}$	✓		✓
	$\dot{V}_{W,Elly,out}$	✓		✓
	$V_{W,liq}$	✓		✓
	$\varrho_{H_2O,cool}$	✓	✓	
	$\tau$	✓	✓	

Under real process conditions, small amounts of water are dragged to the cathode side. As a result, the hydrogen outlet stream of the electrolyzer stack contains partly water which needs to be removed. This task is mainly fulfilled with a hydrogen separator (see Figure 5.5) located downstream the electrolyzer stack and upstream the hydrogen purification unit. The water in the hydrogen outlet stream is drained and recycled to the oxygen separator tank. For determining the size and capacity of the hydrogen separator and purification unit, the composition of the hydrogen output stream is calculated in more detail to gain knowledge on the fractions of hydrogen, water and oxygen in the hydrogen outlet stream. In this model the amount of water is estimated according to Equation (5.26) [ONDA ET AL. 2002] and the hydrogen generation  $N_{H_2,g}$  is derived from Equation (5.11). In the same manner as for the oxygen separator, the hydrogen separator is sized assuming maximum hydrogen production.

$$N_{H_2O,l} = (0.0134 \cdot T_{Elly} + 0.03) \cdot \max[N_{H_2,g}(t)] \quad (5.26)$$

Moreover, it is assumed that the gaseous water fraction downstream the hydrogen separator is in saturated state and therefore the pressure can be calculated using the Antoine equation with parameters  $A$ ,  $B$ ,  $C$  for water and the operating temperature  $T_{Elly}$  of the electrolyzer:

$$p_{H_2O} = 10^{A - \frac{B}{T_{Elly} + C}} \quad (5.27)$$

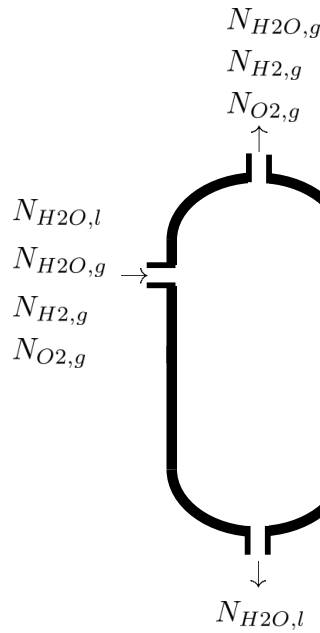


**Figure 5.5:** In- and Outlet streams of the hydrogen separator

As a result, the mole fraction  $y_{H_2O}$  is determined via partial pressure relation with the outlet pressure  $p_{El_y}$  of the electrolyzer:

$$y_{H_2O} = \frac{p_{H_2O}}{p_{El_y}}. \quad (5.28)$$

The oxygen crossover  $N_{O_2,g}$  is modeled according to TRINKE ET AL. 2017 and Equation (5.29), where  $c_{drag}$  is the drag coefficient,  $i_{El_y}$  the current density,  $F$  the Faraday constant,  $\rho_{H_2O}$  the density of water,  $M_{H_2O}$  the molar mass of water,  $p_{O_2}^a$  the partial pressure of oxygen at the anode,  $S_{O_2}$  the oxygen solubility in water and  $s$  the supersaturation factor.

$$N_{O_2,g} \approx c_{drag} \frac{\max[i_{El_y}(t)]}{F \frac{\rho_{H_2O}}{M_{H_2O}}} p_{O_2}^a S_{O_2} s \quad (5.29)$$

Consequently, the total amount of substance  $N_{out,g}$  leaving the hydrogen separator in gaseous state is the sum of the three components hydrogen, oxygen and water as shown in Equation (5.30). The amount of substance of hydrogen  $N_{H_2,g}$  is given by the hydrogen production from electrolysis (see Equation (5.11)).

$$N_{out,g} = N_{H_2,g} + \underbrace{y_{H_2O} \cdot N_{out,g}}_{N_{H_2O,g}} + N_{O_2,g} = \frac{N_{H_2,g} + N_{O_2,g}}{1 - y_{H_2O}} \quad (5.30)$$

The composition of the flow entering the hydrogen purification unit is determined using its corresponding mole fractions as depicted in Equation (5.31) through (5.33).

$$y_{\text{H}_2} = \frac{N_{\text{H}_2,g}}{N_{out,g}} \quad (5.31)$$

$$y_{\text{H}_2\text{O}} = \frac{N_{\text{H}_2\text{O},g}}{N_{out,g}} \quad (5.32)$$

$$y_{\text{O}_2} = \frac{N_{\text{O}_2,g}}{N_{out,g}} \quad (5.33)$$

Additionally, a hydrogen purification removes traces of condensate and oxygen in the hydrogen stream in order to ensure safe storage and sufficient quality of hydrogen for reconversion to electrical energy via fuel cell. The power consumption of the purification unit  $P_{HP}$  is assumed proportional to the hydrogen outlet flow  $\dot{V}_{\text{H}_2,Store}$  of the purification unit. The hydrogen outlet flow  $\dot{V}_{\text{H}_2,Store}$  is equal to the inlet flow  $\dot{V}_{\text{H}_2,Elly}$ . By using the specific power consumption factor  $c_{HP}$  according to Equation (5.34), the power consumption  $P_{HP}$  is calculated.

$$P_{HP}(t) = \dot{V}_{\text{H}_2,Store}(t) \cdot c_{HP} \quad (5.34)$$

All utilized variables and parameters for the modeling of the hydrogen separator are listed in Table 5.5.

**Table 5.5:** In- and output variables and parameters of hydrogen separator model

	Variable	Parameter	Input	Output
	$c_{drag}$	✓	✓	
	$c_{HP}$	✓	✓	
	$F$	✓	✓	
	$i_{Ely}$	✓	✓	
	$M_{H_2O}$	✓	✓	
	$N_{H_2,g}$	✓	✓	
	$N_{H_2O,g}$	✓	✓	
	$N_{H_2O,l}$	✓		✓
	$N_{O_2,g}$	✓		✓
	$N_{out,g}$	✓		✓
	$p_{O_2}^a$	✓	✓	
	$p_{Ely}$	✓	✓	
	$p_{H_2O}$	✓		✓
	$P_{HP}$	✓		✓
	$s$	✓	✓	
	$S_{O_2}$	✓	✓	
	$T_{Ely}$	✓	✓	
	$\dot{V}_{H_2,Store}$	✓	✓	
	$y_{H_2O}$	✓		✓
	$y_{H_2}$	✓		✓
	$y_{O_2}$	✓		✓
	$\varrho_{H_2O}$	✓	✓	

### 5.3 Hydrogen Reconversion

In contrast to hydrogen generation, hydrogen reconversion is active when no renewable energy is available and  $\Delta P$  is therefore negative. It is assumed that the energy needed from hydrogen reconversion  $P_{FC,AC}$  is fully provided by the fuel cell independently of the operating point. For loads below the minimum operating point of the fuel cell, the battery is active. However, the energy for charging the battery  $P_{Bat,AC}$  is provided fully by the fuel cell or the PV plant when operating below the minimum hydrogen generation power. Any losses due to electrical conversion in the battery charger are viewed as negligible in this model.

The main goal of the modeling of the hydrogen reconversion is to determine the actual hydrogen demand  $\dot{V}_{H_2,Rec}$  based on the required load  $P_{Load}$  at times with no renewable energy. Using the variable  $\Delta P$  as defined in Equation (5.1), the power of the fuel cell  $P_{FC,DC}$  is calculated considering the efficiency of the AC/DC converter  $\eta_{AC/DC,FC}$  as follows:

$$P_{FC,DC}(t) = -\frac{\Delta P(t)}{\eta_{AC/DC,FC}}. \quad (5.35)$$

In analogy to the modeling of the hydrogen generation, the load of the fuel cell  $L_{FC}$  is determined by Equation (5.36). The power  $P_{FC,DC}$  of the fuel cell is divided by the maximum value of  $P_{FC,DC,max}$  of the analyzed time series resulting in the load  $L_{FC}$  of the fuel cell.

$$L_{FC}(t) = \frac{P_{FC,DC}(t)}{\max[P_{FC,DC}(t)]} = \frac{P_{FC,DC}(t)}{P_{FC,DC,max}} \quad (5.36)$$

By using the operating voltage window of the fuel cell with its maximum operating voltage  $U_{FC,max}$  and the minimum operating voltage  $U_{FC,min}$  the present operating voltage is identified by following equation:

$$U_{FC,Cell}(t) = U_{FC,min} - L_{FC}(t) \cdot (U_{FC,min} - U_{FC,max}). \quad (5.37)$$

At this point it needs to be clarified that the minimum and maximum operating voltage are referring to the corresponding maximum and minimum current density  $i_{FC}$  according to the given polarization curve of the fuel cell. Due to the relation of increasing current density with lower voltage, the value of the maximum operating voltage  $U_{FC,max}$  is lower than the value of the minimum operating voltage  $U_{FC,min}$ .

For the hydrogen reconversion model the polarization curve of the PEMFC according to GOSHTASBI ET AL. 2019 is used, which is shown in Figure 5.6. Here, a relative humidity of 60%, a temperature of 70 °C and a stoichiometric air ratio of 2.5 at a pressure of 2.5 bar is assumed.

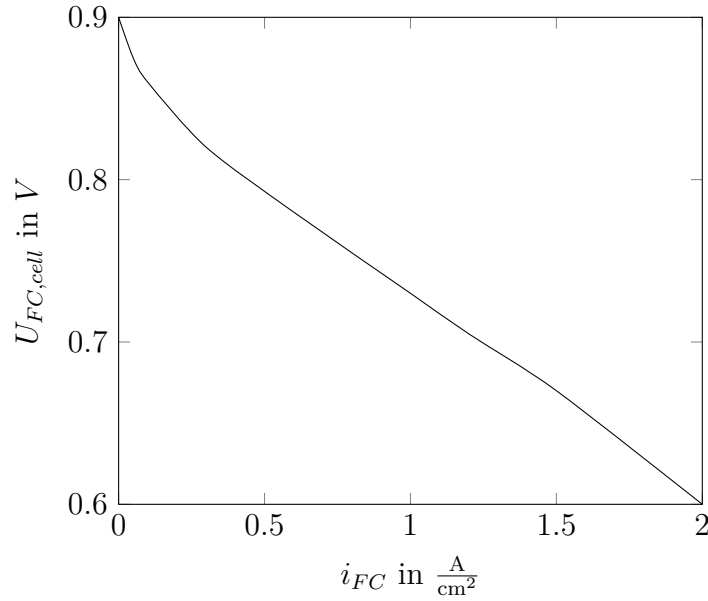


**Figure 5.6:** Polarization curve of PEMFC used in model

Based from the operating voltage  $U_{FC,Cell}$  and the polarization curve the current density  $i_{FC}$  is taken and used for the calculation of the total active area  $A_{FC,act}$  of the fuel cell for one single stack (see Equation (5.38)). By multiplying the result with the current density  $i_{FC}$  the electrical current  $I_{FC}$  is defined as per Equation (5.41) and the active area  $A_{FC,Stack}$  per stack is calculated according to Equation (5.39) using the quantity of stacks  $N_{FC,Stack}$ . Additionally, the number of cells  $N_{FC,Stack,Cells}$  per stack is determined by (5.40) considering the active area  $A_{FC,Cell}$  per cell.

$$A_{FC,act}(t) = -\frac{\Delta P(t)}{i_{FC}(t) \cdot U_{FC,cell}(t)} \quad (5.38)$$

$$A_{FC,Stack}(t) = \frac{A_{FC,act}(t)}{N_{FC,Stack}} \quad (5.39)$$

$$N_{FC,Stack,Cell}(t) = \frac{A_{FC,Stack}(t)}{A_{FC,Cell}} \quad (5.40)$$

$$I_{FC}(t) = i_{FC}(t) \cdot A_{FC,act}(t) \quad (5.41)$$

In the end, the hydrogen volume flow to the fuel cell  $\dot{V}_{H_2,Rec}$  is the crucial output variable of the subsystem for hydrogen reconversion and is calculated with the Faraday relation in Equation (5.42). Likewise as for the hydrogen generation, the  $LHV_{H_2}$  of hydrogen is used also in the hydrogen reconversion to determine the energy contained in the hydrogen and to calculate the efficiency  $\eta_{FC}$  as shown in Equation (5.43) as well as the mass flow  $\dot{m}_{FC,cool}$  for cooling of the fuel cell in Equation (5.44). It is assumed

that unused hydrogen in the fuel cell is recirculated and eventually used up, therefore no efficiency losses are accounted for hydrogen leakage or crossover.

$$\dot{V}_{H_2,Rec}(t) = \frac{i(t) \cdot A_{Ely,act}(t) \cdot \Delta t \cdot M}{z \cdot F \cdot \rho_{H_2,st}} = \frac{I(t) \cdot \Delta t \cdot M}{z \cdot F \cdot \rho_{H_2,st}} \quad (5.42)$$

$$\eta_{FC}(t) = \frac{\Delta P(t)}{\dot{V}_{H_2,Rec}(t) \cdot LHV_{H_2}} \quad (5.43)$$

$$\dot{m}_{FC,cool}(t) = \frac{\dot{Q}_{FC}(t)}{\Delta h_{FC,cool}} = \frac{-\Delta P(t) - \dot{V}_{H_2,Rec}(t) \cdot LHV_{H_2}}{\Delta h_{FC,cool}} \quad (5.44)$$

Table 5.6 depicts all parameters and variables used in the hydrogen reconversion model.

**Table 5.6:** In- and outputs of hydrogen reconversion model

	Variable	Parameter	Input	Output
$A_{FC,act}$	✓			✓
$A_{FC,Cell}$		✓	✓	
$A_{FC,Stack}$	✓			✓
$\Delta h_{FC,cool}$		✓	✓	
$i_{FC}$	✓			✓
$I_{FC}$	✓			✓
$L_{FC}$	✓			✓
$LHV_{H_2}$		✓	✓	
$\dot{m}_{FC,cool}$	✓			✓
$N_{FC,Stack,Cell}$		✓		✓
$N_{FC,Stack}$		✓	✓	
$\Delta P$	✓		✓	
$P_{FC,DC}$	✓			✓
$P_{FC,DC,max}$		✓		✓
$P_{Load}$	✓		✓	
$\dot{Q}_{FC}$	✓			✓
$U_{FC,Cell}$	✓			✓
$U_{FC,max}$		✓		✓
$U_{FC,min}$		✓		✓
$\dot{V}_{H_2,Rec}$	✓			✓
$\eta_{AC/DC,FC}$		✓	✓	
$\eta_{FC}$	✓			✓



## 5.4 Hydrogen Storage

The subsystem hydrogen storage merges the two output variables  $\dot{V}_{H_2,Store}$  and  $\dot{V}_{H_2,Rec}$  in order to calculate the necessary tank size and to check sufficient hydrogen availability when hydrogen reconversion is active. Additionally, an external hydrogen consumer can be considered here if hydrogen is needed as fuel for vehicles or cooking. However, this model neglects an external hydrogen consumer due to the intention of a compact unit design and the requirement of additional equipment (e.g. compressors, piping) for the mentioned hydrogen applications. As a result, the hydrogen flow  $\dot{V}_{Tank}$  in or respectively out of the hydrogen storage tank can be calculated by subtraction of the hydrogen generated with the needed hydrogen for reconversion leading to Equation (5.45). It needs to be mentioned that the hydrogen for reconversion  $\dot{V}_{H_2,Rec}$  is the sum of the hydrogen needed by the fuel cell to cover the electrical load of the consumers as well as all auxiliary equipment necessary. On top of this for operating the fuel cell during absence of renewable energy, additional hydrogen  $\dot{V}_{H_2,FC,cool}$  for powering the cooling unit of the fuel cell is necessary and modeled in Section 5.6 by Equation (5.54).

$$\dot{V}_{Tank}(t) = \dot{V}_{H_2,Store}(t) - (\dot{V}_{H_2,Rec}(t) + \dot{V}_{H_2,FC,cool}(t)) \quad (5.45)$$

The hydrogen stored  $V_{Tank}$  within a time period  $t$  is calculated according to Equation (5.46) and considering the stored hydrogen  $V(t_0)_{Tank}$  at start. The tank volume  $V_{Tank,0}$  is determined by addition of the maximum value and the absolute minimum value of  $V_{Tank}$  according to Equation (5.47). By varying the maximum storage pressure  $p_{Store}$ , the necessary volume for the storage of hydrogen is calculated allowing to identify the optimal storage parameters for selfHY®.

$$V_{Tank}(t) = V(t_0)_{Tank} + \int_0^t \dot{V}_{Tank}(t) dt \quad (5.46)$$

$$V_{Tank,0} = |\min[V_{Tank}(t)]| + \max[V_{Tank}(t)] \quad (5.47)$$

In case the hydrogen storage pressure  $p_{Store}$  is higher than the outlet pressure  $p_{Ely}$  of the electrolyzer, additional energy  $P_C$  for compression is required and needs to be considered in the overall energy consumption of the system. Assuming an isentropic compression with the efficiency  $\eta_{is}$  and an electrical efficiency  $\eta_{el}$  of the motor, the compression power  $P_C$  is calculated by Equation (5.48), where  $\Delta h_C$  is the difference in enthalpy at constant entropy,  $\rho_{H_2}$  the density of hydrogen and the volume flow  $\dot{V}_{H_2,Store}$ .

$$P_C(t) = \dot{V}_{H_2,Store}(t) \cdot \rho_{H_2} \cdot \frac{\Delta h_C}{\eta_{is} \cdot \eta_{el}} \quad (5.48)$$

The compression of hydrogen occurs simultaneously to the hydrogen generation and the power for compression  $P_C$  needs to be added to the power of water treatment  $P_{WT}$ , electrolysis  $P_{Ely,AC}$  and hydrogen purification  $P_{HP}$  in order to account for all the energy

consumption in the system while hydrogen is generated. If the hydrogen pressure at the outlet of the electrolyzer is equal to the storage pressure, the power  $P_C$  for hydrogen compression can be neglected. The summary of the necessary variables and parameters to model the hydrogen storage is shown in Table 5.7.

**Table 5.7:** In- and outputs of hydrogen storage model

	Variable	Parameter	Input	Output
	$\Delta h_C$	✓	✓	
	$p_{Ely}$	✓	✓	
	$p_{Store}$	✓	✓	
	$P_C$	✓		✓
	$\dot{V}_{H_2,FC,cool}$	✓		✓
	$\dot{V}_{H_2,Rec}$	✓	✓	
	$V_{H_2,Store}$	✓	✓	
	$V(t_0)_{Tank}$	✓	✓	
	$V_{Tank}$	✓		✓
	$V_{Tank,0}$	✓		✓
	$\eta_{is}$	✓	✓	
	$\eta_{el}$	✓	✓	
	$\rho_{H_2,st}$	✓	✓	

## 5.5 Battery

The modeling of the battery intends to estimate the energy storage capacity  $E_{Bat}$  required for storing energy when renewable energy is available, but lies below the minimum operating threshold  $P_{Ely,DC,min}$  of hydrogen generation. At these times the power supply to the battery  $P_{Bat,AC}$  equals to the charging power  $P_{Bat,Charge}$  of the battery and is assumed equal to the surplus power  $\Delta P$  supplied by the renewable energy source. On the other hand, the stored electrical energy is used to cover a fraction of the needed reconversion energy in order to increase efficiency of the process. It is assumed that the battery is discharged when hydrogen reconversion is active at a discharge power  $P_{Bat,Dis}$ , which in this operating mode is equal to the power  $P_{Bat,AC}$ . Moreover, a linear scaling of the available energy  $\Delta P$  by the factor  $f_{Bat}$  defines the discharge power  $P_{Bat,Dis}$  (see Equation (5.49)). The smaller the absolute value of  $f_{Bat}$ , the smaller the amount of energy from the battery used in the reconversion and vice versa.

$$P_{Bat,Dis}(t) = -f_{Bat} \cdot \Delta P(t) \quad (5.49)$$

By merging the power for charging  $P_{Bat,Charge}$  and discharging  $P_{Bat,Dis}$  of the battery, the ideal state of charge  $E_{SOC,id}$  can be calculated according to Equation (5.50).

$$E_{SOC,id}(t) = \int_0^t P_{Bat,Charge}(t) - P_{Bat,Dis}(t) dt \quad (5.50)$$

In analogy to the calculation of the volume for the hydrogen storage tank, the energy storage capacity  $E_{Bat,id}$  of the battery is calculated by Equation (5.51) using the absolute minimum and the maximum value of the ideal state of charge  $E_{SOC,id}$ :

$$E_{Bat,id} = |\min[E_{SOC,id}(t)]| + \max[E_{SOC,id}(t)]. \quad (5.51)$$

It needs to be considered that the ideal energy storage capacity  $E_{Bat,id}$  does not take into account any specific design requirements to achieve acceptable degradation rates and sufficient dynamics of the battery. Furthermore, no losses due to self-discharge of the battery are assumed here. However, to account for the energy storage losses in a battery and the requirements for sizing the storage capacity  $E_{Bat}$  to keep degradation rates acceptable, the term of battery efficiency  $\eta_{Bat}$  is introduced as shown in Equation (5.52).

$$E_{Bat} = s_{Bat} \cdot \frac{E_{Bat,id}}{\eta_{Bat}} \quad (5.52)$$

Besides the use of the battery for efficiency reasons as previously described, additional functions such as supply of energy for start-up of the fuel cell and coverage of peak loads need to be included in the overall battery modeling. In this work a scaling factor  $s_{Bat}$  is used to include these additional energy demands, which need to be covered by the

battery. It is assumed that the energy is provided by the fuel cell without any conversion losses and that the charge and discharge rate can be met at all times.

This modeling of the battery system shall provide a first approximation on the scale of the battery size for integration into the container. Once the system is in an advanced engineering design phase a more detailed analysis illuminating the optimal hybrid operation of fuel cell and battery is necessary. For the modeling of the battery the variables and parameters in Table 5.8 are used.

**Table 5.8:** In- and outputs of battery model

	Variable	Parameter	Input	Output
$E_{Bat}$		✓		✓
$E_{Bat,id}$		✓		✓
$E_{SOC,id}$	✓			✓
$f_{Bat}$		✓	✓	
$P_{Bat,AC}$	✓			✓
$P_{Bat,Charge}$	✓			✓
$P_{Bat,Dis}$	✓			✓
$P_{Ely,DC,min}$		✓		✓
$\Delta P$	✓		✓	
$s_{Bat}$		✓	✓	
$\eta_{Bat}$		✓	✓	

## 5.6 Photovoltaic Power Plant

Previously it was assumed that the power  $P_{PV,AC}$  from the PV plant equals to power of electrolysis  $P_{Ely,AC}$  and is only used for load coverage and electrolysis during hydrogen generation according to the relation shown in Equation (5.1). Energy demand by auxiliary equipment such as water treatment or hydrogen purification was calculated, but not incorporated in the total energy supply  $P_{PV,DC}$  by the PV plant. For this reason, all energy demand from auxiliary equipment and the conversion efficiency  $\eta_{DCAC}$  of the DC/AC converter are considered as defined in Equation (5.53) for hydrogen generation.

$$P_{PV,DC}(t) = \frac{P_{WT}(t) + P_{Ely,AC}(t) + P_{HP}(t) + P_C(t) + P_{FC,cool}(t) + P_{Ely,cool}(t)}{\eta_{DCAC}} \quad (5.53)$$

The power  $P_{WT}$  for water treatment,  $P_{Ely,AC}$  for electrolysis,  $P_{HP}$  for hydrogen purification and  $P_C$  for hydrogen compression are calculated as described in Equation (5.18), (5.1), (5.34) and (5.48).

Additionally, the electrical energy demand  $P_{Ely,cool}$  for cooling of deionized water for electrolysis and the energy demand for fuel cell cooling  $P_{FC,cool}$  need to be added for the estimation of the overall energy demand of selfHY<sup>®</sup>. It needs to be differed between the two cooling cycles due to their different operating times. While renewable energy is available, hydrogen is generated, therefore the additional energy can be compensated by increasing the installed capacity of the photovoltaic power plant. On the other side, the electrical energy required for cooling of the fuel cell needs to be supplied when no renewable energy is available by obtaining the energy from the fuel cell or the battery. As a result, an increased hydrogen generation is needed to provide enough hydrogen to ensure sufficient energy for running the cooling unit.

By using the efficiency  $\eta_{FC}$  of the fuel cell, the cooling duty  $\dot{Q}_{FC}$ , an electrical efficiency factor  $f_{FC,cool}$  of the cooling unit and the  $LHV_{H_2}$  of hydrogen, the additional hydrogen  $\dot{V}_{H_2,FC,cool}$  for running the cooling unit of the fuel cell system is determined as shown in Equation (5.54). The electrical efficiency factor  $f_{FC,cool}$  describes the ratio of electrical power for the cooler unit in relation to the necessary cooling duty.

$$\dot{V}_{H_2,FC,cool}(t) = \frac{P_{FC,cool}(t)}{LHV_{H_2} \cdot \eta_{FC}(t)} = \frac{\dot{Q}_{FC}(t) \cdot f_{FC,cool}}{LHV_{H_2} \cdot \eta_{FC}(t)} \quad (5.54)$$

The hydrogen needed for cooling  $\dot{V}_{H_2,FC,cool}$  is added to the hydrogen demand for load coverage resulting in the total amount needed for hydrogen reversion, which is considered in the tank size modeling as shown in Section 5.4 and Equation (5.45). The energy  $P_{Ely,cool}$  for cooling the electrolysis is modeled using an efficiency factor  $f_{Ely,cool}$  to account for losses of the cooling process. As shown in Equation (5.55) the efficiency

factor  $f_{Ely,cool}$  is multiplied with the cooling duty  $\dot{Q}_{Ely}$  of electrolysis resulting in the power demand  $P_{Ely,cool}$  of the electrolyzer cooling unit.

$$P_{Ely,cool}(t) = \dot{Q}_{Ely}(t) \cdot f_{Ely,cool} \quad (5.55)$$

In order to estimate the installed capacity  $P_{PV}$  of the photovoltaic power plant as specified in the previous modeling, the power  $P_{PV,DC}$  is utilized. By using the hourly capacity factor  $c_{PV}$  for a chosen location according to PFENNINGER & STAFFELL 2016, the installed photovoltaic power  $P_{PV}$  is defined as the maximum value of Equation (5.56) over the analyzed time period.

$$P_{PV} = \max\left[\frac{P_{PV,DC}(t)}{c_{PV}(t)}\right] \quad (5.56)$$

The capacity factors used in the model depend on the data set provided, the reference year, the system loss, the availability of tracking of the PV modules as well as the tilt and azimuth angle of the installation. Once the power of the photovoltaic power plant is defined, the corresponding installation area  $A_{PV}$  is of interest. It is calculated as depicted in Equation (5.57) by choosing a specific solar panel with corresponding panel area  $A_{Panel}$  and power  $P_{Panel}$ . Moreover, an area safety factor  $s_{PV}$  is added for consideration of mounting assemblies for the solar panels and auxiliary equipment needed for the photovoltaic power plant.

$$A_{PV} = s_{PV} \cdot \frac{P_{PV}}{P_{Panel}} \cdot A_{Panel} \quad (5.57)$$

All variables and parameters used in the modeling of the PV plant are shown in Table 5.9.

**Table 5.9:** In- and outputs of PV plant model

	Variable	Parameter	Input	Output
$A_{Panel}$		✓	✓	
$A_{PV}$		✓		✓
$c_{PV}$	✓		✓	
$f_{Ely,cool}$		✓	✓	
$f_{FC,cool}$		✓	✓	
$P_C$	✓		✓	
$P_{Ely,AC}$	✓		✓	
$P_{Ely,cool}$	✓			✓
$P_{FC,cool}$	✓			✓
$P_{HP}$	✓		✓	
$P_{Panel}$		✓	✓	
$P_{PV}$		✓		✓
$P_{PV,DC}$	✓			✓
$P_{WT}$	✓		✓	
$\dot{Q}_{Ely}$	✓		✓	
$\dot{Q}_{FC}$	✓		✓	
$s_{PV}$		✓	✓	
$\dot{V}_{H_2,FC,cool}$	✓			✓
$\eta_{DCAC}$		✓	✓	





## 6 Simulation and Results

In this chapter the simulation and results based on the modeling approach from Chapter 5 and measured electrical load data from an exemplary household in Sub-Saharan Africa are presented. First, the location and circumstances of the regarded location are described following a detailed analysis of the electrical consumers of the household. Using the hourly electrical load of the household in the year 2020, the simulation is performed and the results are rendered. The parameter values used in the simulation are summarized in Appendix B.

Based on these results, the system is scaled to fit in a standardized 20 foot container considering all relevant equipment, pipes, connections, valves and instrumentation. Moreover, a detailed process flow diagram (PFD), a single line diagram (SLD) and a 3D-model of the unit are prepared including a parts list relevant for the economic assessment in Chapter 8. The data for the electrical load  $P_{Load}$  was measured in the year 2020 in a household in the surrounding area of Bamako, the capital of Mali. In this two floor building seven residents are housing using the electrical devices with the corresponding power as shown in Table 6.1.

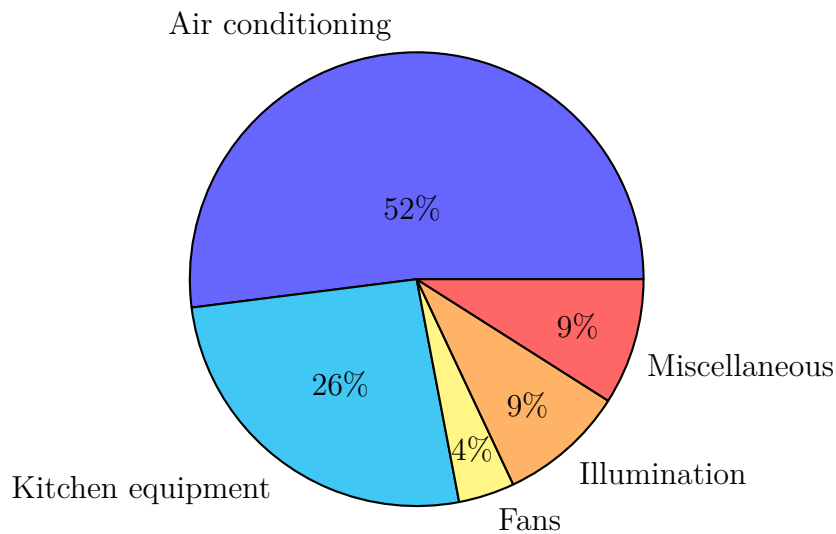


**Figure 6.1:** Shares of maximum electrical power demand in Bamako household

Furthermore, the metered overall annual power consumption by this particular household in the year 2020 was 11,358 kWh. The electrical consumer with the highest power demand are the air conditioning units with approximately 52% share on the overall maximum power demand followed by the kitchen equipment such as oven, stove, refrigerator, microwave and kitchen hood with a share of around 26%. Even though the quantity of illumination devices and fans is relatively high, the contribution with regards to power demand is with a share of 13% rather small. At last, the miscellaneous electrical consumers such as TV, decoder and pumps account for 9% of the maximum power demand as depicted in Figure 6.1.

**Table 6.1:** List of electrical devices of household in Bamako used in simulation

Location	Device	Quantity	Power in kW
Roof	Pump	1	0.37
	Air conditioning	5	6.7
Bedroom 1	TV	1	0.15
	TV decoder	1	0.06
	Ceiling fan	2	0.17
	Illumination	17	0.204
Hallway 1	Illumination	10	0.166
Bedroom 2	Ceiling fan	3	0.255
	Illumination	6	0.144
Living room 1	TV	1	0.22
	Ceiling fan	2	0.1
	Illumination	11	0.084
Balcony	Illumination	2	0.064
Living room 2	TV	1	0.219
	Ceiling fan	2	0.1
	Illumination	48	0.528
	Air conditioning	2	2.5
Kitchen	Equipment	5	5.2
	Fan	1	0.04
	Illumination	6	0.079
Storage	Ceiling fan	1	0.085
	Illumination	1	0.024
Detached house	Ceiling fan	1	0.085
	Illumination	2	0.048
	Air conditioning	1	1.2
Garage	Illumination	7	0.1685
Courtyard	Illumination	9	0.235
	Water pump	1	0.75
			19.95

It needs to be considered that the shares shown in Figure 6.1 are related to the maximum power consumption of the electrical consumers and do not state the share of the actual energy consumption over a given time period, which depend on the load and duration of operation. Although approximation factors can be used to estimate the energy consumption by assuming a certain load and time period of operation based on similar households and energy consumption profiles, the most accurate way is to use measured hourly energy consumption data of the household. For this reason, a logging device has been installed within the electric meter of the household gathering data on the electrical load  $P_{Load}$  of the entire household, which is used in the simulation.

As explained in the modeling in Section 5.6, the electrical power  $P_{PV,DC}$  for the simulation is determined according to PFENNINGER & STAFFELL 2016 using the year 2019 as reference and the data set of MERRA-2, which provides global solar irradiation data. Moreover, the installed capacity of 10 kW is assumed, a system loss of 10 % with no tracking of the solar panels and a tilt angle of 18° from the horizontal with southward facing. For the analyzed location an average capacity factor of 19 % is determined with the highest value in February of approximately 22 % and the lowest in August with around 15 %. The capacity factor is the ratio of the power output of a photovoltaic power plant to the maximum possible power generated over a given period of time. Photovoltaic power plants at sites with capacity factors of around 20 % can be considered as a reasonable option for energy supply.

However, by installing PV modules with tracking, the power generation can be increased leading to higher capacity factors. For an off-grid system such as selfHY<sup>®</sup>, a simple design with as few movable parts as possible is needed, therefore a lower capacity factor, but simpler system design is an acceptable compromise.

Using the iterative process described in Section 5.1, the renewable power  $P_{PV,DC}$  is adjusted to lead to the most compact system design while ensuring sufficient hydrogen generation for meeting the electrical load  $P_{Load}$  at all times. In Figure 6.2 the trend of both variables over one year is shown, where  $P_{Load}$  varies from 0.1 kW up to around 1.4 kW and  $P_{PV,DC}$  from 0 kW at times with no renewable energy up to 4.5 kW at the beginning of March. The renewable power  $P_{PV,DC}$  drops from its peak in March until June before it keeps increasing again until December. This results in an installed photovoltaic power plant capacity  $P_{PV}$  of approximately 6 kW.

Looking at the system into more detail the hydrogen generation as well as the reconversion are crucial for the determination of the electrolyzer and fuel cell size. In Figure 6.3 the trend of the power used for hydrogen generation  $P_{Ely,DC}$  and the reconversion power  $P_{FC,AC}$  supplied by the fuel cell are depicted. As suspected, the electrolysis is active while renewable energy is present and requires a maximum of around 3.8 kW of electrical power, whereas the fuel cell is required to provide a maximum power of around 1.5 kW.

Furthermore, the important parameters for hydrogen generation and reconversion are the average power consumption and supply at times when the respective units are active. For the electrolysis the average power consumption is around 2 kW while the

generated power by the fuel cell is in average circa 0.43 kW. It can be concluded, that the largest fraction of energy provided by the renewable energy source is contributed to the electrolysis with 76 % of the available power  $P_{PV,DC}$  used. The difference between the maximum load  $P_{Load,max}$  of around 1.4 kW and the maximum power  $P_{FC,AC,max}$  of 1.5 kW is due to the additional energy needed for the cooling of the fuel cell, which needs to be supplied by the fuel cell itself due to unavailability of renewable energy during hydrogen reconversion.

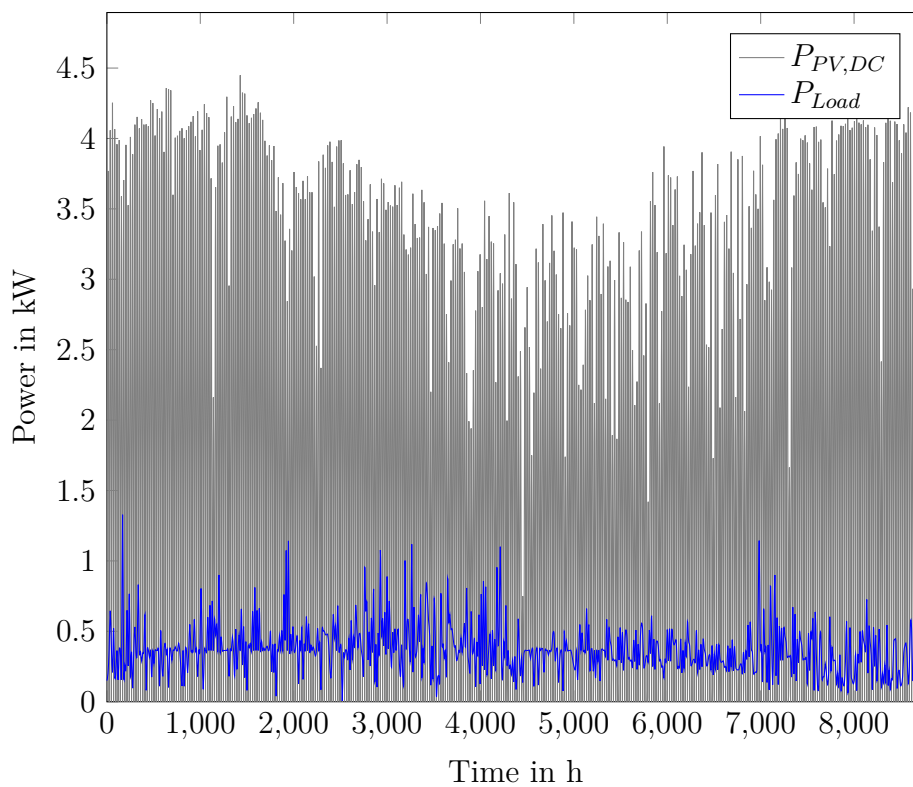


**Figure 6.2:** Renewable power  $P_{PV,DC}$  and electrical load  $P_{Load}$  over one year

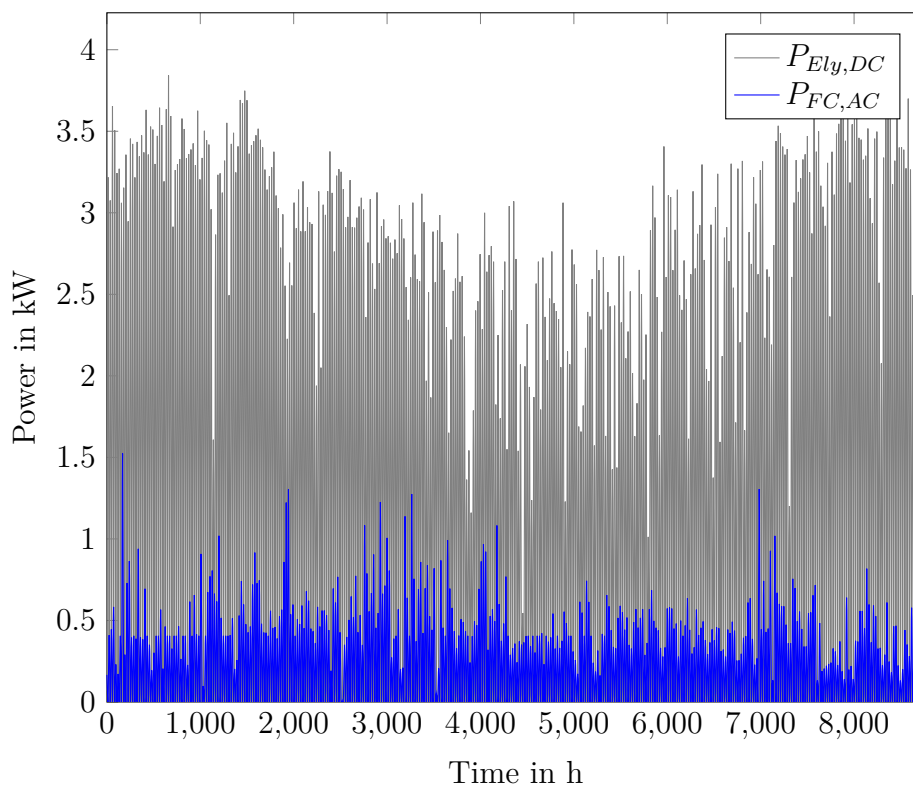


**Figure 6.3:** Electrical power  $P_{Ely,DC}$  for electrolysis and reconversion power  $P_{FC,AC}$  of fuel cell over one year

Depending on the hydrogen generation and consumption, the required volume for storage is changing. Assuming the hydrogen is stored at a maximum pressure of  $p_{H_2,Store} = 60$  bar and constant temperature  $T_{H_2,Store} = 20$  °C, the corresponding volume is determined using hydrogen properties according to LEMMON ET AL. 2018 and results in the trend visualized in Figure 6.4. It can be clearly identified that the most critical situation with regards to availability of hydrogen for reconversion is around the 6000<sup>th</sup> operating hour. This is due to the fact that from the 1817<sup>th</sup> operating hour, hydrogen, which has been generated until that point, is mainly consumed by the fuel cell from this point on. In August the necessary hydrogen storage volume is the lowest, which indicates the favored time of the year for installation and start-up of selfHY<sup>®</sup> due to the expected high hydrogen generation in the upcoming months.

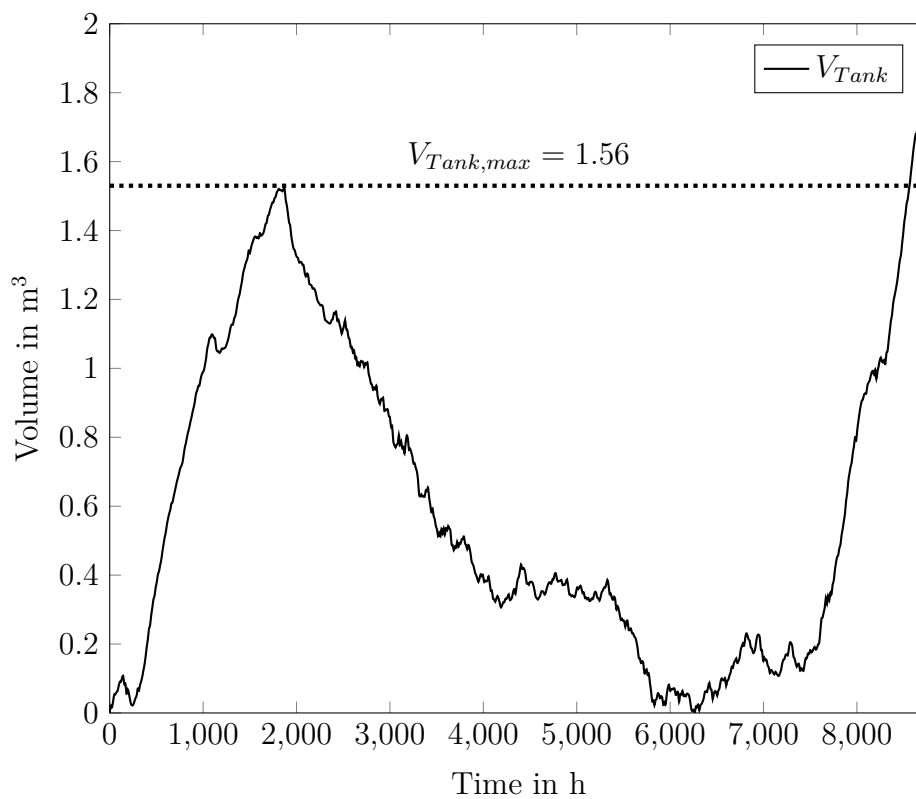


**Figure 6.4:** Volume  $V_{Tank}$  required for storage at  $p_{H_2,Store} = 60$  bar and  $T_{H_2,Store} = 20$  °C at present hydrogen generation and reconversion

From August onward the hydrogen generation predominates resulting in a steep increase of the needed storage volume. By the end of the analyzed time period the highest storage volume  $V_{Tank} = 1.92$  m<sup>3</sup> is observed. In order to keep the system design compact and as storage is the most spatial consuming subsystem, it is of vital importance to reduce the storage volume if possible and at the same time ensure sufficient hydrogen availability. For this reason, it is possible to ease the hydrogen generation and keep the storage volume at the second highest peak value of  $V_{Tank} = 1.56$  m<sup>3</sup>, which is reached at the 1817<sup>th</sup> operating hour. Consequently, the hydrogen generation needs to be adjusted by the control system of the unit to not exceed the storage volume of  $V_{Tank} = 1.56$  m<sup>3</sup> in the last 2000 operating hours. In the end, the hydrogen storage tank is filled up fully

at the start of the new year, which allows more flexibility and makes security of energy supply more certain.

For hydrogen generation and reconversion, a considerable amount of energy is converted to heat. Therefore, a cooling system is required in both cases to maintain the desired operating temperatures while considering additional space requirements for it. The concept for installation of the needed cooling system is that for transportation to the installation site the units are affixed in the container. At site the cooling units are taken out and mounted on top of the container due to favorable conditions for heat dissipation and resulting spatial advantages in the container interior.

Water is assumed as cooling medium in the simulation even though for hydrogen reconversion a water-glycol mixture is used. The discrepancies between water and actual cooling mediums used in the process are neglected due to very similar heat transfer properties. Moreover, no freezing issues are expected in the system owing to the climate with temperatures above 10° C over the entire year [HARRIS ET AL. 2020].

The heat dissipation of hydrogen generation and reconversion depends mainly on the efficiency of the electrolyzer and fuel cell and is depicted in Figure 6.5 and 6.6. Depending on the load of the electrolyzer, the heat  $\dot{Q}_{Ely}$  generated and therefore the necessary mass flow  $\dot{m}_{Ely,cool}$  for cooling of the process is determined. In the simulation the operating temperature of the electrolyzer of  $T_{Ely} = 70\text{ }^{\circ}\text{C}$  is specified which is equal to the inlet water temperature. A constant temperature difference of the inlet and outlet water temperature of 5° C requires the mass flow  $\dot{m}_{Ely,cool}$  for cooling at a pressure of  $p_{Ely,An} = 4\text{ bar}$ . By permanently adjusting a flow control valve in the deionized water circuit the temperature difference is kept constant while the mass flow  $\dot{m}_{Ely,cool}$  is varying.

In Figure 6.5 the trend of the dissipated heat by the hydrogen generation  $\dot{Q}_{Ely}$  and the mass flow  $\dot{m}_{Ely,cool}$  are shown in the course of one year. It is recognizable that the decrease in electrolyzer load is accompanied by a decrease of the heat  $\dot{Q}_{Ely}$  and mass flow  $\dot{m}_{Ely,cool}$ .

Similar to the cooling of the hydrogen generation, the hydrogen reconversion maintains a constant temperature difference across the fuel cell unit of 2° C while the operating pressure is set to  $p_{FC} = 2.5\text{ bar}$ . As depicted in Figure 6.6, the necessary mass flow required for cooling the hydrogen reconversion ranges from 0 to approximately 180  $\frac{\text{kg}}{\text{h}}$  while the cooling duty ranges from 0 to 1.5 kW with individual peaks due to high loads.

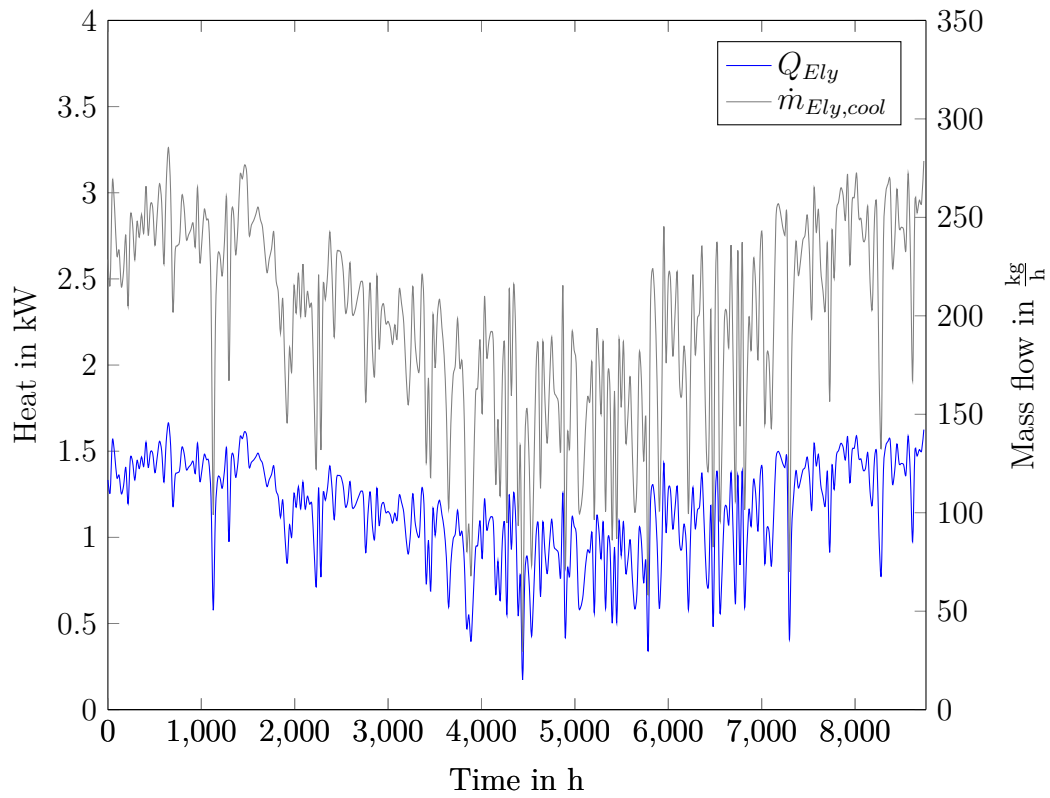


**Figure 6.5:** Heat  $Q_{Ely}$  generated through electrolysis and required mass flow  $\dot{m}_{Ely,cool}$  for cooling the electrolysis process assuming an ideal heat transfer

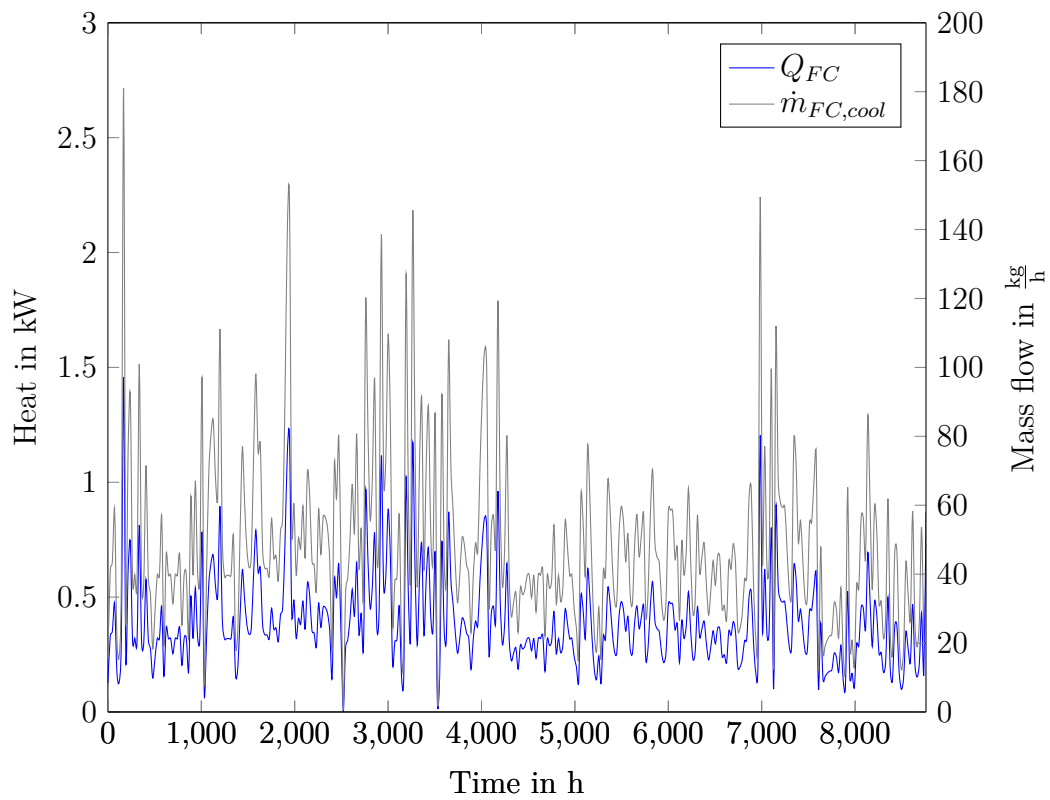


**Figure 6.6:** Heat  $Q_{FC}$  generated by fuel cell and required mass flow  $\dot{m}_{FC,cool}$  for cooling the fuel cell assuming an ideal heat transfer



As a last important simulation result, the efficiencies of hydrogen generation and reconversion are shown in Figure 6.7. It can be concluded that based on the used modeling approach, the hydrogen generation efficiency ranges from approximately 57 to almost 70 % while the hydrogen reconversion experiences a slightly worse efficiency trend ranging from around 47 to 55 %.

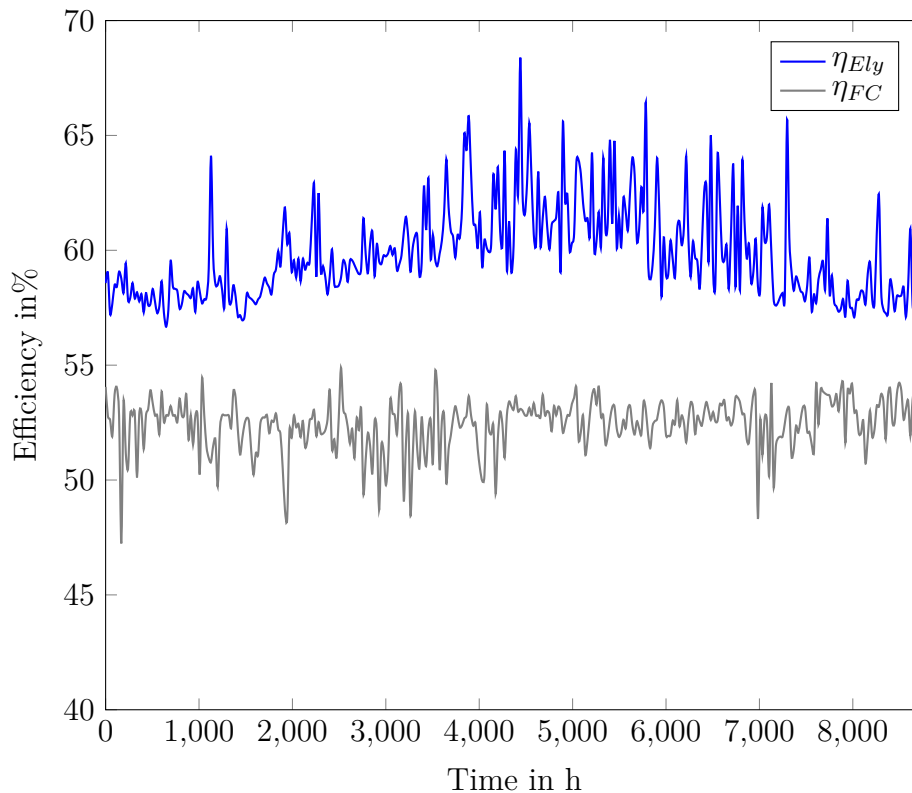


**Figure 6.7:** Electrolyzer efficiency  $\eta_{Ely}$  and hydrogen reconversion efficiency  $\eta_{FC}$  over one year

An interesting observation is that efficiency of the electrolyzer does not increase with higher capacity factors, but exhibits the best efficiency values in the summer months when the renewable power is at the lowest point during the year. The reason behind this are loss mechanisms caused by overpotential in the cells of the electrolyzer, which increase with rising operating voltage. The main losses are the activation, ohmic and mass transport losses, whose influence prevail depending on the operating voltage [MERWE ET AL. 2013]. The hydrogen reconversion or respectively the fuel cell has similar voltage loss mechanisms, which are depicted in Figure 3.26. Therefore, at higher loads with increased current the efficiency of the fuel cell tends to decrease. However, this efficiency decrease is of a much lower magnitude than that of the electrolyzer and therefore does not have a large overall effect. Based on the utilized polarization curves for electrolyzer as well as for the fuel cell the efficiency can vary significantly.

Besides the presented variables, certain parameters resulting from the simulation are important for the further approach of developing selfHY<sup>®</sup> and are therefore summarized in Table 6.2. The spatial requirements of the components are taken from commercially

available components in similar power ranges of the simulation results according to JURISIC ET AL. 2021.

**Table 6.2:** Overview of important results for further assessment of selfHY<sup>®</sup> basic design

Parameter	Description	Unit	
$P_{Ely,DC,max}$	Maximum power of electrolyzer	kW	3.8
$P_{Ely,cool}$	Maximum cooling duty for electrolyzer	kW	1.6
$P_{FC,DC,max}$	Maximum power of fuel cell	kW	1.5
$P_{FC,cool}$	Maximum cooling duty for fuel cell	kW	1.5
$V_{Tank}$	Maximum hydrogen storage	m <sup>3</sup>	1.56
$E_{Bat}$	Battery storage	kWh	2.5
$P_{PV}$	Installed power PVPP	kW	6
$A_{PV}$	Area for PVPP	m <sup>2</sup>	33

With regards to spatial requirements and integration of all needed components in a 20 foot container, the storage volume of 1.56 m<sup>3</sup> poses the biggest challenge for a compact design and is the limiting factor for the sizing of selfHY<sup>®</sup>. Of course, it is possible to arrange the hydrogen storage externally in a separate container and thereby solve potential storage issues, nevertheless for the sake of transport and easier handling during start-up and installation in a remote area, one of the most important requirements as described in Chapter 4 is to have an integrated unit with minimum or no external connections.

In a first top-level spatial assessment, the required components are identified and arranged on the footprint of a 20 foot container keeping in mind that the maximum height of each component shall not exceed 2.385 m and keeping accessibility, operability and maintainability of the components in mind. As in Figure 6.8 depicted, all main components fit on the area of a 20 foot container in defined sections and the size can even be scaled up. As mentioned before, the hydrogen storage is the component with the most critical spatial requirement and is therefore decisive for the upscaling and estimation of the maximum size of selfHY<sup>®</sup>. The spatial sections with the corresponding main components of the system as shown in Figure 6.8 are listed in Table 6.3.

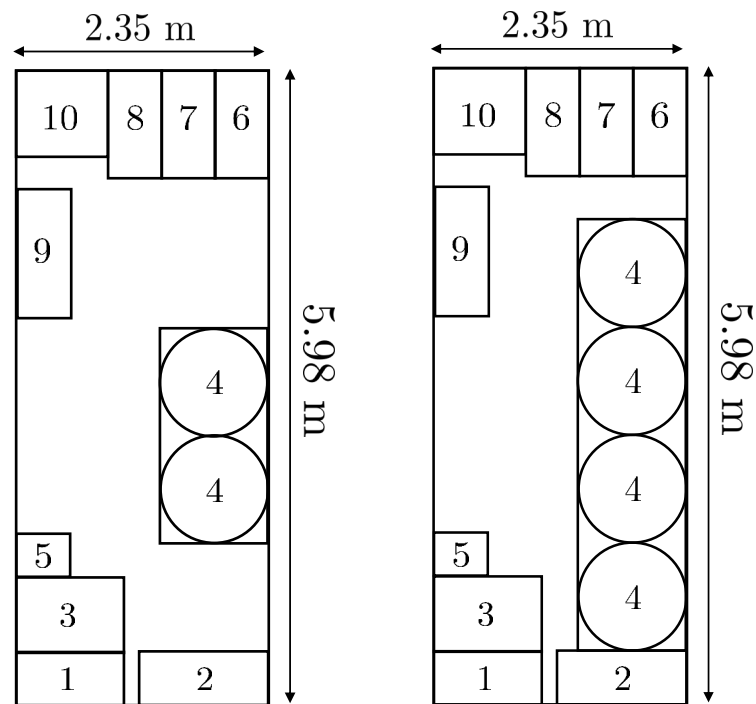


**Figure 6.8:** Spatial arrangement in process sections on 20 foot container footprint of initial (left) and scaled-up (right) size

Based on the simulation results, the hydrogen storage size can be increased by a factor of 2.1, therefore reaching a hydrogen storage volume of around  $3.4 \text{ m}^3$  while still fitting into a standardized 20 foot container (see Figure 6.8). The other components are scaled up accordingly resulting in the size requirements of selfHY<sup>®</sup> depicted in Table 6.3.

The component sizes are based on an extensive market analysis on hydrogen technology vendors and other equipment manufacturers with focus on off-the-shelf available products. Using a conservative approach, the sizes and power of components are rounded up to match suitable products on the market and ensure the design requirements given by the simulation results. Some components cannot be arranged within the container due to their functionality. In particular, the cooling systems as well as the DC/AC converter need to be placed externally. Moreover, the photovoltaic power plant is transported in an additional container with special frames for the solar panels allowing a fast and easy installation on site by unfolding the structure on tracks.

For the further assessment the results in Table 6.3 are used for the development of the basic design and the 3D-model of selfHY<sup>®</sup>, which is the focus of the following chapter.

**Table 6.3:** Spatial requirements of basic selfHY<sup>®</sup> variant

Component	L in m	W in m	H in m	Area in m <sup>2</sup>	Section
Water treatment	0.5	1	1	0.5	1
Electrolysis	0.7	1	1.5	0.7	3
H <sub>2</sub> purification	0.5	1.2	1.5	0.6	2
H <sub>2</sub> storage	4	1	2	4	4
Remineralization	0.4	0.5	1.2	0.2	5
H <sub>2</sub> reconversion	1	0.5	0.5	0.5	6
DC/AC converter PV	0.7	0.5	1	0.35	external
AC/DC converter ELY	1	0.5	1	0.5	7
DC/AC converter FC	0.5	0.3	0.6	0.15	6
Battery charger	0.4	0.3	0.6	0.18	8
Battery	0.6	0.2	0.4	0.12	8
Cooling unit FC	1.3	0.6	0.8	0.78	external
Cooling unit ELY	1.2	1	1.3	1.2	external
Nitrogen racks	1.2	0.5	1.7	0.6	9
Control cabinet	1.2	0.5	1.7	0.6	10

# 7 Basic Design

In this chapter the process and electrical design of selfHY<sup>®</sup> is described for the basic variant considering the scaled up simulation results from Table 6.2 by a factor of 2.1 and the size requirements from Table 6.3. As previously described, the simulation results from Table 6.2 are scaled up by only a factor of 2.1 due to size limitation for hydrogen storage. First, the overall process starting with water treatment, hydrogen generation, storage and reconversion as well as the cooling system are described using the process flow diagram from Appendix C.

In the subsequent section, the main electrical connections, grids and consumers are explained and outlined in the single line diagram from Appendix D. In the end, a 3D-model of the basic selfHY<sup>®</sup> variant is rendered. The results from this chapter are used to generate an overall equipment list in order to assess the economic feasibility of different selfHY<sup>®</sup> variants.

## 7.1 Process

As shown in the block flow diagram in Figure 4.3, the two input streams to generate hydrogen via electrolysis are demineralized water and electricity from renewable energy. The electrical design for the renewable power plant can be assumed very similar among all possible installation sites, whereas the water quality can vary extremely with different locations leading to deviant process designs for the water treatment unit. For the present configuration, the feed water quality is assumed to be ground water according to the main parameters defined in Table 7.1. Additionally, standards are listed which describe the commonly used procedures for determining the values of conductivity, hardness, pH-value and total dissolved solids (TDS).

**Table 7.1:** Feed water specification for water treatment process design

Parameter	Unit	Range	Standard
Conductivity	$\frac{\mu\text{S}}{\text{cm}}$	< 700	EN 27888
Hardness	$\frac{\text{mval}}{\text{l}}$	< 20	ISO/TS 15923-2
pH-value	-	7 - 8	ISO 10523
TDS	$\frac{\text{mg}}{\text{l}}$	< 1000	EN 12880

As depicted in Appendix C and Figure 7.1, the feed water is taken into the process from a reservoir by a circulation pump. In case selfHY<sup>®</sup> can be connected directly to a water distribution pipeline, the supply pressure might be sufficient for water intake and to overcome the pressure losses in the basket strainer. As a result, the circulation pump can be removed from the water treatment unit in order to save costs. The basket strainer is needed in order to prevent an intake of larger particles or parts in the system

causing damage to the downstream equipment. The differential pressure transmitter PDT-WT1 monitors constantly the pressure difference between inlet and outlet of the strainer in order to determine clogging of the strainer and necessary cleaning or exchange.

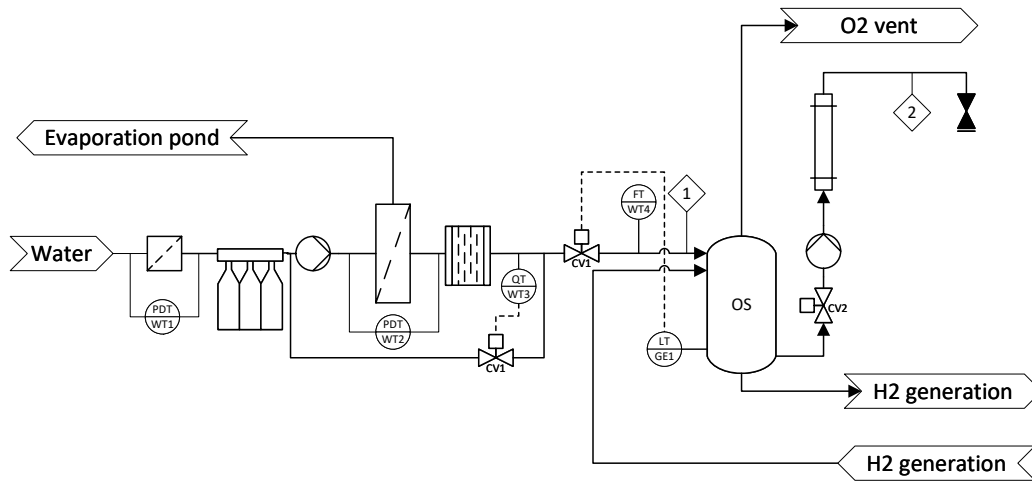


**Figure 7.1:** Process flow diagram of water treatment excluding the remineralization unit

The next process step of the water treatment is the adjustment of the pH-value in order to condition the water optimally for the water softening where the hardness of water is reduced. The main ions removed in the water softening are calcium and magnesium where a certain pH-value range is required for the reaction to occur efficiently [CRITTENDEN ET AL. 2012]. Both process steps of pH-value adjustment and water softening use additives, such as phosphoric or hydrochloric acid for decreasing the pH-value or sodium chloride for regenerating the columns of the water softening unit [LAASCH & LAASCH 2013]. The additives are filled up during maintenance in regular intervals, which are defined depending on the additive demand. The core component of the water treatment system is the reverse osmosis unit where the reverse osmosis pump increases pressure in front of the semipermeable membranes in order to filter particles and ions according to the principles explained in Subsection 3.2.1. The differential pressure transmitter PDT-WT2 monitors the pressure difference from the inlet and outlet of the reverse osmosis module and determines thereby the necessity of cleaning or exchange.

An additional electrodeionization unit removes the residual ions in the water so that very low electrical conductivity of around  $0.1 \frac{\mu\text{S}}{\text{cm}}$  is achieved. The brine water formed in the regeneration process of the water softening unit, the brine from the reverse osmosis unit as well as from the electrodeionization is introduced in an evaporation pond or in some cases in intermediate bulk containers (IBC) suitable for brine. Evaporation ponds have the advantage that no post-treatment of the brine or disposal is necessary, which reduces operation and maintenance efforts. Intermediate bulk containers would be required for transport to a waste water disposal site, which can be a major challenge

in remote areas. For the expected annual waste water of around  $1 \text{ m}^3$ , which is caused by the hydrogen production demand, both options are feasible.

Downstream the electrodeionization, the quality of the demineralized water is checked by the transmitter QT-WT3 before flowing as stream 1 into the oxygen separator of the hydrogen generation part of the unit. If the electrical conductivity is not satisfying and therefore higher than  $0.1 \frac{\mu\text{S}}{\text{cm}}$ , the control valve CV1 is closed and the demineralized water is recycled to the inlet of the reverse osmosis pump for repeated purification. The recycle line can also be used to keep the water treatment unit at constant operation as frequent stops and start-ups might have negative effects on the life expectancy of the water treatment unit.

In addition to the water treatment for hydrogen generation, a remineralization unit for production of potable water is connected to the oxygen separator as shown in Figure 7.1. From there, demineralized water is taken and remineralized depending on the consumers demand resulting in potable water from stream 2. Due to size limitations the water treatment unit as well as the remineralization unit are designed for a maximum throughput of approximately  $100 \frac{\text{L}}{\text{h}}$ .

Aside from the demineralized water consumption by the remineralization process, a smaller fraction of the demineralized water is used in the electrolysis process (see Figure 7.2) where the demineralized water is split into hydrogen and oxygen. In order to maintain a constant operating temperature of the endothermic reaction, the recirculated demineralized water from stream 3 is directly cooled by an air cooler, which is located externally on the top of the container. At rated operation of the  $10 \text{ kW}$  electrolyzer with an efficiency of  $60\%$  to the LHV of hydrogen, a volume flow of approximately  $0.6 \frac{\text{m}^3}{\text{h}}$  is needed for cooling demineralized water from the outlet temperature of  $75^\circ\text{C}$  to the operating temperature of  $70^\circ\text{C}$ . A flow-controlled recirculation pump adjusts the steady flow to the electrolyzer depending on its operating point.

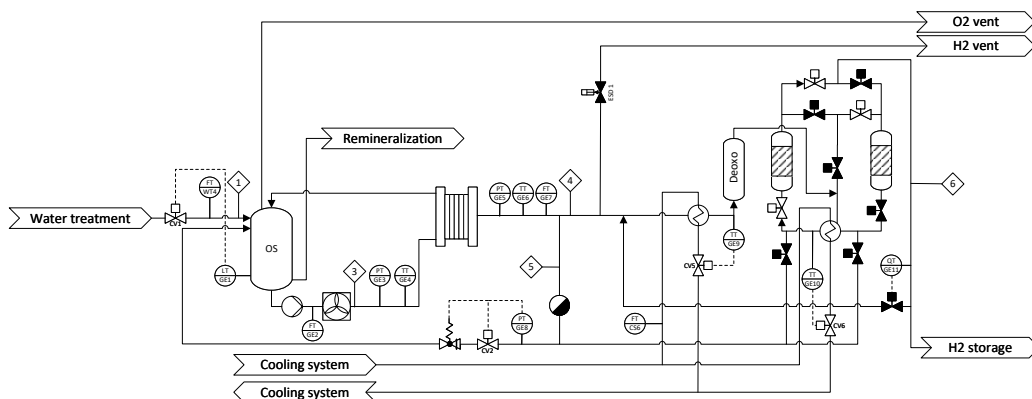


**Figure 7.2:** Process flow diagram of hydrogen generation unit with electrolysis and hydrogen purification

Moreover, the level transmitter LT-GE1 monitors the demineralized water level in the oxygen separator in order to protect the recirculation pump from running dry. It is important to mention that the demineralized water recirculation loop is connected to the anode side of the electrolysis stack where oxygen is generated. The oxygen is dragged with the demineralized water flow to the atmospheric oxygen separator where the oxygen is vented to the atmosphere while the demineralized water is recycled. The maximum demineralized water consumption at rated operation of the electrolysis results to approximately  $2 \frac{\text{L}}{\text{h}}$ . On the cathode side of the electrolysis stack, hydrogen with residual water and oxygen from crossover is generated at 60 bar and depicted as stream 4 in Figure 7.2. The main water fraction from stream 5 is subsequently removed by a condensate trap and recycled to the oxygen separator. An additional control valve CV2 and a safety valve ensure that high pressure is not introduced to the atmospheric oxygen separator.

Furthermore, the hydrogen product stream is purified by a deoxidizer removing oxygen traces and adsorber columns removing last traces of water in the product stream. Once the adsorbent material of one column is fully loaded, the regeneration of this column is started and the second column starts regular operation. The residual water recovered from the regeneration process is also introduced back to the oxygen separator. In Figure 7.2 the regular adsorption operation of the left column is depicted with the corresponding valve positions. After the purification process, it is expected that traces of oxygen and water at dew point are below 2 ppmv, which is permanently monitored by the transmitter QT-GE11. If the desired quality is achieved, the hydrogen flow from stream 6 flows to the hydrogen storage, otherwise the corresponding valve opens and recycles the product stream to the inlet of the purification unit.

Once the hydrogen product stream reaches the hydrogen storage of selfHY<sup>®</sup> as depicted in Figure 7.3, the pressure in the hydrogen storage tank is monitored by the pressure transmitter PT-ST2 as well as the flow by the bidirectional flow transmitter FT-ST3. As long as the hydrogen generation is operating, the hydrogen storage is filled and the hydrogen reconversion is not active.

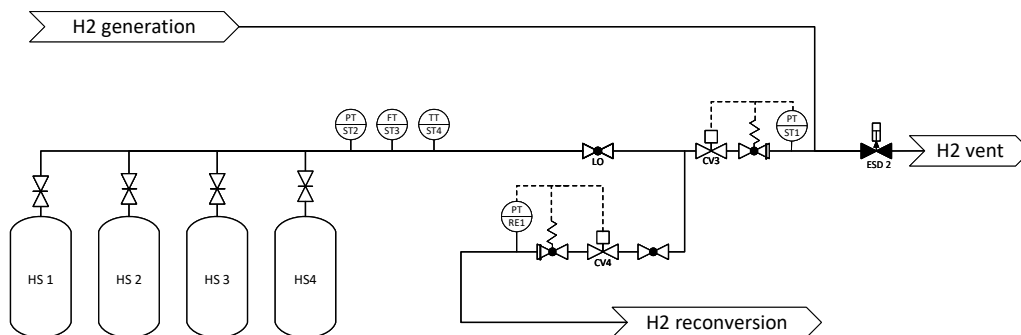


**Figure 7.3:** Process flow diagram of hydrogen storage

Depending on the operating mode, the positions of the control valves CV3 and CV4 are adjusted. As depicted in Figure 7.3 for hydrogen production, the control valve CV4



with its pressure transmitter PT-ST1 keeps the pressure on the upstream side at around 60 bar while the pressure in the four hydrogen storage tanks is gradually increasing depending on the availability of renewable energy. If hydrogen for reconversion is required, the control valve CV3 to the hydrogen generation closes fully and CV4 opens partly to adjust a constant pressure on the downstream side. Depending on the supply pressure range of the fuel cell and the current hydrogen storage pressure, the control valve CV4 adjusts the valve opening in order to maintain the desired inlet pressure for the fuel cell. An additional safety valve ensures that the pressure from the hydrogen storage, which can reach up to 60 bar during normal operation, is not introduced to the hydrogen reconversion, which operates at lower pressures of under 3 bar.

For the hydrogen reconversion as shown in Figure 7.4, an injector is used to dose the correct amount of hydrogen from stream 7 of the storage tanks to the fuel cell. It needs to be considered that not all hydrogen reacts with oxygen and therefore it is recirculated by a blower to the injector of the reconversion unit. The control system ensures the correct balance between recirculation of hydrogen and injection of new hydrogen from the storage depending on the monitored parameters such as pressure and flow. In order to supply the fuel cell with pressurized oxygen for the reaction as shown in stream 8, an air compressor with a humidifier is installed.

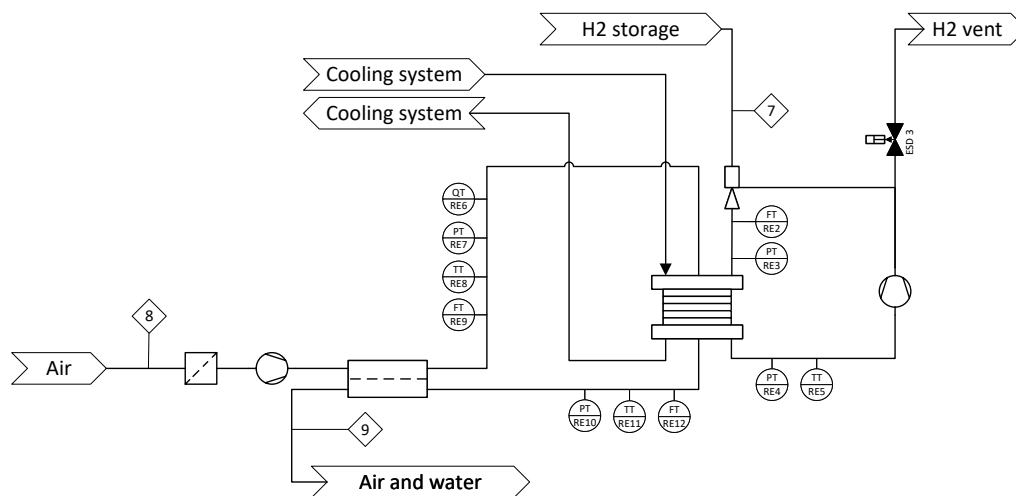


**Figure 7.4:** Process flow diagram of hydrogen reconversion

Moreover, an air filter removes larger particles, which can be harmful for the fuel cell. The oxygen of the humid air reacts with the hydrogen to water, which is routed in stream 9 to the evaporation pond at approximate maximum flow of  $3 \frac{\text{L}}{\text{h}}$  during rated operation. Part of the generated water is reused in the humidifier, which keeps the air humid and the membranes moisturized.

In this exothermic reaction, the generated heat needs to be removed from the process in order to keep the operating temperatures at a constant level. For this reason, a chiller is installed on top of the container providing cooling to the fuel cell system as well as to the hydrogen purification unit. The temperature of the cooling liquid is kept at a

constant level by adjusting the control valve CV8 in the refrigeration cycle depending on the temperature measurement by the transmitter TT-CS2.

Additional control valves CV5, CV6 and CV7 in the cooling lines of the systems ensure the fine adjustment of the correct inlet flow depending on the cooling duty of the respective unit. The entire process design with the cooling system is depicted in Appendix C and provides also more details on operating parameters and technical safety measures such as vent lines and ESD valves.

The utilities needed on site are compressed air and nitrogen. The compressed air for valve control is generated by a small air compressor mounted in a control cabinet. Moreover, nitrogen bottle racks are installed inside the container as shown later in Section 7.3 and are necessary for purging the unit in case of start-up, maintenance or longer shutdown. In the next section the electrical design with the corresponding components of the electrical system is explained in more detail using the single line diagram from Appendix D.

## 7.2 Electrical

The hydrogen generation and reconversion as well as all auxiliary electrical equipment are connected to the electrical network of selfHY<sup>®</sup>. For the power range of up to 40 kW hydrogen generation and approximately 20 kW hydrogen reconversion power, a standardized 3 phase low voltage grid at 400/230 V is implemented.

For all selfHY<sup>®</sup> variants a maximum power from renewable energy of 75 kW is expected. As shown in the single line diagram in Appendix D and Figure 7.5, the electrical consumers are the water treatment unit, the electrolysis, the hydrogen purification unit, the battery and the cooling system. When hydrogen is generated, these units are consuming electrical energy as well, which is considered in the modeling approach from Chapter 5.

As previously described in Subsection 3.2.2, the electrolysis requires direct current, which is provided by an AC/DC-converter. Moreover, a load isolator switch with fuse in the DC grid ensures protection from current peaks in the same way as for the fuel cell and battery and poses a cost-effective way compared to other switches for overcurrent protection. Similarly, the AC grid circuit breakers are used to counteract on high current and prevent damage to the connected electrical equipment whereas surge arresters protect the AC grids from voltage peaks in case of excessive current. When hydrogen is reconverted, electrical energy is provided by the fuel cell and the battery to the cooling system and the electrical consumers.

Depending on the consumer grid requirements, an AC/AC-converter is used to transform the electrical energy generated by selfHY<sup>®</sup> to the local grid requirements. For the battery a bidirectional AC/DC converter is used to manage the charging and discharging of the battery based on the surplus energy available from the 400/230 V grid. Apart from

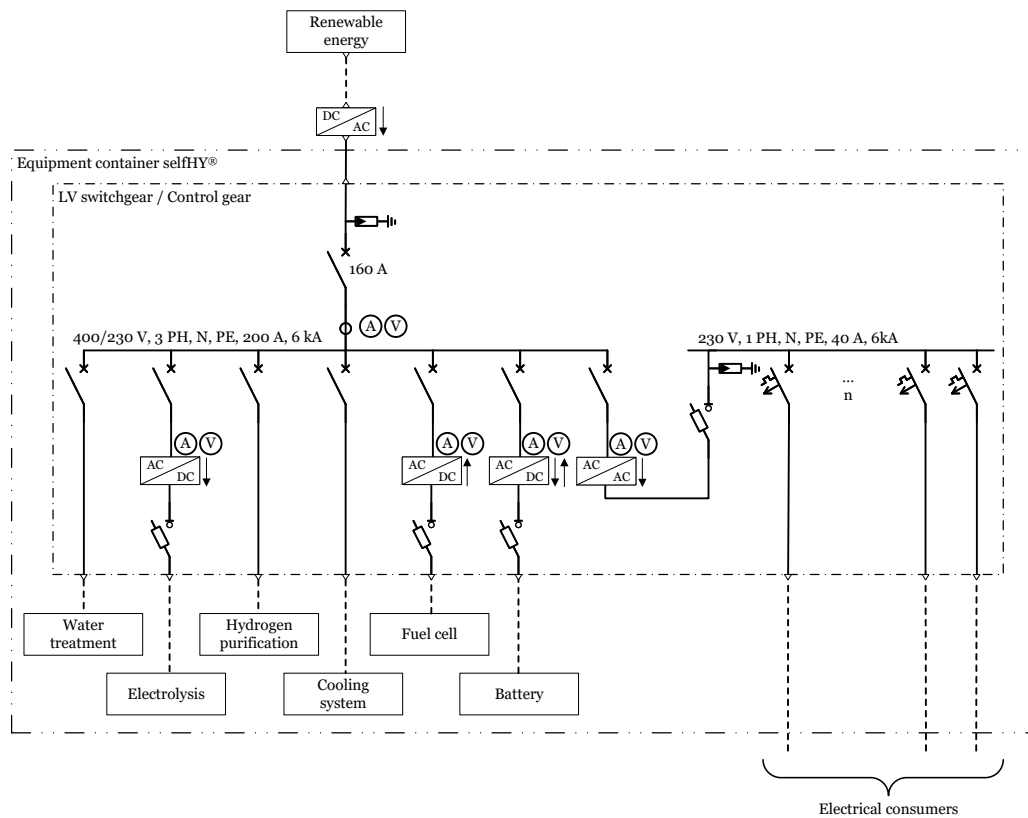


**Figure 7.5:** Single line diagram of selfHY<sup>®</sup>

this grid, additional busbars with lower voltage levels such as 24 V direct current might be necessary for operating smaller electrical consumers such as valve actuators.

In Table 7.2 the most important electrical parameters of the electrical equipment are summarized. While the electrolysis requires the highest power, the water treatment and hydrogen purification are the smaller power consumers of the hydrogen generation. Moreover, the hydrogen purification is only running at rated power during the regeneration of the columns unlike the water treatment unit and the electrolysis, which operate constantly. The cooling system and the battery are the two units, which are operating permanently independent of the operating mode. While the cooling system ensures the heat dissipation from the fuel cell and the hydrogen purification, the battery charges or discharges depending on the operating mode and power demand by consumers.

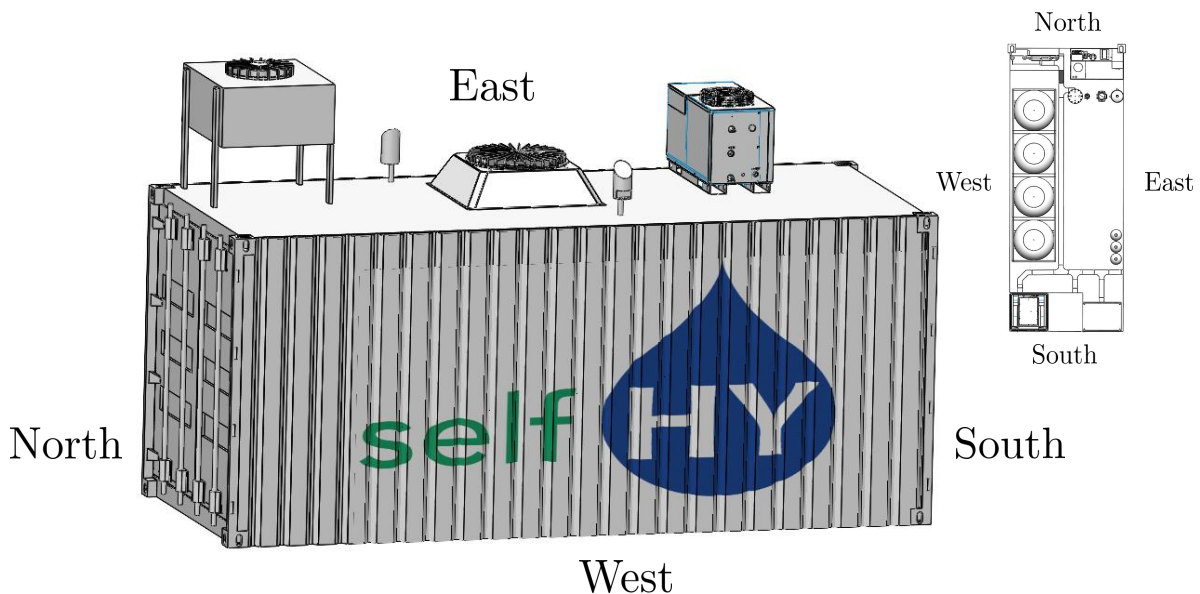
Since the basic process and electrical design as well as the general arrangement of the units (see Figure 6.8) have been assessed so far, the next section focuses on the developed 3D-model of selfHY<sup>®</sup>.

**Table 7.2:** Main electrical equipment parameters of selfHY<sup>®</sup>

Unit	Power in kW	Voltage in V	Type	Operation during
Water treatment	1	230	AC	H <sub>2</sub> generation
Electrolysis	10	28	DC	H <sub>2</sub> generation
Hydrogen purification	2	230	AC	H <sub>2</sub> generation
Cooling system	5	230	AC	permanent
Fuel cell	4	24	DC	H <sub>2</sub> reconversion
Battery	3	55	DC	permanent

### 7.3 3D-Model and Variants

For the basic version of selfHY<sup>®</sup>, the main target is to arrange all components of the system so it can fit in a standardized 20 foot container. Based on the general layout from Figure 6.8, a 3D-model is developed showing the spatial requirements and potential up-scaling opportunities of the individual components. In Figure 7.6 the external view on the 20 foot container is visualized, where the cooling and ventilation system are positioned on top of the container. It is not expected that the overall weight of the components on the roof plate exceeds 300 kg in total, taking a maximum allowable point load of  $600 \frac{\text{kg}}{\text{m}^2}$  into regard. Therefore, the structural stability of selfHY<sup>®</sup> with the installations on top can be assumed as feasible in accordance with ISO 668.

**Figure 7.6:** External view on selfHY<sup>®</sup>

Moreover, the oxygen and hydrogen vents are recognizable in Figure 7.6 and arranged in contrary venting directions from each other in order to prevent mixing of oxygen with hydrogen. In the course of further development of selfHY<sup>®</sup>, the correct height

of the vents needs to be analyzed with dispersion calculations to not only predict the mixing of hydrogen and oxygen, but also ensure that no hydrogen is taken into the units of the cooling system. During transportation all the components mounted on top of the container are disassembled and stored inside the container with respective fixation for safe transport.

The interfaces of selfHY<sup>®</sup> to external components include the electrical connection to the renewable energy power source with a low voltage grid, a connection for feed water intake to the water treatment unit and the connection to the local grid or directly to the consumers. The 20 foot container can be opened and is constructed with an additional door on the east side of the container along with the standard doors on the north and south side. The access to the indoor maintenance area is given by the door on the east side, where sufficient room for maintenance and exchange of equipment and nitrogen racks is provided as well as enough space for the transport of the cooling system units and vents.

In Figure 7.7 the maintenance area in front of the storage tank assembly is shown. On the north side of selfHY<sup>®</sup> the water treatment and demineralization unit is positioned. Next to it is the electrolyzer stack and the connected oxygen separator with the recirculation pump of the demineralized water loop. The generated hydrogen in the electrolysis is then routed to the purification unit while on the way a condensate trap removes dragged water from the hydrogen product stream. The hydrogen purification unit is positioned in the north-west corner of the unit and accessible from the maintenance area as well as from the north. Furthermore, the water treatment unit is spatially separated from the hydrogen process part by an inner wall because it has lower explosion protection standards than the area, where hydrogen is processed. The hydrogen process area which includes the electrolysis, purification, storage and fuel cell is expected to be categorized as zone 1 according to IEC EN 60079-14 and ATEX Directive 1999/92/EC, where explosive atmospheres are likely to occur occasionally during normal operation.

In general, all equipment installed in the hydrogen process area shall comply with ATEX directive 2014/34/EC according the requirements to gas group IIC. For hydrogen this results in equipment use with very low potential ignition energy of only of up to 20  $\mu\text{J}$  and a temperature class T1, which allows the maximum permissible surface temperature of up to 450 °C due to the high auto-ignition temperature of hydrogen of 560 °C. All electrical equipment in this area shall be designed in pressure tight encapsulation according to IEC EN 60079-14 with equipment protection level Gb as required for equipment in zone 1. A sufficient air exchange rate is enabled by the ventilation system installed in the center of the roof to prevent the presence of explosive atmosphere. In order to decrease potential leakage all possible connections shall be welded, if not possible it needs to be ensured that the connections are permanently technically tight according TRBS. The four hydrogen storage tanks are aligned on the west side of the container and connected with main line from the purification unit and to the fuel cell.

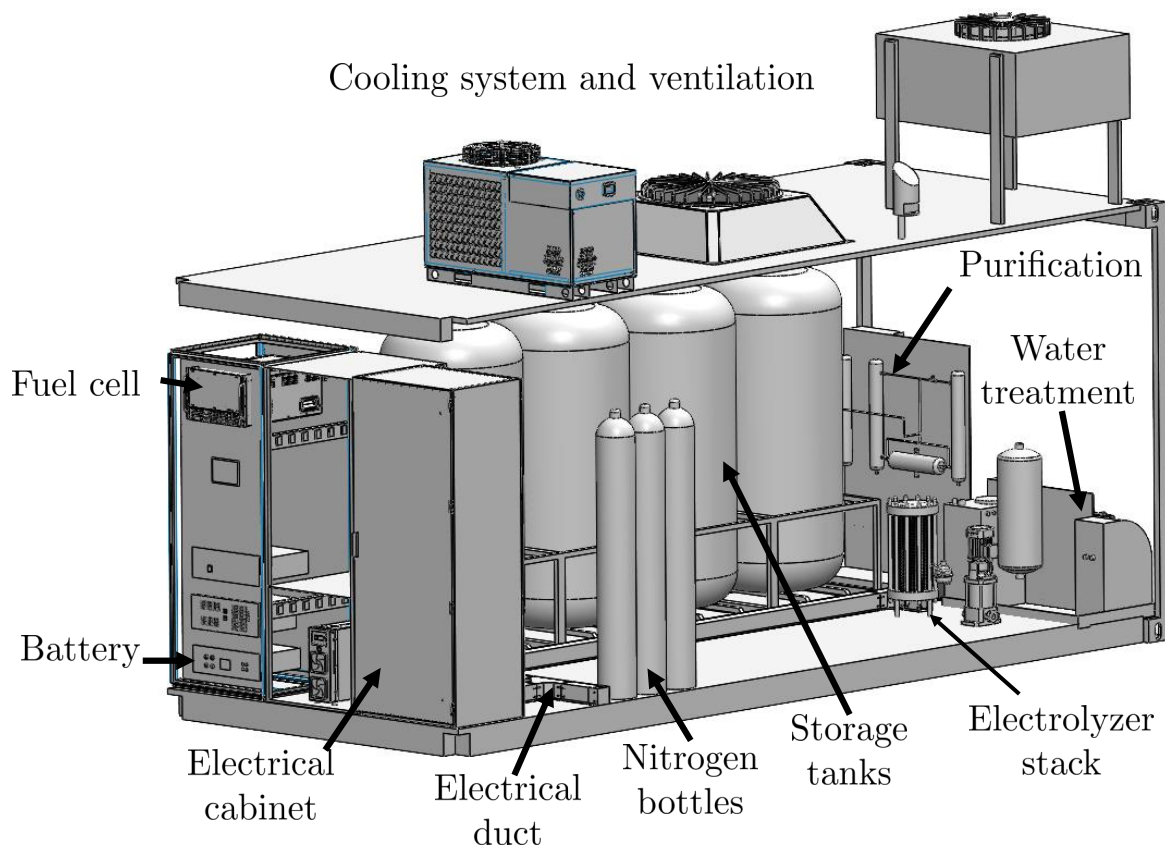


**Figure 7.7:** Internal view on selfHY®

In case of an emergency shutdown, all valves are set to fail-safe mode and the hydrogen in the main line is vented. In the south of the container the electrical cabinet with the programmable logic controller and the fuel cell are located. The fuel cell is positioned at the highest slot of the modular cabinet in order to keep hydrogen piping length to a minimum and prevent hydrogen to be induced in the bottom area of the container where many electrical equipment is installed. In the modular slot below the fuel cell, additional fuel cell units can be installed as well as the battery and converters. Between the control cabinet in the south-east corner and the south-west corner of selfHY®, additional or larger electrical equipment can be installed in case the size and power of the installed electrolyzer and fuel cell increases. Moreover, an electrical duct routes all necessary electrical connections from the external power supply by renewable energy to the electrical consumers in the hydrogen generation and auxiliaries. The electrical duct shall also provide sufficient room for the connections to the external electricity consumers. For the purging of the plant a set of nitrogen bottles at 200 to 300 bar storage pressure with a respective pressure reducer is foreseen in the east of the container.

Based on the developed 3D-model and an extensive market research on hydrogen technology equipment, the power and also the size of the electrolyzer and fuel cell can be increased up to 40 kW installed power for electrolysis and 20 kW for the fuel cell while

still fitting into a standardized 20 foot container. However, as previously mentioned, the compressed hydrogen storage is the limiting factor in order to keep all components in one 20 foot container unit. Therefore, expanded variants of selfHY<sup>®</sup> with external storage containers will be assessed for economic evaluation in Chapter 8.

In the following the features of four selfHY<sup>®</sup> variants are depicted including variant 2, which was the main subject of this chapter. The four assessed variants with their main features are summarized in Table 7.3. The initial variant 1 of selfHY<sup>®</sup> is designed to supply one large household in Bamako, Mali with energy for the entire year based on the results from Table 6.2. Due to spatial availability left in the container variant 2, the base case, was defined. It is characterized by the upscaling to maximum hydrogen storage while still fitting all relevant equipment within the 20 foot container.

**Table 7.3:** Variants of selfHY<sup>®</sup>

<b>Variant</b>	<b>1</b>	<b>2</b>	<b>3</b>	<b>4</b>
Quantity 20 foot container	2	2	2	3
Quantity 10 foot container	0	0	1	0
Electrolysis power in kW	3.8	10	25	40
Fuel cell power in kW	1.6	4	10	16
Storage volume in m <sup>3</sup>	1.6	3.4	8.5	13.6
Quantity storage tanks	2	4	10	16
Energy supply in $\frac{\text{MWh}}{\text{a}}$	11	24	60	95

Variants 3 and 4 consider an expansion of the storage to additional external containers, which only contain the same type of hydrogen storage tanks as used in the process container, where the electrolyzer and fuel cell are located. Thus, the only interface is a piping connection between the hydrogen storage tanks in the process container and the additional storage container. There is no requirement seen at this point for any electrical connections to the storage container. The additional hydrogen containers are connected back-to-back on the west side of the selfHY<sup>®</sup> process container. For this analysis, 40 foot containers have not been taken into regard due to expected difficulties for truck transport to remote areas. There is to mention that for all variants an additional 20 foot container for the photovoltaic power plant with the folded PV panel structure and an installed capacity of up to 85 kW is foreseen.

In the following chapter the defined selfHY<sup>®</sup> variants from Table 7.3 are analyzed from an economic point of view.





# 8 Economic Evaluation

The economic evaluation is based on the developed selfHY<sup>®</sup> concept design and the required process and electrical equipment determined in Chapter 7. The main target is to analyze the CAPEX and levelized cost of energy of selfHY<sup>®</sup> and put it into perspective to costs of current off-grid energy system solutions such as battery energy storage systems (BESS) or diesel generators (DG).

The four variants defined in Table 7.3 will be assessed in the following with regards to CAPEX, cost breakdown by units and levelized cost of energy considering among others operation and maintenance costs, discount factors as well as the expected operation time. In order to include possible cost variations depending on the development of hydrogen technology and the general economy, a cost sensitivity analysis is performed. The cost data base for this assessment has been generated from extensive literature review and interviews with leading hydrogen technology providers.

## 8.1 Cost Estimation for selfHY<sup>®</sup> Variants

As mentioned in Section 7.3, selfHY<sup>®</sup> can be scaled up further by adding hydrogen storage containers as defined in Table 7.3. In general, it is to be expected that the larger the hydrogen storage, the lower the overall costs for energy. Of course, from this point of view, the limitation lies in the upscaling size of the hydrogen generation and reconversion as they can only be scaled up to a certain size while still fitting into a 20 foot container. This maximum scale-up is reached with variant 4, where a further increase in system size would result in simply adding more variants as defined in Table 7.3 with no positive effect on the levelized cost of energy. For the cost estimation of selfHY<sup>®</sup>, the following equipment categories with the listed items have been identified and assessed:

- Renewable energy
  - PVPP with solar panels
  - MPPT including inverter
- Water treatment
  - Basket strainer
  - Intake pump
  - Water treatment unit (demineralized water)
  - Remineralization unit
- Hydrogen generation
  - Oxygen separator

- Circulation pump
- Electrolyzer stack (PEM)
- Condensate trap
- Purification unit
- Hydrogen storage
  - Hydrogen storage tanks
- Hydrogen reconversion
  - Fuel cell system (PEM)
- Battery (including charger)
- Auxiliary equipment
  - Chiller
  - Rectifier for electrolyzer
  - Inverter for fuel cell
  - Electrical cables and ducting
  - Piping including valves
  - Instrumentation including transmitters
  - Control cabinet and PLC
- Container

In Figure 8.1 the cost breakdown of selfHY<sup>®</sup> by categories is depicted for the base case variant 2. The main cost fractions are the hydrogen generation, storage and auxiliary equipment including coolers, converters, instrumentation, mechanical and electrical work as well as the implementation of the control system. The relatively low costs of hydrogen reconversion can be traced back to the smaller power requirements for reconversion at the evaluated site in Bamako, Mali, and the more advanced stage of fuel cell system design compared to electrolysis.

It can be recognized that the container costs also reveal a quite large fraction with 10% of the overall CAPEX, which is comparable to the four hydrogen storage tanks or the water treatment installed. With this in mind, it is desirable for selfHY<sup>®</sup> variants 3 and 4 to reduce the number and size of the containers by means of increasing storage pressure, which leads to a decrease in required storage volume. However, an increase in storage pressure also indicates a cost increase due to the use of equipment with higher pressure classes. This can have major effects on the costs of the downstream equipment from the electrolyzer such as the purification unit, storage tanks, piping and valves. The influence on these costs needs to be analyzed further once pressure differences higher than 100 bar in PEM electrolysis can be achieved while ensuring a high technology readiness as well.

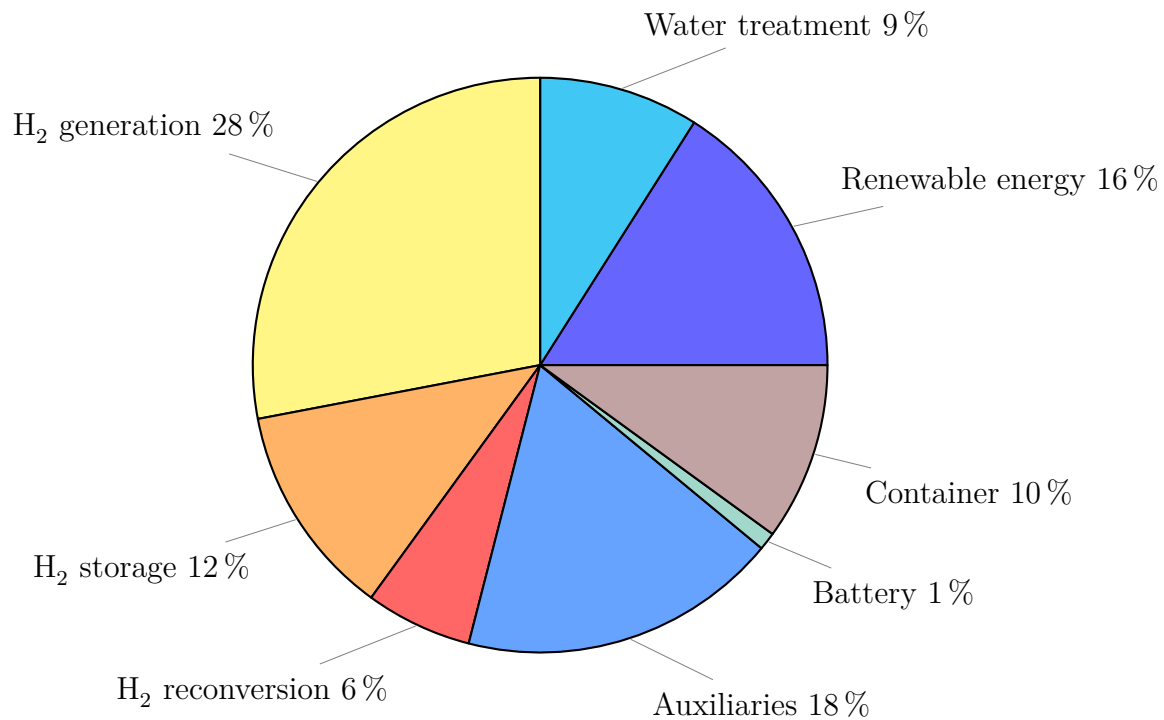


**Figure 8.1:** CAPEX breakdown of selfHY<sup>®</sup> variant 2

Another large cost fraction is the renewable energy source, which is a photovoltaic power plant with a special mechanical structure to fold and unfold the panels from a 20 foot container. The costs of the panel are approximately divided in half for the container and mechanical structure and half for the solar panels mounted on the mechanical structure. Moreover, the battery guarantees security of supply during high peak loads where the response time of the fuel cell is not adequate. With regards to costs, the battery including the bidirectional converter or battery charger account for only 1 % of the overall equipment cost showing therefore minimum cost saving potential.

Besides the pure CAPEX breakdown, the CAPEX in relation to the energy supplied to the consumers is an important key performance indicator (KPI) for an off-grid energy system with regards to economics. For this reason, the expected annual energy demand of 23.9 MWh is set in relation to the CAPEX over a period of 25 years, which is in the following referred to as levelized CAPEX (LCAPEX). By using LCAPEX only the cost of the equipment is considered without taking into account several other cost factors such as operation and maintenance costs, transport and installation costs, cost for water supply, profit margins or market effects such as inflation. SelfHY<sup>®</sup> is intended to electrify remote areas and provide the basic human need for energy without putting the priority on large profitability margins. For this reason, the LCAPEX are a suitable KPI to quantify the initial investment cost in dependence of the energy demand, which is to be covered at the specific site. Due to the self-sufficiency and automated operational control of the system, the operational and maintenance costs as well as the costs for chemicals or utilities are reduced to a minimum. The initial CAPEX and LCAPEX for the four selfHY<sup>®</sup> variants are summarized in Figure 8.2 and show the trend, that

CAPEX increase with system size while LCAPEX decrease with system size. In order to define a cost range taking contingencies and volatility of market prices into account, the initial case is varied according to class 3 accuracy for cost estimation in the process industry of the AACE cost estimate classification system (see Figure 8.2).

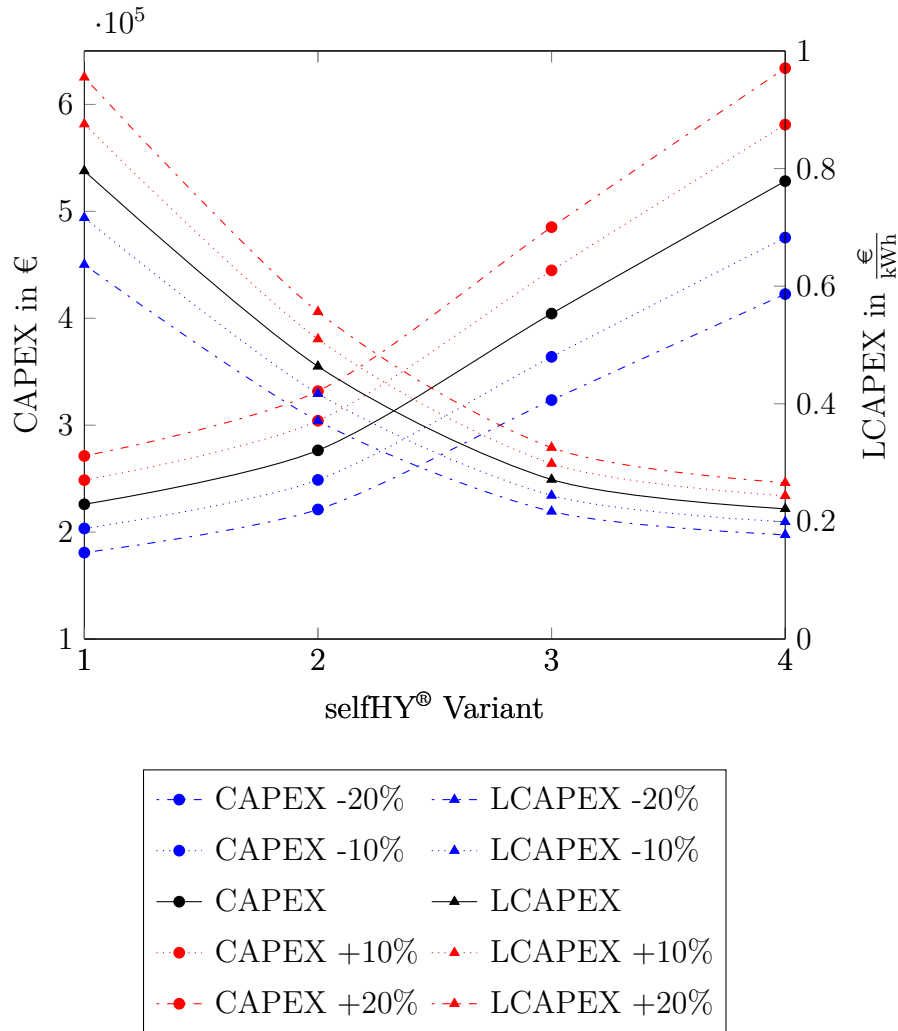


**Figure 8.2:** Sensitivity analysis of CAPEX and LCAPEX

In order to get a more detailed and accurate picture of the total expenditure of selfHY®, the levelized cost of energy are calculated in the following expanding LCAPEX with all possible operational expenditure (OPEX). The operational expenditure includes the replacement of nitrogen bottles and chemicals for the water treatment unit as well as local personnel for maintenance and operational services. No expenses are incurred for the water intake due to the assumptions, that available ground or rain water is used and the respective infrastructure is already existent.

Furthermore, maintenance and installation costs with necessary repairs and possible exchange of equipment are included in the OPEX, whereas the profit margins and market effects such as inflation are taken into regard by a discount factor  $d$ . The transport costs have been excluded from the  $LCOE$  due to a high dependency on the location. If selfHY® is manufactured in Europe or the Americas, a full transport via

ship and truck to a potential market in Africa are expected to be in the range of 5,000 to 10,000 €. It is to mention that additional costs for land preparation or acquisition are not included in the *LCOE*.

For the calculation of the *LCOE*, Equation (8.1) according to SIMON-MARTIN ET AL. 2022 is utilized, where  $C_0$  represent the CAPEX,  $O_0$  the yearly OPEX,  $E_a$  the annual energy production and  $d$  the discount rate. The *LCOE* is determined over the product life span  $n$  of selfHY<sup>®</sup>, which is chosen to twenty-five years. Moreover, the residual value at the end of the product life span is set to result in zero based on a constant depreciation rate and is therefore not considered in the calculation of *LCOE*.

$$LCOE = \frac{C_0 \cdot d}{E_a \cdot [1 - (1 + d)^{-n}]} + \frac{O_0}{E_a} \quad (8.1)$$

For the *LCOE* of selfHY<sup>®</sup>, Equation (8.1) can be applied because it is supposed, that the yearly OPEX are divided uniformly along the life span of the product while periodic costs are the same in nominal terms during the lifespan. Moreover, the yearly energy production  $E_a$  is assumed to remain constant over the product life span. For the CAPEX the previous results from Figure 8.2 are used while the OPEX are set to 1% of the initial CAPEX per year. Accordingly the annual energy production  $E_a$  is scaled up depending on the selfHY<sup>®</sup> variant analyzed. In Figure 8.3 the *LCOE* for different discount rates is visualized concluding that variant 4 ranges in costs from 0.34 to 0.76  $\frac{\text{€}}{\text{kWh}}$  and is therefore the most economic option.

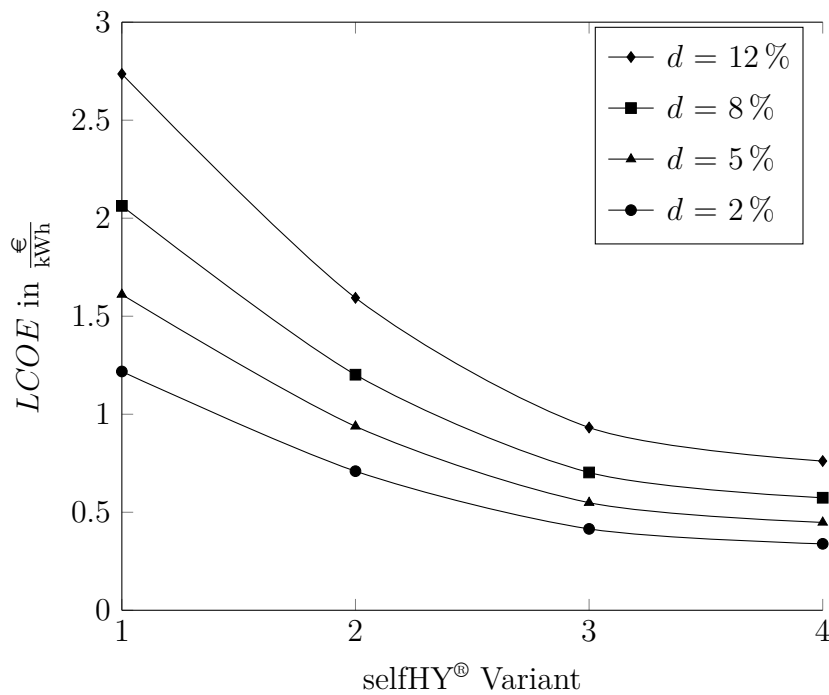


**Figure 8.3:** Sensitivity analysis of *LCOE* for different discount factors  $d$

Depending on the discount factor, the *LCOE* shows strong deviations, which implies a high influence of this parameter choice on the economics. The discount rate is defined by

the investor and depends very much on the market circumstances, technology readiness level of the product and required profitability of the project. For this case study, typical discount rates used by companies in the range from 2 to 12 % are chosen [PEČENAK ET AL. 2020]. Keeping the goal of selfHY<sup>®</sup> in mind to electrify remote areas, it is likely that the discount rates can be considered lower due to the probable investment and involvement of government and state organizations. However, if private investments are considered, higher discount rates will apply and therefore higher electricity prices are expected.

One way to compensate the insecurity of this investment and thereby lowering discount rates is the use of public and innovation funds on national as well as international level connected with government guarantees for investors. In the interest of the global economy and the climate protection goals, the electrification of remote areas in a renewable manner is one of the key challenges to overcome in the next decades. For this reason, it is inevitable to provide the human need for energy and security of energy supply to countries with rural electrification demand and find solutions to justify economic investments in this field.

Potential cost savings, besides the expected price decrease in hydrogen technology over the next years, is the potential to reduce costs by production of many selfHY<sup>®</sup> units, in the best case fully or semi-automated. The economic evaluation in this work only considers the costs of manufacturing one particular unit of selfHY<sup>®</sup>. The cost savings, if higher quantities of the system components are manufactured, can reduce the overall price significantly due to effects from economy of scale. For the whole operational lifetime the degradation of the electrolyzer stack and the fuel cell are to be considered and possible replacement is needed after around 80,000 operational hours, which is considered in the yearly OPEX  $O_0$ .

However, the hydrogen production can also be compensated not only by renewing the electrolyzer stack, but also by adding more renewable energy power to compensate for the degradation and the lower reaction mechanisms within the electrolyzer stack. On the other side, the degradation of the fuel cell causes lower maximum electrical power output, but still allows operation without considerably higher hydrogen consumption. For this reason, a detailed analysis on the options and respective costs of maintaining degrading components needs to be assessed in order to identify the best solution and minimize OPEX. Another aspect for cost saving potential is the elimination of additional hydrogen storage container in variants 3 and 4. As previously mentioned, by increasing the storage pressure, the necessary storage volume is reduced. At a storage pressure of around 280 bar, the required energy content could be stored in four hydrogen storage tanks considering the same spatial requirements as for the present storage at 60 bar.

In the following section the results from the cost estimation of the selfHY<sup>®</sup> variants are compared to other costs of microgrids with different configuration such as battery energy storage, diesel generator or hybrid energy systems.

## 8.2 Comparison with other Renewable Microgrids

Based on literature review of exemplary and comparable techno-economical assessments for off-grid energy systems, this section compares the costs and puts the economic feasibility of selfHY<sup>®</sup> into perspective. In Table 8.1 the results are summarized with the most important technical parameters of each energy system. It is noticeable that all variants of selfHY<sup>®</sup> except variant 1 are comparable to the *LCOE* of the other energy systems. In particular, selfHY<sup>®</sup> variant 2 and 3 are in the forecasted range of IRENA and below the costs of diesel generators according to ZEBRA ET AL. 2021.

However, the lowest *LCOE* is achieved by hybrid systems with around  $0.21 \frac{\text{€}}{\text{kWh}}$ . For locations in South Korea and Bangladesh, these energy systems have been analyzed and it can be concluded that a combination of photovoltaic power plants and wind turbines is a beneficial configuration for the renewable energy system in part due to the countercyclical availability. Moreover, storage capacities by means of BESS or hydrogen increase the initial CAPEX, but show major advantages for security of supply and *LCOE*. It is to mention that for the location in South Korea the installation of hydrogen storage has even shown negligible advantages in costs due to the possibility to decrease battery storage capacity. Another reason for the lower costs is the design premise to stay below 1 % of unmet load and not aim for energy supply at all time, which also leads to positive cost effects. Furthermore, the lower *LCOE* for selfHY<sup>®</sup> variant 4 can be ascribed to the upscaling effects of this larger plant design with approximately ten times the electrolyzer capacity compared to variant 1. In general, each assessment on *LCOE* of remote energy systems highly depends on the available renewable energy and its consistency throughout the year at the given location. Each undertaking of installing a remote energy system requires an in-depth analysis on technical feasibility and economics in order to conclude the optimal energy system configuration.

Ultimately, this work verifies that storage options with hydrogen are comparable from an economic and technical point of view to the currently more established solutions of battery energy storage on the market. Energy system configurations involving diesel generators show increased costs and can be viewed as not in line with current climate protection goals. On the contrary, hydrogen energy systems such as selfHY<sup>®</sup> are in line with current decarbonization goals and need to be considered in the future for rural electrification. For this reason, efforts shall be made to increase research activities in this field as well as to develop pilot plants of this kind. Inspired by this conclusion, the next chapter gives an outlook on necessary steps to push the needle forward on the maturity of hydrogen energy systems for rural electrification.

**Table 8.1:** *LCOE* of other microgrids and selfHY<sup>®</sup>

	Energy in MWh	CO <sub>2</sub> in $\frac{t}{a}$	<i>LCOE</i> in $\frac{€}{kWh}$	Source
<b>Bamako, Mali</b> selfHY <sup>®</sup> Variant 1	11	0	1.22	
<b>Bamako, Mali</b> selfHY <sup>®</sup> Variant 2	24	0	0.71	
<b>Bamako, Mali</b> selfHY <sup>®</sup> Variant 3	60	0	0.41	
<b>Bamako, Mali</b> selfHY <sup>®</sup> Variant 4	95	0	0.34	
<b>South Korea</b> DG 2 x 150 kW	1,228	1,013	0.445	MUN ET AL. 2021
<b>South Korea</b> PV 700 kW WT 250 kW BESS 2,308 kWh	2,806	0	0.21	MUN ET AL. 2021
<b>South Korea</b> PV 500 kW WT 750 kW BESS 288 kWh H <sub>2</sub> Store 200 kg ELY 200kW FC 250 kW	2,782	0	0.208	MUN ET AL. 2021
<b>Yanbu,</b> <b>Saudi-Arabia</b> PV 55 kW BM 981 $\frac{t}{a}$	≈ 160	> 0	0.28	KHARRICH ET AL. 2021
<b>Yanbu,</b> <b>Saudi-Arabia</b> PV 55 kW DG 25 kW BESS 11-28 kWh	≈ 160	> 0	0.4 - 0.33	KHARRICH ET AL. 2021
<b>Barishal,</b> <b>Bangladesh</b> PV 65 kW WT 1 kW BESS 135 kWh DG 3 kW	≈ 239	3.3	0.22	ISHRAQUE ET AL. 2021
DG	-	> 0	0.92 - 1.3	ZEBRA ET AL. 2021
PV	-	0	0.4 - 0.61	ZEBRA ET AL. 2021
PV & DG	-	> 0	0.54 - 0.77	ZEBRA ET AL. 2021
PV 30 kW	-	0	0.4 - 0.61	ZEBRA ET AL. 2021 RUUD 2013
Mini-grids in 2025	-	-	0.35 - 0.5	IRENA 2016



## 9 Outlook

In this work, a concept of the hydrogen energy system selfHY<sup>®</sup>, utilized for rural electrification, has been developed proving current economic feasibility by comparing it to other remote energy systems such as BESS and diesel generators. Nevertheless, the current development and installation of hydrogen energy systems is proceeding slowly focusing especially on domestic solutions for homes in industrial countries to support decarbonization efforts. In developing countries, where the electrical infrastructure is not as advanced and many people live in rural areas without access to public infrastructure, hydrogen energy systems have been given too little attention as a solution to the problem of rural electrification. It is commonly accepted that for reducing the carbon emissions according to the Paris Agreement many sustainable solutions and technologies need to be considered and advanced. For this reason, also hydrogen energy systems, which have been neglected in the past as a solution to rural electrification, need to be fostered and analyzed further in order to find beneficial areas of application.

This work shows for the exemplary location of Bamako in Mali that hydrogen energy systems can be the solutions for rural electrification. However, this cannot be generalized, because there are also locations where BESS or other options with hybrid renewable energy sources pose the best solution for a self-sufficient energy system. Therefore, site location assessments on rural areas, where access to energy is not provided, shall be conducted with the focus to define the optimal types of energy system configuration based on the renewable energy sources, availability of water and other important circumstances on site. In a similar approach as the development of the H2Atlas-Africa by FORSCHUNGSZENTRUM JÜLICH 2022, which identifies green hydrogen potential in West Africa, a map for rural electrification potential with hydrogen needs to be created. With these results, the international market potential can be estimated leading to possible cost benefits by economy of scale, which enhance the overall economic viability of energy systems in remote areas. By taking advantage of the current momentum for establishing a worldwide hydrogen economy and the expectation that costs will decrease in hydrogen technology, the technical readiness of hydrogen energy systems needs to be commercialized as soon as possible in order to enable a fast scale-up. Also new and innovative technologies for containerized hydrogen energy systems need to be considered simultaneously. One example would be electrochemical hydrogen compressors, which are currently entering the market and showing benefits in higher storage pressures while featuring a compact design with no rotational elements.

Finally, there is to mention that incentives by government organizations and funds for hydrogen technology development in the field of rural electrification can accelerate the deployment of these systems and allow to make up ground on already more established energy systems such as BESS. These presented topics can help to reach the goal of developing a robust and economic energy system for rural electrification with hydrogen, so easy to access, use and install as today's refrigerators.



# A Operating Modes and Active Streams

**Table A.1:** Active energy and process streams for different operating modes according to block flow diagram shown in Figure 4.3

Stream	Mode	H <sub>2</sub> generation	H <sub>2</sub> reversion	Battery charging
		$\Delta P > 0$	$\Delta P < 0$	$0 < \Delta P < P_{Ely,DC,min}$
1		✓		✓
2		✓		✓
3		✓		
4		✓		
5		✓		
6		✓		
7		✓		
8		✓		
9		✓		
10		✓		
11		✓		
12		✓		
13		✓		
14		✓		
15		✓		
16			✓	
17			✓	
18			✓	
19			✓	
20			✓	✓
21			✓	✓
22		✓	✓	✓



## B Parameter Values for Simulation

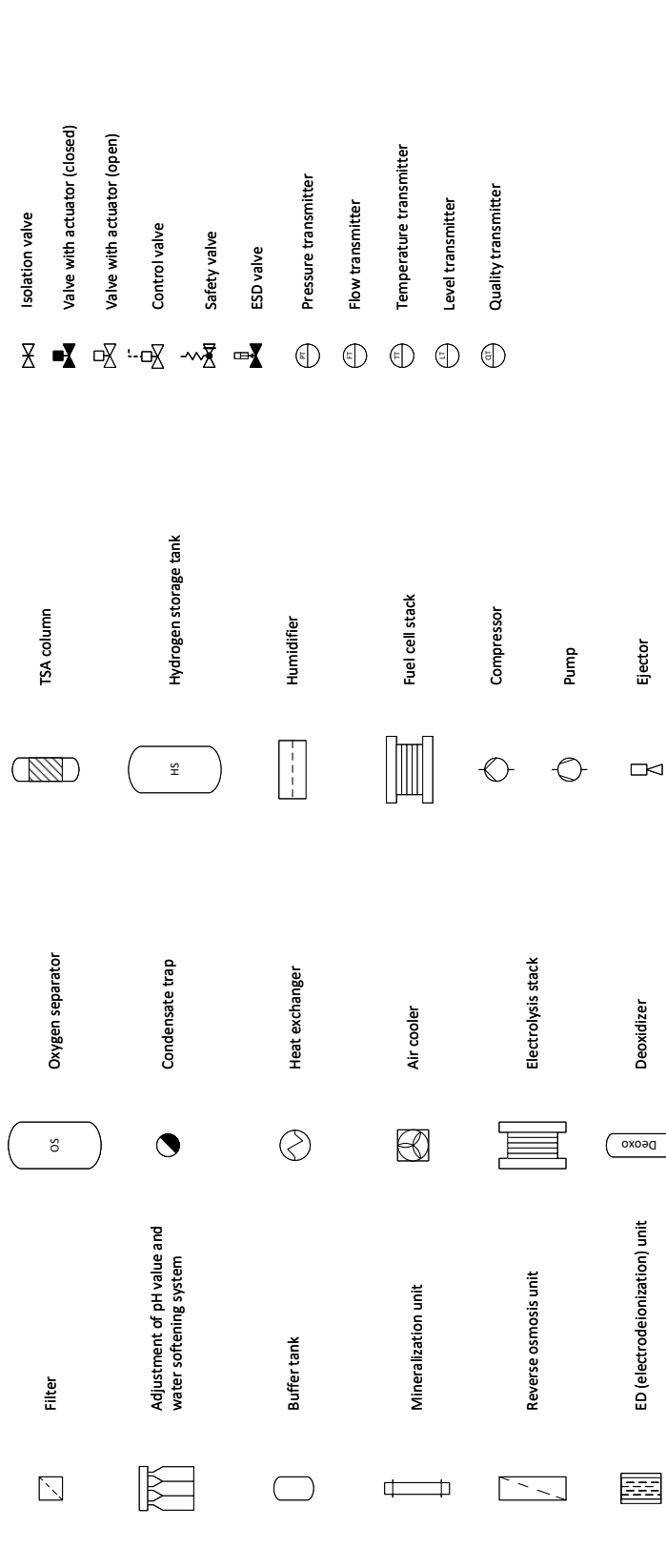
$A_{Ely,Cell}$	0.1	$\text{cm}^2$	$p_{Ely}$	2	bar
$A_{FC,Cell}$	0.1	$\text{cm}^2$	$p_{Store}$	60	bar
$A_{Panel}$	2	$\text{cm}^2$	$P_{Panel}$	0.5	kW
$c_{drag}$	2		$s$	15	
$c_{HP}$	0.08	$\frac{\text{kW}}{\text{Nm}^3}$	$s_{Bat}$	1.2	
$c_{W,demi}$	0.803		$s_{PV}$	1.5	
$e_{WT}$	3	kWh	$S_{O_2}$	$9.8 \times 10^{-6}$	$\frac{\text{mol}}{\text{Pa m}^3}$
$f_{Bat}$	0.02		$T_{Ely}$	70	$^{\circ}\text{C}$
$f_{Ely,cool}$	0.02		$V(t_0)_{Tank}$	0	$\text{m}^3$
$f_{FC,cool}$	0.15		$z$	2	
$\Delta h_{Ely,cool}$	21	$\frac{\text{kJ}}{\text{kg}}$	$\eta_{AC/DC,Ely}$	0.98	
$\Delta h_{FC,cool}$	29	$\frac{\text{kJ}}{\text{kg}}$	$\eta_{Bat}$	0.98	
$LHV_{H_2}$	33.3	$\frac{\text{kWh}}{\text{kg}}$	$\eta_{DCAC}$	1	
$N_{Ely,Stack}$	1		$\eta_{el}$	0.95	
$N_{FC,Stack}$	1		$\eta_F$	0.98	
$r_{HD}$	2.5		$\eta_{is}$	0.85	
$\Delta t$	1	h	$\eta_{WT}$	0.6	
$\dot{V}_{W,pot,p.P.}$	10	$\frac{\text{L}}{\text{h}}$	$\tau$	5	min
$p_{O_2}^a$	1.7	bar			





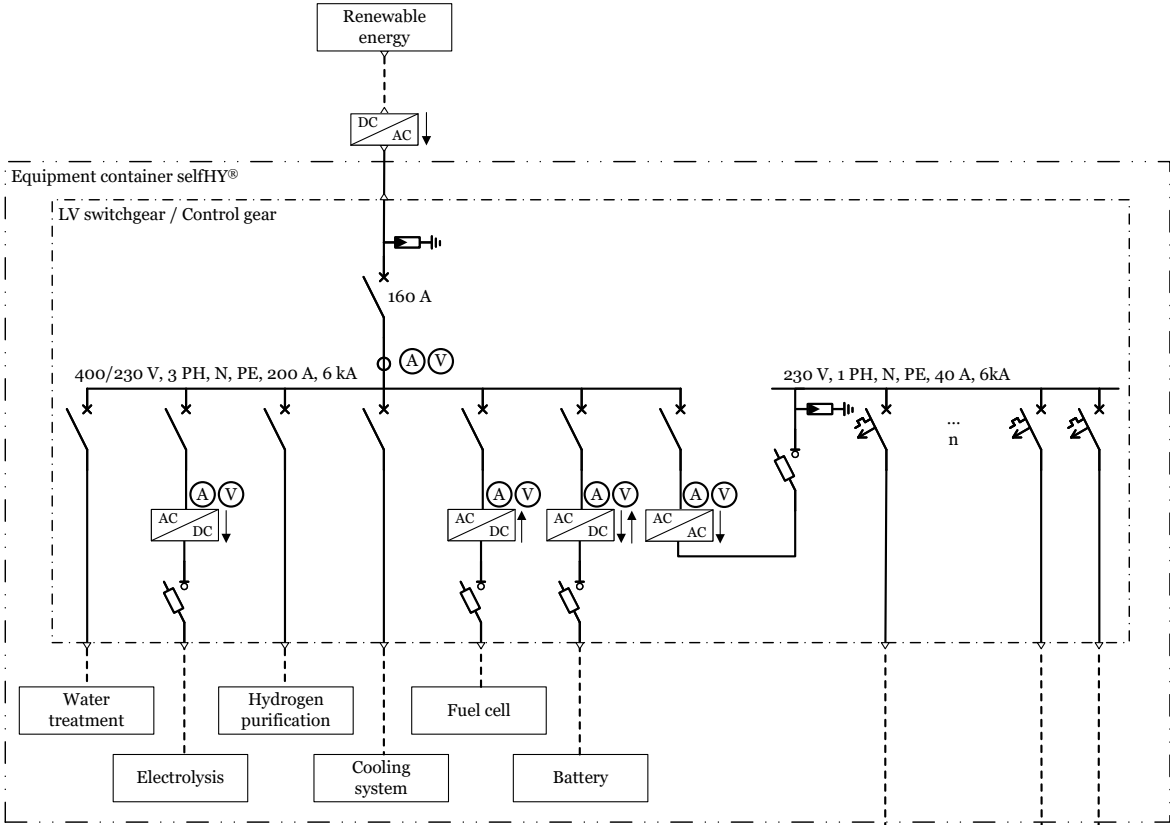
selfHy® Variant 2

Stream	1	2	3	4	5	6	7	8	9	10	11
Medium	Deionate	Potable water	Deionate	H2	Condensate	H2	H2	Air	Humid air	Coolant	Coolant
Flow rate	Nm <sup>3</sup> /h 0 - 0.1	0 - 0.1	0 - 0.6	0.4 - 2.2	< 2e-5	0.4 - 2.2	0.22 - 1.8	0 - 0.8	0 - 1.5	0 - 0.4	0 - 0.3
	kg/h 0 - 100	0 - 100	0 - 600	0.04 - 0.2	< 0.02	0.04 - 0.2	0.02 - 0.16	0 - 1	0 - 2	0 - 600	0 - 300
Pressure	bar 3 - 6	2	3 - 6	60	60	60	> 2.5	3 - 10	20-30	2	2
Temperature	° C 4 - 20	15	70	70	30	20	20	4 - 40	20	25	25
Quality	-	TrinkwV	≤ 0.1 µS/cm	2.0	≤ 0.1 µS/cm	5.0	5.0	atmos.	abs. LF 5 %	Ethyleneglycol	Ethyleneglycol





# D Single Line Diagram



- |  |                                |  |                |  |   |  |   |
|--|--------------------------------|--|----------------|--|---|--|---|
|  | Circuit breaker                |  | Surge arrester |  | Current transformer                             |  | AC/DC – converter with bidirectional induction of energy flow |
|  | Miniature circuit breaker      |  | Amperemeter    |  | AC/DC – converter with induction of energy flow |  |   |
|  | Load isolator switch with fuse |  | Voltmeter      |  | AC/AC – converter with induction of energy flow |  |   |

Electrical consumers



# Bibliography

AKINYELE ET AL. 2020

AKINYELE, D. ; OLABODE, E. ; AMOLE, A.: *Review of Fuel Cell Technologies and Applications for Sustainable Microgrid Systems*. Inventions 5.3 (Aug. 2020), p. 42. DOI: 10.3390/inventions5030042.

ALBRECHT ET AL. 2020

ALBRECHT, U. ; BÜNGER, U. ; MICHALSKI, J. ; RAKSHA, T. ; WURSTER, R. ; ZERHUSEN, J.: *International hydrogen Strategies - A study commissioned by and in cooperation with the World Energy Council Germany*. World Energy Council Germany, 2020.

ANDERER ET AL. 2010

ANDERER, P. ; DUMONT, U. ; HEIMERL, S. ; RUPRECHT, A. ; WOLF-SCHUMANN, U.: *The Hydropower Potential of Germany*. WasserWirtschaft 100 (Jan. 2010), pp. 12–16.

ANDREA 2020

ANDREA, D. 2020.

ATKINSON ET AL. 2012

ATKINSON, A. ; SKINNER, S. J. ; KILNER, J. A.: *Solid Oxide Fuel Cells solid oxide fuel cell (SOFC)*. *Encyclopedia of Sustainability Science and Technology*. Springer New York, 2012, pp. 9885–9904. DOI: 10.1007/978-1-4419-0851-3\_139.

BARTHELEMY ET AL. 2017

BARTHELEMY, H. ; WEBER, M. ; BARBIER, F.: *Hydrogen storage: Recent improvements and industrial perspectives*. International Journal of Hydrogen Energy 42.11 (Mar. 2017), pp. 7254–7262. DOI: 10.1016/j.ijhydene.2016.03.178.

BASSANI ET AL. 2020

BASSANI, A. ; PREVITALI, D. ; PIROLA, C. ; BOZZANO, G. ; COLOMBO, S. ; MANENTI, F.: *Mitigating Carbon Dioxide Impact of Industrial Steam Methane Reformers by Acid Gas to Syngas Technology: Technical and Environmental Feasibility*. Journal of Sustainable Development of Energy, Water and Environment Systems 8.1 (Mar. 2020), pp. 71–87. DOI: 10.13044/j.sdewes.d7.0258.

BESSARABOV 2018

BESSARABOV, D. G.: *PEM water electrolysis*. London, United Kingdom: Academic Press, an imprint of Elsevier, 2018. ISBN: 9780081028308.

BEZMALINOVIĆ ET AL. 2013

BEZMALINOVIĆ, D. ; BARBIR, F. ; TOLJ, I.: *Techno-economic analysis of PEM fuel cells role in photovoltaic-based systems for the remote base stations*. International Journal of Hydrogen Energy 38.1 (Jan. 2013), pp. 417–425. DOI: 10.1016/j.ijhydene.2012.09.123.

BHUTTA ET AL. 2012

BHUTTA, M. M. A. ; HAYAT, N. ; FAROOQ, A. U. ; ALI, Z. ; JAMIL, S. R. ; HUSSAIN, Z.: *Vertical axis wind turbine – A review of various configurations and design techniques*. Renewable and Sustainable Energy Reviews 16.4 (May 2012), pp. 1926–1939. DOI: 10.1016/j.rser.2011.12.004.

BLANCO 2016

BLANCO, M.: *Advances in Concentrating Solar Thermal Research and Technology*. Kent: Elsevier Science, 2016. ISBN: 9780081005170.

BLUMENTHAL 2020

BLUMENTHAL, K. VON: *Preiswerter grüner Wasserstoff für jedermann*. First Berlin Equity Research (2020).

BOBBE ET AL. 2016

BOBBE, T. ; KRZYWINSKI, J. ; WOELFEL, C.: *A Comparison of Design Process Models from Academic Theory and Professional Practice*. Jan. 2016.

BONILLA-PETRICIOLET ET AL. 2017

BONILLA-PETRICIOLET, A. ; MENDOZA-CASTILLO, D. I. ; REYNEL-ÁVILA, H. E., eds.: *Adsorption Processes for Water Treatment and Purification*. Springer International Publishing, 2017. DOI: 10.1007/978-3-319-58136-1.

BRATSCH 1989

BRATSCH, S. G.: *Standard Electrode Potentials and Temperature Coefficients in Water at 298.15 K*. Journal of Physical and Chemical Reference Data 18.1 (Jan. 1989), pp. 1–21. DOI: 10.1063/1.555839.

BRAUNS & TUREK 2020

BRAUNS, J. ; TUREK, T.: *Alkaline Water Electrolysis Powered by Renewable Energy: A Review*. Processes 8.2 (Feb. 2020), p. 248. DOI: 10.3390/pr8020248.

BREEZE 2016

BREEZE, P.: *Chapter 4 - Parabolic Trough and Fresnel Reflector Solar Power Plants. Solar Power Generation*. Ed. by P. BREEZE. Academic Press, 2016, pp. 25–34. ISBN: 978-0-12-804004-1. DOI: <https://doi.org/10.1016/B978-0-12-804004-1.00004-X>. URL: <https://www.sciencedirect.com/science/article/pii/B978012804004100004X>.

BURTON ET AL. 2011

BURTON, T. ; JENKINS, N. ; SHARPE, D. ; BOSSANYI, E.: *Wind Energy Handbook*. Wiley, May 2011. DOI: 10.1002/9781119992714.

CARDELLA 2018

CARDELLA, U. F.: *Large-scale hydrogen liquefaction under the aspect of economic viability*. PhD thesis. Technische Universität München, Lehrstuhl für Anlagen- und Prozesstechnik, 2018.

CARMO ET AL. 2013

CARMO, M. ; FRITZ, D. L. ; MERGEL, J. ; STOLTEN, D.: *A comprehensive review on PEM water electrolysis*. International Journal of Hydrogen Energy 38.12 (Apr. 2013), pp. 4901–4934. DOI: 10.1016/j.ijhydene.2013.01.151.

CENTER FOR SUSTAINABLE SYSTEMS 2020

CENTER FOR SUSTAINABLE SYSTEMS: *Wind Energy Factsheet*. Pub. No. CSS07-09. (2020).

CENTRE. 2018

CENTRE., E. C. J. R.: *Li-ion batteries for mobility and stationary storage applications: scenarios for costs and market growth*. Publications Office, 2018. DOI: 10.2760/87175.

CHROMETZKA ET AL. 2020

CHROMETZKA, T. ; POTISAT, T. ; QUINN, A.: *Ditching the diesel: Hydrogen Microgrids*. Enapter S.r.l, 2020.

CLARKE 2015

CLARKE, D.: *Stand-alone solar-pv hydrogen energy systems incorporating reverse osmosis*. PhD thesis. Edith Cowan University, 2015. URL: <https://ro.ecu.edu.au/theses/1750/>.

CORÀ 2019

CORÀ, E.: *Hydropower Technologies - The State of the Art*. Hydropower Europe, 2019.

CORKE 2018

CORKE, T.: *Wind Energy Design*. Boca Raton, FL: CRC Press, 2018. ISBN: 9781315105468.

CRITTENDEN ET AL. 2012

CRITTENDEN, J. C. ; TRUSSELL, R. R. ; HAND, D. W. ; HOWE, K. J. ; TCHOBANOGLOUS, G.: *MWH's Water Treatment*. John Wiley & Sons, Inc., Mar. 2012. DOI: 10.1002/9781118131473.

DAI ET AL. 2016

DAI, J. ; LIU, D. ; WEN, L. ; LONG, X.: *Research on power coefficient of wind turbines based on SCADA data*. Renewable Energy 86 (Feb. 2016), pp. 206–215. DOI: 10.1016/j.renene.2015.08.023.

DAUD ET AL. 2017

DAUD, W. ; ROSLI, R. ; MAJLAN, E. ; HAMID, S. ; MOHAMED, R. ; HUSAINI, T.: *PEM fuel cell system control: A review*. Renewable Energy 113 (Dec. 2017), pp. 620–638. DOI: 10.1016/j.renene.2017.06.027.

DESHMUKH 2020

DESHMUKH, S.: *Ultrapure Water Production. Handbook of Water and Used Water Purification*. Springer International Publishing, 2020, pp. 1–22. DOI: 10.1007/978-3-319-66382-1\_106-1.

DINCER 2002

DINCER, I.: *Technical, environmental and exergetic aspects of hydrogen energy systems*. International Journal of Hydrogen Energy 27.3 (Mar. 2002), pp. 265–285. DOI: 10.1016/s0360-3199(01)00119-7.

E4TECH 2018

E4TECH: *The Fuel Cell Industry Review*. Fuel Cell Industry Review, 2018.

ERICKSON & MAKSIMOVIĆ 2020

ERICKSON, R. W. ; MAKSIMOVIĆ, D.: *Fundamentals of Power Electronics*. Springer International Publishing, 2020. DOI: 10.1007/978-3-030-43881-4.

ERIKSEN 2018

ERIKSEN, J.: *HYMEHC-04 Expandable*. HYSTORSYS AS, 2018.

ESMAP 2020

ESMAP: *Green Hydrogen in Developing Countries*. World Bank, Washington, DC, 2020.

EURELECTRIC & VGB POWERTECH E.V. 2018

EURELECTRIC ; VGB POWERTECH E.V.: *Hydropower - Fact sheets*. 2018.

FASTERHOLDT ET AL. 2018

FASTERHOLDT, I. ; LEE, A. ; KIDHOLM, K. ; YDERSTRÆDE, K. B. ; PEDERSEN, K. M.: *A qualitative exploration of early assessment of innovative medical technologies*. BMC Health Services Research 18.1 (Nov. 2018). DOI: 10.1186/s12913-018-3647-z.

FLETCHER & EBRAHIMI 2020

FLETCHER, T. ; EBRAHIMI, K.: *The Effect of Fuel Cell and Battery Size on Efficiency and Cell Lifetime for an L7e Fuel Cell Hybrid Vehicle*. *Energies* 13.22 (Nov. 2020), p. 5889. DOI: 10.3390/en13225889.

FORSCHUNGSZENTRUM JÜLICH 2022

FORSCHUNGSZENTRUM JÜLICH: *ECOWAS H2Atlas*. Institut für Energie- und Klimaforschung – Technoökonomische Systemanalyse (IEK-3), 2022.

FRANK BRUIJN & JANSSEN 2017

FRANK BRUIJN, A. DE; JANSSEN, G. J. M.: *PEM Fuel Cell Materials: Costs, Performance and Durability*. *Encyclopedia of Sustainability Science and Technology*. Springer New York, 2017, pp. 1–41. DOI: 10.1007/978-1-4939-2493-6\_152-3.

FRAUNHOFER ISE 2020

FRAUNHOFER ISE: *Höhere Wirkungsgrade bei Organischer Photovoltaik – neuer Solarzellenrekord auf 1 cm<sup>2</sup>*. Press Release. 2020. URL: [https://www.ise.fraunhofer.de/content/dam/ise/de/images/presseinfos/2020/2520\\_ISE\\_d\\_OPV\\_1cm2\\_Rekord.pdf](https://www.ise.fraunhofer.de/content/dam/ise/de/images/presseinfos/2020/2520_ISE_d_OPV_1cm2_Rekord.pdf).

FUEL CELLS AND HYDROGEN JOINT UNDERTAKING 2019

FUEL CELLS AND HYDROGEN JOINT UNDERTAKING: *Towards a dual hydrogen certification system for guarantees of origin and for the certification of renewable hydrogen in transport and for heating & cooling: final report of phase 2*. Publications Office, 2019. DOI: 10.2843/46282.

GHERMANDI & MESSALEM 2009

GHERMANDI, A. ; MESSALEM, R.: *Solar-driven desalination with reverse osmosis: the state of the art*. *Desalination and Water Treatment* 7.1-3 (July 2009), pp. 285–296. DOI: 10.5004/dwt.2009.723.

GIESECKE & HEIMERL 2014

GIESECKE, J. ; HEIMERL, S.: *Wasserkraftanlagen*. Springer Berlin Heidelberg, 2014. DOI: 10.1007/978-3-642-53871-1.

GIULIANO 2014

GIULIANO, S.: *Solare Turmkraftwerke bei erhöhten Temperaturen*. (2014).

GOSHTASBI ET AL. 2019

GOSHTASBI, A. ; CHEN, J. ; WALDECKER, J. R. ; HIRANO, S. ; ERSAL, T.: *On Parameterizing PEM Fuel Cell Models*. 2019 American Control Conference (ACC). 2019, pp. 903–908. DOI: 10.23919/ACC.2019.8815294.

GSTÖHL & PFENNINGER 2020

GSTÖHL, U. ; PFENNINGER, S.: *Energy self-sufficient households with photovoltaics and electric vehicles are feasible in temperate climate*. PLOS ONE 15.3 (Mar. 2020). Ed. by C. LV, e0227368. DOI: 10.1371/journal.pone.0227368.

HARRIS ET AL. 2020

HARRIS, I. ; OSBORN, T. J. ; JONES, P. ; LISTER, D.: *Version 4 of the CRU TS monthly high-resolution gridded multivariate climate dataset*. Scientific Data 7.1 (Apr. 2020). DOI: 10.1038/s41597-020-0453-3.

HAUG 2019

HAUG, P.: *Experimental and theoretical investigation of gas purity in alkaline water electrolysis*. PhD thesis. Clausthal University of Technology, 2019.

HEINZELMANN 2011

HEINZELMANN, B.: *Strömungsbeeinflussung bei Rotorblättern von Windenergieanlagen mit Schwerpunkt auf Grenzschichtabsaugung*. PhD thesis. Technische Universität Berlin, 2011. URL: [https://depositonce.tu-berlin.de/bitstream/11303/3272/1/Dokument\\_11.pdf](https://depositonce.tu-berlin.de/bitstream/11303/3272/1/Dokument_11.pdf).

HEMMES 2021

HEMMES, K.: *A personal retrospect on three decades of high temperature fuel cell research; ideas and lessons learned*. International Journal of Hydrogen Energy 46.28 (Apr. 2021), pp. 14962–14976. DOI: 10.1016/j.ijhydene.2020.12.196.

HENKENSMEIER ET AL. 2020

HENKENSMEIER, D. ; NAJIBAH, M. ; HARMS, C. ; ŽITKA, J. ; HNÁT, J. ; BOUZEK, K.: *Overview: State-of-the Art Commercial Membranes for Anion Exchange Membrane Water Electrolysis*. Journal of Electrochemical Energy Conversion and Storage 18.2 (Aug. 2020). DOI: 10.1115/1.4047963.

HOES ET AL. 2017

HOES, O. A. C. ; MEIJER, L. J. J. ; ENT, R. J. VAN DER ; GIESEN, N. C. VAN DE: *Systematic high-resolution assessment of global hydropower potential*. PLOS ONE 12.2 (Feb. 2017). Ed. by Z. D. DENG, e0171844. DOI: 10.1371/journal.pone.0171844.

HÖFNER 2016

HÖFNER, T.: *Entwicklung von Membran-Elektroden-Einheiten für die Anionenaustauschmembran-Wasserelektrolyse*. PhD thesis. Rheinisch-Westfälische Technische Hochschule Aachen, 2016.



HUSSAIN & YANGPING 2020

HUSSAIN, S. ; YANGPING, L.: *Review of solid oxide fuel cell materials: cathode, anode, and electrolyte*. *Energy Transitions* 4.2 (Oct. 2020), pp. 113–126. DOI: 10.1007/s41825-020-00029-8.

IDRISS ET AL. 2015

IDRISS, H. ; SCOTT, M. ; SUBRAMANI, V.: *Introduction to hydrogen and its properties. Compendium of Hydrogen Energy*. Elsevier, 2015, pp. 3–19. DOI: 10.1016/b978-1-78242-361-4.00001-7.

INTERNATIONAL ENERGY AGENCY (IEA) 2019

INTERNATIONAL ENERGY AGENCY (IEA): *The Future of Hydrogen*. IEA, Paris, 2019. URL: <https://www.iea.org/reports/the-future-of-hydrogen>.

IRENA 2016

IRENA: *Innovation Outlook: Renewable Mini-grids*. International Renewable Energy Agency, Abu Dhabi, 2016.

IRENA 2017

IRENA: *Electricity Storage and Renewables: Costs and Markets to 2030*. International Renewable Energy Agency, Abu Dhabi, 2017. URL: [https://www.irena.org/-/media/Files/IRENA/Agency/Publication/2017/Oct/IRENA\\_Electricity\\_Storage\\_Costs\\_2017\\_Summary.pdf](https://www.irena.org/-/media/Files/IRENA/Agency/Publication/2017/Oct/IRENA_Electricity_Storage_Costs_2017_Summary.pdf).

IRENA 2019a

IRENA: *Future of Solar Photovoltaic: Deployment, investment, technology, grid integration and socio-economic aspects (A Global Energy Transformation: paper)*. International Renewable Energy Agency, Abu Dhabi, 2019.

IRENA 2019b

IRENA: *Future of wind: Deployment, investment, technology, grid integration and socio-economic aspects (A Global Energy Transformation paper)*. International Renewable Energy Agency, Abu Dhabi, 2019.

IRENA 2020a

IRENA: *Renewable Energy Statistics 2020*. The International Renewable Energy Agency, Abu Dhabi, 2020.

IRENA 2020b

IRENA: *Renewable Energy Technologies*. International Renewable Energy Agency, Abu Dhabi, 2020. URL: <https://www.irena.org/Statistics/View-Data-by-Topic/Capacity-and-Generation/Technologies>.

## IRENA 2020c

IRENA: *Renewable Power Generation Costs in 2019*. International Renewable Energy Agency, Abu Dhabi, 2020. URL: [https://www.irena.org/-/media/Files/IRENA/Agency/Publication/2020/Jun/IRENA\\_Power\\_Generation\\_Costs\\_2019.pdf](https://www.irena.org/-/media/Files/IRENA/Agency/Publication/2020/Jun/IRENA_Power_Generation_Costs_2019.pdf).

## ISHRAQUE ET AL. 2021

ISHRAQUE, M. F.; SHEZAN, S. A.; RASHID, M. M.; BHADRA, A. B.; HOSSAIN, M. A.; CHAKRABORTTY, R. K.; RYAN, M. J.; FAHIM, S. R.; SARKER, S. K.; DAS, S. K.: *Techno-Economic and Power System Optimization of a Renewable Rich Islanded Microgrid Considering Different Dispatch Strategies*. IEEE Access 9 (2021), pp. 77325–77340. DOI: 10.1109/access.2021.3082538.

## ISLAM ET AL. 2018

ISLAM, M. S.; SULTANA, A.; SAADAT, A. H. M.; ISLAM, M. S.; SHAMMI, M.; UDDIN, M. K.: *Desalination Technologies for Developing Countries: A Review*. Journal of Scientific Research 10.1 (Jan. 2018), pp. 77–97. DOI: 10.3329/jsr.v10i1.33179.

## ISMAIL 2017

ISMAIL, B. I.: *Introductory Chapter - Aspects of Renewable Hydroelectric Power Generation*. *Renewable Hydropower Technologies*. InTech, July 2017. DOI: 10.5772/67563.

## JURISIC ET AL. 2021

JURISIC, T.; REHFELDT, S.; KNELLER, M.; KLEIN, H.: *Range of application for a self-sufficient energy system with hydrogen as energy carrier in remote areas*. Proceedings of Global Power and Propulsion Society. 2021.

## KALTSCHMITT ET AL. 2013

KALTSCHMITT, M.; STREICHER, W.; WIESE, A.: *Erneuerbare Energien*. Springer Berlin Heidelberg, 2013. DOI: 10.1007/978-3-642-03249-3.

## KANURI &amp; MOTUPALLY 2012

KANURI, S. V.; MOTUPALLY, S.: *Phosphoric Acid Fuel Cells for Stationary Applications*. *Fuel Cells and Hydrogen Production*. Springer New York, 2012, pp. 515–530. DOI: 10.1007/978-1-4939-7789-5\_150.

## KEUSCHNIGG 2016

KEUSCHNIGG, R.: *CFD-Simulation einer mit Dieselreformat betriebenen SOFC-Brennstoffzelle*. MA thesis. Technischen Universität Graz - Institut für Wärmetechnik, 2016.

KHAN ET AL. 2020

KHAN, M. S. ; XU, X. ; KNIBBE, R. ; REHMAN, A. UR ; LI, Z. ; YAGO, A. J. ; WANG, H. ; ZHU, Z.: *New Insights into the Degradation Behavior of Air Electrodes during Solid Oxide Electrolysis and Reversible Solid Oxide Cell Operation*. Energy Technology 8.9 (Aug. 2020), p. 2000241. DOI: 10.1002/ente.202000241.

KHARRICH ET AL. 2021

KHARRICH, M. ; KAMEL, S. ; ALGHAMDI, A. S. ; EID, A. ; MOSAAD, M. I. ; AKHERRAZ, M. ; ABDEL-AKHER, M.: *Optimal Design of an Isolated Hybrid Microgrid for Enhanced Deployment of Renewable Energy Sources in Saudi Arabia*. Sustainability 13.9 (Apr. 2021), p. 4708. DOI: 10.3390/su13094708.

KLELL ET AL. 2018

KLELL, M. ; EICHLSEDER, H. ; TRATTNER, A.: *Wasserstoff in der Fahrzeugtechnik: Erzeugung, Speicherung, Anwendung*. deutsch. 4. Deutschland: Springer Vieweg, Apr. 2018. ISBN: 978-3658204464.

KLOSE ET AL. 2020

KLOSE, C. ; SAATKAMP, T. ; MÜNCHINGER, A. ; BOHN, L. ; TITVINIDZE, G. ; BREITWIESER, M. ; KREUER, K.-D. ; VIERRATH, S.: *All-Hydrocarbon MEA for PEM Water Electrolysis Combining Low Hydrogen Crossover and High Efficiency*. Advanced Energy Materials 10.14 (Feb. 2020), p. 1903995. DOI: 10.1002/aenm.201903995.

KONSTANTIN 2013

KONSTANTIN, P.: *Praxisbuch Energiewirtschaft*. Springer Berlin Heidelberg, 2013. DOI: 10.1007/978-3-642-37265-0.

KOST 2018

KOST, C.: *Levelized Cost of Electricity Renewable Energy Technologies*. Fraunhofer Institute for Solar Energy Systems ISE, 2018. URL: [https://www.ise.fraunhofer.de/content/dam/ise/en/documents/publications/studies/EN2018\\_Fraunhofer-ISE\\_LCOE\\_Renewable\\_Energy\\_Technologies.pdf](https://www.ise.fraunhofer.de/content/dam/ise/en/documents/publications/studies/EN2018_Fraunhofer-ISE_LCOE_Renewable_Energy_Technologies.pdf).

KRASAE-IN ET AL. 2010

KRASAE-IN, S. ; STANG, J. H. ; NEKSA, P.: *Development of large-scale hydrogen liquefaction processes from 1898 to 2009*. International Journal of Hydrogen Energy 35.10 (May 2010), pp. 4524–4533. DOI: 10.1016/j.ijhydene.2010.02.109.

KULKARNI & GIDDEY 2012

KULKARNI, A. ; GIDDEY, S.: *Materials issues and recent developments in molten carbonate fuel cells*. Journal of Solid State Electrochemistry 16.10 (June 2012), pp. 3123–3146. DOI: 10.1007/s10008-012-1771-y.

KUMAR ET AL. 2020

KUMAR, K.; ALAM, M.; VERMA, S.; DUTTA, V.: *Analysis of metal hydride storage on the basis of thermophysical properties and its application in microgrid*. Energy Conversion and Management 222 (Oct. 2020), p. 113217. DOI: 10.1016/j.enconman.2020.113217.

KUMAR 2015

KUMAR, S.: *Clean Hydrogen Production Methods*. Springer International Publishing, 2015. DOI: 10.1007/978-3-319-14087-2.

KURZWEIL 2016

KURZWEIL, P.: *Brennstoffzellentechnik*. Springer Fachmedien Wiesbaden, 2016. DOI: 10.1007/978-3-658-14935-2.

KURZWEIL & DIETLMEIER 2018

KURZWEIL, P.; DIETLMEIER, O. K.: *Elektrochemische Speicher*. Springer Fachmedien Wiesbaden, 2018. DOI: 10.1007/978-3-658-21829-4.

LAASCH & LAASCH 2013

LAASCH, T.; LAASCH, E.: *Haustechnik*. Springer Fachmedien Wiesbaden, 2013. DOI: 10.1007/978-3-8348-9900-2.

LAGUNA-BERCERO 2012

LAGUNA-BERCERO, M.: *Recent advances in high temperature electrolysis using solid oxide fuel cells: A review*. Journal of Power Sources 203 (Apr. 2012), pp. 4–16. DOI: 10.1016/j.jpowsour.2011.12.019.

LAKO & KOYAMA 2015

LAKO, P.; KOYAMA, M.: *Hydropower - Technology Brief*. IEA-ETSAP and IRENA, 2015. URL: [https://www.irena.org/-/media/Files/IRENA/Agency/Publication/2015/IRENA-ETSAP\\_Tech\\_Brief\\_E06\\_Hydropower.pdf](https://www.irena.org/-/media/Files/IRENA/Agency/Publication/2015/IRENA-ETSAP_Tech_Brief_E06_Hydropower.pdf).

LEE 2017

LEE, C.-G.: *Molten Carbonate Fuel Cells*. *Encyclopedia of Sustainability Science and Technology*. Springer New York, Oct. 2017, pp. 1–39. DOI: 10.1007/978-1-4939-2493-6\_141-3.

LEE ET AL. 2020

LEE, J. K.; LEE, C.; FAHY, K. F.; ZHAO, B.; LAMANNA, J. M.; BALTIC, E.; JACOBSON, D. L.; HUSSEY, D. S.; BAZYLAK, A.: *Critical Current Density as a Performance Indicator for Gas-Evolving Electrochemical Devices*. Cell Reports Physical Science 1.8 (Aug. 2020), p. 100147. DOI: 10.1016/j.xcrp.2020.100147.

LEMMON ET AL. 2018

LEMMON, E. W.; BELL, I.; HUBER, M. L.; MCLINDEN, M. O.: *NIST Standard Reference Database 23: Reference Fluid Thermodynamic and Transport Properties-REFPROP, Version 10.0*, National Institute of Standards and Technology. 2018. DOI: <https://doi.org/10.18434/T4/1502528>. URL: <https://www.nist.gov/srd/refprop>.

LETCHER 2017

LETCHER, T. M.: *Wind Energy Engineering: A Handbook for Onshore and Offshore Wind Turbines*. ACADEMIC PR INC, May 2017. 622 pp. ISBN: 0128094516. URL: [https://www.ebook.de/de/product/27799730/trevor\\_m\\_letcher\\_wind\\_energy\\_engineering\\_a\\_handbook\\_for\\_onshore\\_and\\_offshore\\_wind\\_turbines.html](https://www.ebook.de/de/product/27799730/trevor_m_letcher_wind_energy_engineering_a_handbook_for_onshore_and_offshore_wind_turbines.html).

LEVRON & SHMILOVITZ 2012

LEVRON, Y.; SHMILOVITZ, D.: *Power systems' optimal peak-shaving applying secondary storage*. Electric Power Systems Research 89 (Aug. 2012), pp. 80–84. DOI: 10.1016/j.epsr.2012.02.007.

LI ET AL. 2011

LI, X.; WALSH, F. C.; PLETCHER, D.: *Nickel based electrocatalysts for oxygen evolution in high current density, alkaline water electrolyzers*. Phys. Chem. Chem. Phys. 13 (3 2011), pp. 1162–1167. DOI: 10.1039/C0CP00993H.

LI ET AL. 2019

LI, Z.; ZHENG, Z.; XU, L.; LU, X.: *A review of the applications of fuel cells in microgrids: opportunities and challenges*. BMC Energy 1.1 (Oct. 2019). DOI: 10.1186/s42500-019-0008-3.

LIGEN ET AL. 2020

LIGEN, Y.; VRUBEL, H.; GIRAULT, H.: *Energy efficient hydrogen drying and purification for fuel cell vehicles*. International Journal of Hydrogen Energy 45.18 (Apr. 2020), pp. 10639–10647. DOI: 10.1016/j.ijhydene.2020.02.035.

LINDE GMBH 2019

LINDE GMBH: *Linde Hydrogen FuelTech - Tomorrow's fuel today*. Linde Engineering, 2019.

LINDEMANN 2007

LINDEMANN, U.: *Methodische Entwicklung technischer Produkte Methoden flexibel und situationsgerecht anwenden*. Berlin, Heidelberg: Springer Berlin Heidelberg, 2007. ISBN: 9783540374350.

LINSTROM 1997

LINSTROM, P.: *NIST Chemistry WebBook, NIST Standard Reference Database 69*. en. 1997. DOI: 10.18434/T4D303.

MARENBACH ET AL. 2020

MARENBACH, R.; JÄGER, J.; NELLES, D.: *Elektrische Energietechnik*. Springer Fachmedien Wiesbaden, 2020. DOI: 10.1007/978-3-658-29492-2.

MARTINSON ET AL. 2014

MARTINSON, C.; SCHOOR, G. VAN; UREN, K.; BESSARABOV, D.: *Characterisation of a PEM electrolyser using the current interrupt method*. International Journal of Hydrogen Energy 39.36 (Dec. 2014), pp. 20865–20878. DOI: 10.1016/j.ijhydene.2014.09.153.

MATTER 2018

MATTER, C. G.: *Membrane Filtration (Micro and Ultrafiltration) in Water Purification. Handbook of Water and Used Water Purification*. Springer International Publishing, 2018, pp. 1–17. DOI: 10.1007/978-3-319-66382-1\_3-2.

MCFADDEN & BASU 2016

MCFADDEN, S.; BASU, B.: *Wind turbine gearbox design with drivetrain dynamic analysis*. English. Offshore Wind Farms. United States: Elsevier Inc., Mar. 2016, pp. 137–158. ISBN: 9780081007792. DOI: 10.1016/B978-0-08-100779-2.00007-6.

MCPHAIL ET AL. 2011

MCPHAIL, S. J.; AARVA, A.; DEVIANTO, H.; BOVE, R.; MORENO, A.: *SOFC and MCFC: Commonalities and opportunities for integrated research*. International Journal of Hydrogen Energy 36.16 (Aug. 2011), pp. 10337–10345. DOI: 10.1016/j.ijhydene.2010.09.071.

MECHERIKUNNEL & RICHMOND 1980

MECHERIKUNNEL, A.; RICHMOND, J.: *Spectral distribution of solar radiation*. NASA Goddard Space Flight Center Greenbelt, MD, United States, 1980.

MEHRPOOYA 2014

MEHRPOOYA, P.: *Improvement of vertical-axis wind turbine performance via turbine coupling*. PhD thesis. July 2014. DOI: 10.13140/RG.2.2.13616.76808.

MERTENS 2015

MERTENS, K.: *Photovoltaik - Lehrbuch zu Grundlagen, Technologie und Praxis*. 3rd ed. Carl Hanser Verlag München, 2015. ISBN: 978-3-446-442.

MERWE ET AL. 2013

MERWE, J. VAN DER ; UREN, K. ; SCHOOR, G. VAN ; BESSARABOV, D.: *A study of the loss characteristics of a single cell PEM electrolyser for pure hydrogen production*. 2013 IEEE International Conference on Industrial Technology (ICIT). 2013, pp. 668–672. DOI: 10.1109/ICIT.2013.6505751.

MHI VESTAS OFFSHORE WIND 2018

MHI VESTAS OFFSHORE WIND: *MHI Vestas Launches the First 10 MW Wind Turbine in History*. Press Release (2018).

MILLER ET AL. 2020

MILLER, H. A. ; BOUZEK, K. ; HNAT, J. ; LOOS, S. ; BERNÄCKER, C. I. ; WEISSGÄRBER, T. ; RÖNTZSCH, L. ; MEIER-HAACK, J.: *Green hydrogen from anion exchange membrane water electrolysis: a review of recent developments in critical materials and operating conditions*. Sustainable Energy & Fuels 4.5 (2020), pp. 2114–2133. DOI: 10.1039/c9se01240k.

MOUGIN 2015

MOUGIN, J.: *Hydrogen production by high-temperature steam electrolysis. Compendium of Hydrogen Energy*. Elsevier, 2015, pp. 225–253. DOI: 10.1016/b978-1-78242-361-4.00008-x.

MÜLLER 2018a

MÜLLER, M.: *Stationary Lithium-Ion Battery Energy Storage Systems - A Multi-Purpose Technology*. PhD thesis. Technical University of Munich, 2018.

MÜLLER 2018b

MÜLLER, M.: *Entwicklung und Betrieb einer Anlage zur kontinuierlichen Hydrierung von flüssigen organischen Wasserstoffträgern im Technikumsmaßstab*. PhD thesis. Friedrich-Alexander-Universität, Erlangen-Nürnberg, 2018.

MUN ET AL. 2021

MUN, H. ; MOON, B. ; PARK, S. ; YOON, Y.: *A Study on the Economic Feasibility of Stand-Alone Microgrid for Carbon-Free Island in Korea*. Energies 14.7 (Mar. 2021), p. 1913. DOI: 10.3390/en14071913.

MUNOZ-HERNANDEZ ET AL. 2013

MUNOZ-HERNANDEZ, G. A. ; MANSOOR, S. P. ; JONES, D. I.: *Modelling and Controlling Hydropower Plants*. Springer London, 2013. DOI: 10.1007/978-1-4471-2291-3.

NAVARRO ET AL. 2015

NAVARRO, R. ; GUIL, R. ; FIERRO, J.: *Introduction to hydrogen production. Compendium of Hydrogen Energy*. Elsevier, 2015, pp. 21–61. DOI: 10.1016/b978-1-78242-361-4.00002-9.

NEILL & HASHEMI 2018

NEILL, S. P. ; HASHEMI, M. R.: *Introduction. Fundamentals of Ocean Renewable Energy*. Elsevier, 2018, pp. 1–30. DOI: 10.1016/b978-0-12-810448-4.00001-x.

NEL ASA 2019

NEL ASA: *M Series - Hydrogen Generation Systems*. (2019).

NELSON 2019a

NELSON, V.: *Innovative Wind Turbines*. CRC Press, Nov. 2019. DOI: 10.1201/9781003010883.

NELSON 2019b

NELSON, V.: *Wind energy : renewable energy and the environment*. Boca Raton, FL: CRC Press, 2019. ISBN: 9781138615342.

NIKOLAIDIS & POULLIKKAS 2017

NIKOLAIDIS, P. ; POULLIKKAS, A.: *A comparative overview of hydrogen production processes*. *Renewable and Sustainable Energy Reviews* 67 (Jan. 2017), pp. 597–611. DOI: 10.1016/j.rser.2016.09.044.

ONDA ET AL. 2002

ONDA, K. ; MURAKAMI, T. ; HIKOSAKA, T. ; KOBAYASHI, M. ; NOTU, R. ; ITO, K.: *Performance analysis of polymer-electrolyte water electrolysis cell at a small-unit test cell and performance prediction of large stacked cell*. English. *Journal of the Electrochemical Society* 149.8 (Aug. 2002). ISSN: 0013-4651. DOI: 10.1149/1.1492287.

PECENAK ET AL. 2020

PECENAK, Z. K. ; MATHIESEN, P. ; FAHY, K. ; CANNON, C. ; AYANDELE, E. ; KIRK, T. J. ; STADLER, M.: *The impact of project financing in optimizing microgrid design*. *Journal of Renewable and Sustainable Energy* 12.6 (Nov. 2020), p. 065301. DOI: 10.1063/5.0026187.

PESCHEL 2020

PESCHEL, A.: *Industrial Perspective on Hydrogen Purification, Compression, Storage, and Distribution*. *Fuel Cells* 20.4 (Aug. 2020), pp. 385–393. DOI: 10.1002/fuce.201900235.

PETROVIC 2020

PETROVIC, S.: *Introduction. Battery Technology Crash Course*. Springer International Publishing, Oct. 2020, pp. 1–20. DOI: 10.1007/978-3-030-57269-3\_1.



PFENNINGER & STAFFELL 2016

PFENNINGER, S. ; STAFFELL, I.: *Long-term patterns of European PV output using 30 years of validated hourly reanalysis and satellite data*. Energy 114 (Nov. 2016), pp. 1251–1265. DOI: 10.1016/j.energy.2016.08.060.

PHILLIPS & DUNNILL 2016

PHILLIPS, R. ; DUNNILL, C. W.: *Zero gap alkaline electrolysis cell design for renewable energy storage as hydrogen gas*. RSC Adv. 6 (102 2016), pp. 100643–100651. DOI: 10.1039/C6RA22242K.

PINGITORE ET AL. 2017

PINGITORE, A. T. ; MOLLEO, M. ; SCHMIDT, T. J. ; BENICEWICZ, B. C.: *Polybenzimidazole Fuel Cell Technology: Theory, Performance, and Applications*. Encyclopedia of Sustainability Science and Technology. Springer New York, Oct. 2017, pp. 1–38. DOI: 10.1007/978-1-4939-2493-6\_143-3.

PLETCHER & LI 2011

PLETCHER, D. ; LI, X.: *Prospects for alkaline zero gap water electrolyzers for hydrogen production*. International Journal of Hydrogen Energy 36.23 (2011), pp. 15089–15104. ISSN: 0360-3199. DOI: <https://doi.org/10.1016/j.ijhydene.2011.08.080>.

POWIDIAN 2019

POWIDIAN: *MobHyl Power M30*. 2019. URL: <http://powidian.com/wp-content/uploads/2018/06/fiche-tech.-MobHyl-Power-M30-RV-v2-US-merged.pdf>.

PREUSTER ET AL. 2017

PREUSTER, P. ; ALEKSEEV, A. ; WASSERSCHIED, P.: *Hydrogen Storage Technologies for Future Energy Systems*. Annual Review of Chemical and Biomolecular Engineering 8.1 (June 2017), pp. 445–471. DOI: 10.1146/annurev-chembioeng-060816-101334.

PROCESS INDUSTRY PRACTICES (PIP) 2013

PROCESS INDUSTRY PRACTICES (PIP): *PIP REEC001 - Compressor Selection Guidelines*. 2013.

QUASCHNING & MURIEL 2001

QUASCHNING, V. ; MURIEL, M.: *Solar Power – Photovoltaics or Solar Thermal Power Plants?*: VGB Congress Power Plants 2001. Deutsches Zentrum für Luft- und Raumfahrt e.V. (DLR). 2001. URL: <https://www.volker-quaschning.de/downloads/VGB2001.pdf>.

RITCHIE 2019

RITCHIE, H.: *Access to Energy*. Our World in Data (2019).

RUUD 2013

RUUD, C.: *Why not go green? : an analysis of the viability of solar PV mini-grids in Tanzania*. MA thesis. Norwegian University of Life Science, 2013.

SANKIR & SANKIR 2018

SANKIR, M. ; SANKIR, N. D., eds.: *Hydrogen Storage Technologies*. John Wiley & Sons, Inc., July 2018. DOI: 10.1002/9781119460572.

SANTOS ET AL. 2006

SANTOS, M. A. DOS ; ROSA, L. P. ; SIKAR, B. ; SIKAR, E. ; SANTOS, E. O. DOS: *Gross greenhouse gas fluxes from hydro-power reservoir compared to thermo-power plants*. Energy Policy 34.4 (Mar. 2006), pp. 481–488. DOI: 10.1016/j.enpol.2004.06.015.

SARBATLY 2020a

SARBATLY, R.: *Conventional Water Treatments. Membrane Technology for Water and Wastewater Treatment in Rural Regions*. IGI Global, 2020, pp. 138–165. DOI: 10.4018/978-1-7998-2645-3.ch006.

SARBATLY 2020b

SARBATLY, R.: *Fundamentals of Membranes and Membrane Processes. Membrane Technology for Water and Wastewater Treatment in Rural Regions*. IGI Global, 2020, pp. 1–24. DOI: 10.4018/978-1-7998-2645-3.ch001.

SCHMIDT ET AL. 2017

SCHMIDT, O. ; GAMBHIR, A. ; STAFFELL, I. ; HAWKES, A. ; NELSON, J. ; FEW, S.: *Future cost and performance of water electrolysis: An expert elicitation study*. International Journal of Hydrogen Energy 42.52 (Dec. 2017), pp. 30470–30492. DOI: 10.1016/j.ijhydene.2017.10.045.

SCHOLZ 2006

SCHOLZ, M.: *Water Softening*. Dec. 2006, pp. 135–139. ISBN: 9780444527349. DOI: 10.1016/B978-044452734-9/50023-2.

SCOTT 2020

SCOTT, K.: *Electrochemical methods for hydrogen production*. Cambridge, UK: Royal Society of Chemistry, 2020. ISBN: 9781788016049.

SDANGHI ET AL. 2019

SDANGHI, G. ; MARANZANA, G. ; CELZARD, A. ; FIERRO, V.: *Review of the current technologies and performances of hydrogen compression for stationary and automotive applications*. Renewable and Sustainable Energy Reviews 102 (Mar. 2019), pp. 150–170. DOI: 10.1016/j.rser.2018.11.028.

SELAMET ET AL. 2011

SELAMET, Ö. F.; BECERIKLI, F.; MAT, M. D.; KAPLAN, Y.: *Development and testing of a highly efficient proton exchange membrane (PEM) electrolyzer stack*. International Journal of Hydrogen Energy 36.17 (2011). International Conference on Hydrogen Production (ICH2P)-2010, pp. 11480–11487. ISSN: 0360-3199. DOI: <https://doi.org/10.1016/j.ijhydene.2011.01.129>.

SHARMA & ALI 2020

SHARMA, S. K.; ALI, K.: *Solar Cells*. Springer International Publishing, 2020. DOI: [10.1007/978-3-030-36354-3](https://doi.org/10.1007/978-3-030-36354-3).

SIMON-MARTIN ET AL. 2022

SIMON-MARTIN, M. DE; BRACCO, S.; PIAZZA, G.; PAGNINI, L. C.; GONZALEZ-MARTINEZ, A.; DELFINO, F.: *Levelized Cost of Energy in Sustainable Energy Communities*. Springer International Publishing, 2022. DOI: [10.1007/978-3-030-95932-6](https://doi.org/10.1007/978-3-030-95932-6).

SINGH 2015

SINGH, R.: *Chapter 1. Introduction to Membrane Technology*. Dec. 2015, pp. 1–80. ISBN: 9780444633620. DOI: [10.1016/B978-0-444-63362-0.00001-X](https://doi.org/10.1016/B978-0-444-63362-0.00001-X).

SLADE ET AL. 2018

SLADE, R. C. T.; KIZEWSKI, J. P.; POYNTON, S. D.; ZENG, R.; VARCOE, J. R.: *Alkaline Membrane Fuel Cells. Fuel Cells and Hydrogen Production*. Springer New York, Oct. 2018, pp. 439–453. DOI: [10.1007/978-1-4939-7789-5\\_154](https://doi.org/10.1007/978-1-4939-7789-5_154).

SONG ET AL. 2019

SONG, K.; LIU, L.; LI, F.; FENG, C.: *Degree of Hybridization Design for a Fuel Cell/Battery Hybrid Electric Vehicle Based on Multi-objective Particle Swarm Optimization*. 2019 3rd Conference on Vehicle Control and Intelligence (CVCI). IEEE, Sept. 2019. DOI: [10.1109/cvci47823.2019.8951610](https://doi.org/10.1109/cvci47823.2019.8951610).

STERNER & STADLER 2017

STERNER, M.; STADLER, I.: *Energiespeicher - Bedarf, Technologien, Integration*. Springer Berlin Heidelberg, 2017. DOI: [10.1007/978-3-662-48893-5](https://doi.org/10.1007/978-3-662-48893-5).

STOPLE 2011

STOPLE, R. A.: *Testing efficiency and characteristics of a Kaplan-type small turbine*. MA thesis. Norwegian University of Science and Technology, 2011. URL: [http://www.remotehydrolight.com/Testing\\_o\\_effeciency\\_kaplan.pdf](http://www.remotehydrolight.com/Testing_o_effeciency_kaplan.pdf).

SUN ET AL. 2017

SUN, Z.; LIN, B.; YAN, F.: *Anion-Exchange Membranes for Alkaline Fuel-Cell Applications: The Effects of Cations*. ChemSusChem 11.1 (Dec. 2017), pp. 58–70. DOI: 10.1002/cssc.201701600.

SUNDÉN 2019

SUNDÉN, B.: *Battery technologies. Hydrogen, Batteries and Fuel Cells*. Elsevier, 2019, pp. 57–79. DOI: 10.1016/b978-0-12-816950-6.00004-x.

SUNFIRE FUEL CELLS GMBH 2021

SUNFIRE FUEL CELLS GMBH: *Sunfire-Remote 900*. 2021.

TEICHMANN ET AL. 2012

TEICHMANN, D.; STARK, K.; MÜLLER, K.; ZÖTTL, G.; WASSERSCHIED, P.; ARLT, W.: *Energy storage in residential and commercial buildings via Liquid Organic Hydrogen Carriers (LOHC)*. Energy & Environmental Science 5.10 (2012), p. 9044. DOI: 10.1039/c2ee22070a.

THOMAS MELIN 2007

THOMAS MELIN, R. R.: *Membranverfahren*. Springer-Verlag GmbH, Mar. 2007. ISBN: 978-3-540-34327-1.

TIMMERBERG & KALTSCHMITT 2019

TIMMERBERG, S.; KALTSCHMITT, M.: *Hydrogen from renewables: Supply from North Africa to Central Europe as blend in existing pipelines – Potentials and costs*. Applied Energy 237 (Mar. 2019), pp. 795–809. DOI: 10.1016/j.apenergy.2019.01.030.

TONG ET AL. 2020

TONG, W.; FORSTER, M.; DIONIGI, F.; DRESP, S.; ERAMI, R. S.; STRASSER, P.; COWAN, A. J.; FARRÀS, P.: *Electrolysis of low-grade and saline surface water*. Nature Energy 5.5 (Feb. 2020), pp. 367–377. DOI: 10.1038/s41560-020-0550-8.

TOSHIBA ENERGY SYSTEMS & SOLUTIONS CORPORATION 2021

TOSHIBA ENERGY SYSTEMS & SOLUTIONS CORPORATION: *H2One - One container model*. 2021.

TRIANAPHYLLOU 2000

TRIANAPHYLLOU, E.: *Multi-criteria Decision Making Methods: A Comparative Study*. Springer US, 2000. DOI: 10.1007/978-1-4757-3157-6.

TRINKE ET AL. 2017

TRINKE, P.; BENSMANN, B.; HANKE-RAUSCHENBACH, R.: *Experimental evidence of increasing oxygen crossover with increasing current density during PEM water electrolysis*. *Electrochemistry Communications* 82 (2017), pp. 98–102. ISSN: 1388-2481. DOI: <https://doi.org/10.1016/j.elecom.2017.07.018>.

TSCHOPP ET AL. 2020

TSCHOPP, D.; TIAN, Z.; BERBERICH, M.; FAN, J.; PERERS, B.; FURBO, S.: *Large-scale solar thermal systems in leading countries: A review and comparative study of Denmark, China, Germany and Austria*. English. *Applied Energy* 270 (2020). ISSN: 0306-2619. DOI: 10.1016/j.apenergy.2020.114997.

ULLEBERG 1998

ULLEBERG, Ø.: *Stand-alone power systems for the future: Optimal design, operation and control of solar-hydrogen energy system*. PhD thesis. NTNU Trondheim, 1998.

UNIVERSITY OF WISCONSIN MADISON 1975

UNIVERSITY OF WISCONSIN MADISON: *TRNSYS, a Transient Simulation Program*. Solar Energy Laboratory, 1975.

URSUA ET AL. 2012

URSUA, A.; GANDIA, L. M.; SANCHIS, P.: *Hydrogen Production From Water Electrolysis: Current Status and Future Trends*. *Proceedings of the IEEE* 100.2 (Feb. 2012), pp. 410–426. DOI: 10.1109/jproc.2011.2156750.

VINCENT & BESSARABOV 2018

VINCENT, I.; BESSARABOV, D.: *Low cost hydrogen production by anion exchange membrane electrolysis: A review*. *Renewable and Sustainable Energy Reviews* 81 (2018), pp. 1690–1704. ISSN: 1364-0321. DOI: <https://doi.org/10.1016/j.rser.2017.05.258>.

VITO NV 2018

VITO NV: *Tiger Power with help of Vito/Energyville launches solar and hydrogen-driven alternative to diesel generators*. 2018. URL: <https://vito.be/en/news/tiger-power-help-vitoenergyville-launches-solar-and-hydrogen-driven-alternative-diesel>.

VOITH HYDRO HOLDING GMBH & Co.KG 2018

VOITH HYDRO HOLDING GMBH & Co.KG: *M-Line – Modular line for Small Hydro solutions at Voith*. 2018. URL: <https://voith.com/corp-en/hydropower-components/mini-hydro.html>.

WATTER 2015

WATTER, H.: *Regenerative Energiesysteme*. Springer Fachmedien Wiesbaden, 2015. DOI: 10.1007/978-3-658-09638-0.

WISER & BOLINGER 2019

WISER, R. H. ; BOLINGER, M.: *2018 Wind Technologies Market Report*. (Aug. 2019). DOI: 10.2172/1559241.

WISER ET AL. 2015

WISER, R. H. ; LANTZ, E. ; MAI, T. ; ZAYAS, J. ; DEMEO, E. A. ; EUGENI, E. ; LIN-POWERS, J. ; TUSING, R.: *Wind Vision: A New Era for Wind Power in the United States*. The Electricity Journal 28 (Nov. 2015). DOI: 10.1016/j.tej.2015.09.016.

YODWONG ET AL. 2020

YODWONG, B. ; GUILBERT, D. ; PHATTANASAK, M. ; KAEWMANEE, W. ; HINAJE, M. ; VITALE, G.: *Faraday's Efficiency Modeling of a Proton Exchange Membrane Electrolyzer Based on Experimental Data*. Energies 13.18 (2020). ISSN: 1996-1073. DOI: 10.3390/en13184792.

YUAN ET AL. 2020

YUAN, Z. ; WANG, W. ; WANG, H. ; YILDIZBASI, A.: *Developed Coyote Optimization Algorithm and its application to optimal parameters estimation of PEMFC model*. Energy Reports 6 (2020), pp. 1106–1117. ISSN: 2352-4847. DOI: <https://doi.org/10.1016/j.egyr.2020.04.032>.

ZAHORANSKY ET AL. 2010

ZAHORANSKY, R. ; ALLELEIN, H.-J. ; BOLLIN, E. ; OEHLER, H. ; SCHELLING, U.: *Wasserkraftwerke*. Energietechnik: Systeme zur Energieumwandlung. Kompaktwissen für Studium und Beruf. Ed. by R. ZAHORANSKY. Wiesbaden: Vieweg+Teubner, 2010, pp. 252–276. ISBN: 978-3-8348-9704-6. DOI: 10.1007/978-3-8348-9704-6\_11. URL: [https://doi.org/10.1007/978-3-8348-9704-6\\_11](https://doi.org/10.1007/978-3-8348-9704-6_11).

ZAKARIA ET AL. 2019

ZAKARIA, Z. ; MAT, Z. A. ; HASSAN, S. H. A. ; KAR, Y. B.: *A review of solid oxide fuel cell component fabrication methods toward lowering temperature*. International Journal of Energy Research 44.2 (Nov. 2019), pp. 594–611. DOI: 10.1002/er.4907.

ZALK & BEHRENS 2018

ZALK, J. VAN ; BEHRENS, P.: *The spatial extent of renewable and non-renewable power generation: A review and meta-analysis of power densities and their application in the U.S.* Energy Policy 123 (Dec. 2018), pp. 83–91. DOI: 10.1016/j.enpol.2018.08.023.

ZEBRA ET AL. 2021

ZEBRA, E. I. C.; WINDT, H. J. VAN DER; NHUMAI, G.; FAAIJ, A. P.: *A review of hybrid renewable energy systems in mini-grids for off-grid electrification in developing countries*. Renewable and Sustainable Energy Reviews 144 (July 2021), p. 111036. DOI: 10.1016/j.rser.2021.111036.

ZEISELMAIR 2010

ZEISELMAIR, A.: *Machbarkeitsstudie zur Errichtung einer Wasserkraftanlage zur elektrischen Versorgung des Dorfes Yuwienta im Regenwald Ecuadors*. MA thesis. Technische Universität München - Fachgebiet Hydromechanik, 2010.

ZHANG 2020

ZHANG, L.: *Electrochemical water electrolysis : fundamentals and technologies*. Boca Raton: CRC Press, Taylor & Francis Group, 2020. ISBN: 9780429447884.

ZÜTTEL 2004

ZÜTTEL, A.: *Hydrogen storage methods*. Naturwissenschaften 91.4 (Apr. 2004), pp. 157–172. DOI: 10.1007/s00114-004-0516-x.